Title
ANGULAR DISTRIBUTIONS OF TARGET FRAGMENTS FROM THE REACTIONS OF 292 MeV - 25.2 GeV 12C WITH 197au AND 238u

Author
Morita, Y.

Publication Date
1983-05-01

Lawrence Berkeley Laboratory
UNIVERSITY OF CALIFORNIA

ANGULAR DISTRIBUTIONS OF TARGET FRAGMENTS FROM THE REACTIONS OF 292 MeV - 25.2 GeV ^{12}C WITH ^{197}Au AND ^{238}U

Y. Morita
(Ph.D. Thesis)

May 1983

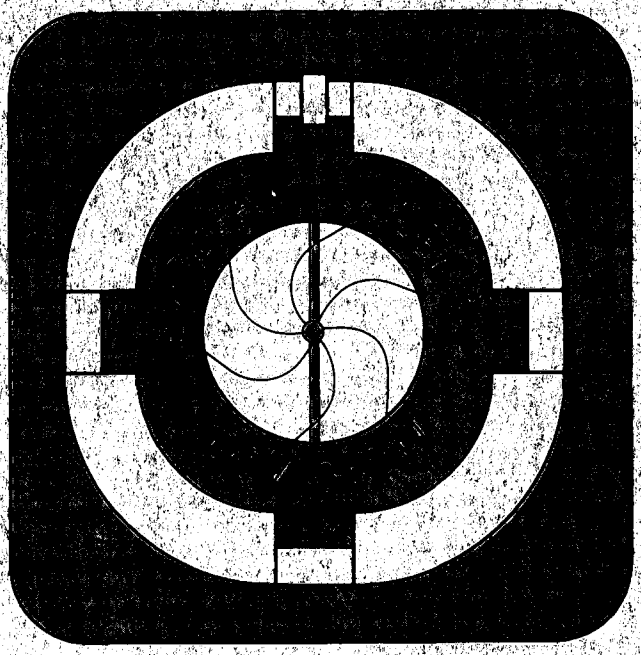

Prepared for the U.S. Department of Energy under Contract DE-AC03-76SF00098

DISCLAIMER

Angular Distributions of Target Fragments from the Reactions of 292 MeV - 25.2 GeV ^{12}C with ^{197}Au and ^{238}U

Yoshimitsu Morita

Ph.D. Thesis

Department of Nuclear Engineering

University of California at Berkeley

Nuclear Science Division

Lawrence Berkeley Laboratory

May 20, 1983

This work was supported by the Director, Office of Energy Research, Division of Nuclear Physics of the Office of High Energy and Nuclear Physics of the U.S. Department of Energy under Contract DE-AC03-76SF00098.

Abstract

Angular distributions of target fragments from the reactions of ^{12}C with ^{197}Au and ^{238}U were measured at projectile energies of 292 MeV, 1.0 GeV, 3.0 GeV, 12.0 GeV and 25.2 GeV.

The angular distributions of the ^{197}Au target fragments were all forwardly peaked. Extensively forward peaked angular distributions were observed at the non-relativistic projectile energies (292 MeV, 1.0 GeV). No obvious differences were observed in the angular distributions at the different relativistic projectile energies of 3.0 GeV, 12.0 GeV and 25.2 GeV. The characteristic angular distribution pattern from the relativistic projectile energy experiments was also observed in the non-relativistic energy experiments. Maximum degree of forward-peaking in the angular distributions at each projectile energy was observed at the product mass number (A) around 190 from the 292 MeV projectile energy, at A=180 from 1.0 GeV and at A= 175 from 3.0 GeV and 12.0 GeV.

In general, two different types of angular distributions were observed in the relativistic projectile energy experiments with the ^{238}U target. Isotropic angular distributions were observed for the fission product nuclides. The angular distributions of the fission products at the intermediate (292 MeV) energy showed slightly forward- peaked angular distributions. Because of the long projectile-target interaction time in the primary nuclear reaction, larger momentum was transferred from the projectile to the target nucleus. Steep forward-peaked angular distributions were also observed with the ^{238}U target. The reaction to produce the steep forward-peaked angular distributions with the ^{238}U target was the same as the one operating with the ^{197}Au target at the relativistic projectile energies. An interesting feature of the angular distribution was some favouring of sideward emission at the large angle for the light

products from the reaction of 25.2 GeV $^{12}C+^{238}U$ in comparison with the 12.0 GeV and 3.0 GeV projectile energy results.

Computations were attempted to estimate the basic properties of the target fragments for the reaction of the 3.0 GeV ^{12}C projectile with the ^{197}Au target using two different assumptions. In the first assumption, proton-proton elastic scattering experimental results were applied and the nucleons of the projectile and target nucleus were treated as completely free nucleons. The computation gave the side peaked angular distributions at all impact parameters. The other assumption was to treat the abraded volume of the target nucleus as a collective volume and to use the nuclear potential energy between the abraded volume and the residual target volume for computations of the recoil energies of the target fragments. The estimated recoil energies of the heavy products based on the second assumption had a trend consistent with the experimental data.

Acknowledgements

I would like to thank Professor Glenn T. Seaborg for having given me the opportunity to participate in the project at the Lawrence Berkeley Laboratory and for his guidance. I would like to thank also Professor Lawrence Ruby for supervising me at the Department of Nuclear Engineering. I am also grateful to Professor John O. Rasmussen for his advice on computations. I thank Professor Walter Loveland who gave me useful guidance on the experiments, Dr. K. Aleklett, Dr. T. Lund who helped me join the experiments at CERN and Mrs. Diana Lee who helped me for the data analysis. I am grateful to the people who helped me perform the experiments at the Bevalac and the 88-inch cyclotron and also grateful to my colleagues in Professor Seaborg's group who kept encouraging me. I thank Dr. Tek Lim and the people who gave me opportunities to use the research nuclear reactor at the Department of Nuclear Engineering.

I would like to thank Professor Thomas H. Pigford for his wise guidance during my entire period at Berkeley. I also thank Professors Donald Olander and Stanley Prussin for useful discussions.

Finally, I would like to thank my parents who gave me warm support from Japan.

I appreciate the support of the U.S. Department of Energy for the experiments.

Table of contents

I Introduction

The reaction between two heavy nuclei depends on the kinetic energy of the projectile nucleus in the center-of-mass system. At a kinetic energy below the Coulomb potential energy, the projectile nucleus does not approach the target close enough to make a compound nucleus. Instead, the interaction sometimes exchanges a few nucleons between the projectile and target nucleus at an energy slightly below the Coulomb energy. Also, photon exchange with no nucleon transfer excites the target nucleus and causes nuclear evaporation or even fission[1]. Sometimes, the projectile nucleus scatters the target nucleus without exciting it. A Coulomb interaction that results in no change of the nuclear energy level is characterized as elastic scattering.

At a kinetic energy of the projectile nucleus higher than the Coulomb potential barrier, the projectile nucleus can make a compound nucleus upon fusing with the target nucleus, or a deep inelastic reaction can occur transferring several nucleons between the target and projectile nucleus beside elastic scattering[2,3,4]. Also, after the primary reaction, the target nucleus may be excited and fission or evaporate some nucleons. However, the nucleons transferred from the projectile to the target nucleus do not have high enough kinetic energy to push out the colliding target nucleons breaking the binding with the rest of the target nucleus.

When the kinetic energy of a nucleon of the projectile nucleus is higher than the binding energy of a nucleon in the target nucleus, the nucleons transferred from the projectile nucleus to the target keep their original forward momentum by pushing out the colliding target nucleons. Thus, the reaction produces three parts. General descriptions of relativistic heavy ion nuclear reactions can be found in references 5 - 11. As is shown in Fig.1, because of the high

kinetic energy of the projectile nucleus, part of the projectile nucleus keeps moving forward leaving the reacting nucleons behind after the initial collision. The nucleons transferred from the projectile nucleus to the target carry a large momentum in the beam direction. Those nucleons knock off part of the target nucleus by imparting energy exceeding the binding energy of this part to the rest of the nucleus. Part A, in Fig.1, is the projectile nucleus residue. Part B is often called the participants. Part C is the target nucleus residue.

The projectile nucleus residue, part A, maintains its relativistic kinetic energy even after collision with the target nucleus[12]. Investigations on this aspect have been underway for several years at the Lawrence Berkeley Laboratory. The products from part B have been measured in various ways and many reaction mechanisms[13-19] have been proposed to describe the experimental results. However, the reaction mechanism is still obscure. The third part, C, is the target nucleus residue. The recoil kinetic energy of the target residue is small. At relativistic energy, the momentum transfer from the projectile is very small, because a compound nucleus is not formed. The target residues barely come out of the target material[20,21]. Part C has not been studied extensively, compared with the other two parts, even though it is equally important to understand this aspect of the relativistic nucleus reaction mechanism. This study was focused on the behavior of this target nucleus residue.

The angular distributions of the target fragments were measured in this work for the first time. To compare the results from those Bevalac experiments, the angular distributions were also measured from the reactions of non-relativistic energy projectiles. The experimental results showed the validity of the categorization of the three reaction parts, A, B and C. Even at the non-relativistic projectile energies, some of the characteristics of the angular distributions were observed similar to those observed from the results of the relativistic projectile

energy experiments. Measurements of the angular distributions of the target nucleus residues made possible the evaluation of the forward momentum transferred from the projectile nucleus corresponding to the different impact parameters for the primary reaction. This computational analysis tests the validity of the physical concept for relativistic nuclear reactions and may offer further insights into the reaction mechanism.

II Experimental

The angular distributions of the target residues were measured by catching the recoil fragments with catcher foils placed over the target. After the bombardment, the catcher foils were removed and divided into pieces corresponding to different axial angles from the beam direction, then mounted on a Ge(Li) detector to obtain the γ-ray spectra of the recoil nuclides caught on the catcher foils. From these γ-ray spectra, the decay curves were constructed to find the half-lives associated with the γ-ray peaks. By counting the standard source with the same detector, each peak position of the spectra was calibrated to give the γ-ray energy. The energy and half-life gave the information necessary to identify the nuclides[22,23]. The radioactivity at the end of the bombardment was computed with the help of the data from the decay curve for each nuclide. The relative activities on the different angular catcher foils were calculated for each nuclide. These relative yields were divided by the solid angles subtended by the angular catcher foils relative to the target to give the differential cross sections.

In order to understand heavy ion nuclear reaction mechanisms, it is desirable to employ a heavy element as target . Depleted uranium and gold were chosen for the target material. Uranium is a heavy element and has a large reaction cross section and fissions into a variety of products, which may not clearly show the character of the primary reaction. On the other hand, gold is interesting to compare with uranium, since gold is much less fissionable and also a heavy element. Carbon was chosen as the projectile. Although carbon is not a very heavy element, in this recoil experiment, high beam intensity is required. The Bevalac produces a relatively high intensity carbon beam.

The projectile energies used for the angular distribution measurements are 2.1 GeV/n, 1.0 GeV/n and 250 MeV/n from the Bevalac at the Lawrence Berkeley Laboratory, 86 MeV/n from the SC synchrocyclotron at CERN in Switzerland and and 24.5 MeV/n from the 88-inch cyclotron at the Lawrence Berkeley Laboratory.

II-A Bevalac Experiments

The target assemby utilized for the Bevalac experiments is shown in Fig.2. $^{238}UF_4$ and ^{197}Au were evaporated on a 2 mil thick aluminum foil and a 5 mil thick mylar foil, respectively. The target backing material should be as light as possible, so that the radioactivities of the recoils produced from the backing material do not disturb the measurement of the target recoils. UF_4 and Au were evaporated to produce ~1mg/cm^2 thickness deposits with a 5/8 inch diameter which is comparable to the size of the Bevalac beam . The thickness of the Au evaporation target was determined by the activation analysis method using the TRIGA-MARK-III reactor at the Department of Nuclear Engineering of the University of California, Berkeley. The catcher foil was made of a cone shaped 2 mil thick mylar and placed over the evaporated target material. Although the mylar catcher foils were directly exposed to the beam during the bombardment, the components of mylar ($C_{10}H_8O_4$) will not produce any heavier nuclides than themselves at relativistic projectile energies[24,25]. These catcher foils caught the target nucleus residues recoiling from the evaporated target as a result of the reaction with the carbon projectile. Since the recoils should reach the catcher foil without major attenuation, the whole assembly was put in a vacuum chamber and evacuated to ~2×10^{-2} Torr. Also, the target should be thin to reduce scattering and absorption of the fragments. However, a thin target does not produce a sufficient amount of recoil nuclides for measurement. The energy degradation of the carbon projectile in the Al and mylar backing was estimated[26,27] to be much less than 3 MeV even for the 100 MeV/n ^{12}C beam which is the highest energy available in reference 27. This is negligible in comparison to the initial energy. Taking advantage of the large energy of the relativistic energy projectile, the multi-target system was employed to overcome

the insufficient beam intensity. Seventeen target-catcher foil components were built into each assembly. Although the size of the target evaporation was relatively large, it was almost uniformly exposed to the beam, because of the difficulty to focus the beam pulses at the Bevalac. The total beam fluences were 10^{14} over the time period of ~27 hours for the 250 MeV/n beam, 10^{13} over 11.5 hours for the 1.0 GeV/n and 10^{12} over 10 hours for the 2.1 GeV/n beams. After the bombardment, the catcher foils were removed and divided into 4 concentric pieces whose angular ranges were 0°–30°, 30°–50°,50°–70° and 70°–90° from the center of the target in the beam direction. The catcher foils which had the same angular range from each of seventeen target assemblies were counted together by using a Ge(Li) detector to increase the intensity of the radioactivity. The levels of radioactivities of the target fragments caught on the catcher foils were assessed through the usual analysis of the γ -ray spectra. After identifying the product nuclides, the radioactivity level, A_0, of each nuclide at the end of the bombardment was computed to give the relative yields at the different recoil angles. The differential cross section, $d\sigma/d\Omega(\vartheta)$, was obtained by dividing the relative activities by the "catching probabilities" of the different angular catcher foils subtending from the target. A schematic diagram is given in Fig.3, showing the analysis employed to compute the catching probabilties for the different angular catcher foils in this experiment. The target was assumed to be uniformly exposed to the beam. Also, the atoms recoiling out of the target material were assumed to reach the catcher foil and were all stopped. According to the Northcliffe and Schilling table[26], the heaviest element (^{181}Re) identified here, which is also estimated to have the lowest recoil energy[28] (~10 MeV), has a recoil range of 0.6 mg/cm^2 in air. Comparing this value with the air density in the target chamber, 2×10^{-5} mg/cm^3, we can see the attenuation of the recoil atoms in the vacuum chamber is negligible (

distance between the target and catcher foil is 2 cm). The thickness of the mylar catcher foil, 7.3 mg/cm^2, is large enough to stop the lightest nuclide identified here, which has a large kinetic energy, ~50 MeV[28]. The recoil range of such a nuclide in mylar is estimated to be ~1.5 mg/cm^2, using the recoil energy estimates reported by Loveland *et al* [28].

A description of the analysis used for the determination of the differential cross section is as follows:

On the basis of Fig.3, we can see that all the recoils caught by the cone part, a_c, must pass through the circle plane, a_p. The probability for the particles to be caught by a_c , after isotropic emission from the target, is thus the same as the probability for the particles to pass through the plane, a_p. (a_p=a_c). On the basis of the same argument, the recoils to reach the cone part, a_c+b_c, must pass through the plane, b_p (b_p=a_c+b_c). Rewriting this equation, we obtain b_c=b_p−a_p. Now, we have the probabilities for, a_c and b_c. For the third part of the angular catcher foil, the same analysis gives the relation, c_c=c_p−b_p. The fourth part was assumed to have d_c=0.5−c_p, since half of the particles will be recoiled onto the catcher foil. Finally, the whole problem is now to find the "catching probabilities" for the isotropically emitted recoils caught by such catcher foil discs coaxially placed parallel to the target plane. The details of the computation are described in Appendix A.

Still, the actual experimental assembly might seriously differ from this idealized situation so as to cause serious errors in the final results, due to the geometric distortion of the cone shaped catcher foil and the thickness of the evaporated target. These effects were measured in a calibration experiment. For this purpose, we measured the angular distribution of fission products from the 43 MeV ^{4}He+^{238}U reactions, using a target-catcher foil assembly identical to those used in the Bevalac experiments. The 44.3 MeV α-particle beam from the 88-inch

cyclotron at the Lawrence Berkeley Laboratory was utilized, taking into account the beam energy degradation by the Al target backing foil and the UF_4 material itself. The beam was collimated by use of the 5/8 inch diameter carbon block to expose the evaporated target uniformly as it was in the Bevalac experiments. After irradiation with the total fluence of $\sim 10^{14}$ ions of ^{12}C over the time period ~4 hours, the single catcher foil was removed and divided into four pieces, as it was in the Bevalac experiments. The relative activities of the fission nuclides, ^{99}Mo and ^{112}Pd, for the four foils, were compared with the angular distribution function, $W(\vartheta)=1+ \alpha_2 P_2+\alpha_4 P_4$, reported by Vandenbosch *et al* [29]. thus giving the calibration factors for the angular catcher foils. The correction factors (A) obtained for the 30°, 50°, 70° and 90° catcher foils are 1.00, 1.03, 1.04 and 1.44, respectively. The computational detail for the calibration factors is described in Appendix A.

Another set of calibration factors was necessary in order to account for the counting geometry errors. The mounted counting sample for the widest angular catcher foil has a large area compared with the smallest angular one. Since the measurement was done by use of a Ge(Li) detector, the geometrical angle between the Ge(Li) crystal and the mounted samples affects the counting efficiency. The correction factor for each angle was obtained by measuring the γ-ray yield of ^{137}Cs spread over the same area of the catcher foils. Since the multiple target system was used for the Bevalac experiments, angular catcher foils of the same angle were counted together as one sample at the Ge(Li) detector. The thicknesses of the samples mounted for counting at the Ge(Li) detector also affected the counting efficiency. This correction was also considered in the similar way to that described above. The final geometric correction factors (B) are 1.00, 1.00, 1.13 and 1.27 for the 30°, 50°, 70° and 90° catcher foils, respectively. The final values of the differential cross sections,

$d\sigma/d\Omega$, were calculated by use of the following formula, using the activity, A_0, for each angular catcher foil and the correction factors, A and B,

$$d\sigma/d\Omega(\vartheta) = \frac{A_0}{P} x A x B$$

and where P is the "catching probability" given in Appendix A.

II-B SC synchrocyclotron experiment at CERN

The SC synchrocyclotron at CERN produces 86 MeV/n carbon beam with an intensity more than 10^3 times of the higher energy beams from the Bevalac. Also, the beam was well focused to $\leq$ 3 mm diameter without a collimator. The total beam fluence was $\sim 10^{16}$ ions over the time period of 15 hours for both Au and U target experiments.

The experiments were performed through the joint work between the people involved in the CERN projects and those in the LBL.

For the experiment with the Au target, the experimental set up was owing to the efforts of the people in Europe (Aleklett, Hagebo, Haldorsen, Lund and Molzahn) and my colleagues involved in the LBL projects (McGaughey and Loveland).

For the experiment with the U target, the experimental set up was owing to the effort of the people in Europe (Aleklett and Lund) and my colleagues (McGaughey and Loveland).

The high intensity of the beam made the experiment easier than the Bevalac experiments. The target assembly consisted of a single evaporated target and catcher foil, forward and backward, as shown in Fig.4. The ^{197}Au and $^{238}UF_4$ were evaporated on the Al foil of thickness 13 mg/cm^2 with thickness of 0.3 mg/cm^2 and 0.8 mg/ cm^2, respectively. The beam energy was degraded by this backing foil by less than 3 MeV[27]. The whole target assembly was evacuated in the beam line to $\leq 10^{-6}$ Torr. The experimental procedure was similar to that used in the Bevalac experiments. After the bombardment, the catcher foil was removed and divided into different angular pieces. The divided pieces were mounted at a Ge(Li) detector and the γ-ray spectra were obtained to construct the decay curve in order to identify the products. After the measurements done by Kraus and Loveland at the Oregon State University for the samples

from the experiment with the Au target, analyses were done at the Oregon State University and at LBL. For the experiment with the U target, during the first eighteen days after the end of bombardment, the measurement was performed at CERN for the short half- lived nuclides. The measurement for the long half-lived nuclides was done by Aleklett at Studsvik, Sweden. The data obtained from the first counting were partly analyzed with GAMANAL[30] by Lund and partly with SAMPO[22] at LBL. Those from the second part of the measurement was analyzed with SAMPO at LBL. The catching probability and the mean angles, $\langle\vartheta\rangle$, for each angular catcher foil, subtended from the small diameter beam spot, were computed using the equations given in Appendix A just as they were in the analysis of the Bevalac experiments. The small size of the beam spot eliminated the need for most of the corrections which were necessary for the Bevalac experiments. Corrections were made only for the relative thickness of the backward and forward target thicknesses. The relative activities on the catcher foils were divided by the solid angles to obtain the differential cross sections.

II-C 88-inch cyclotron experiment

A 292 MeV ^{12}C beam was obtained with barely enough intensity to carry out this recoil experiment with the 88-inch cyclotron at the Lawrence Berkeley Laboratory. The ^{197}Au and $^{238}UF_4$ evaporated targets of ~1mg/cm^2 thickness were prepared as they were in the previous studies. 10^{14} particles were delivered over the time period of 10 hours. The catcher foil was made of 13 mg/cm^2 mylar foil. A schematic diagram is given in Fig.4. Because of the significant beam energy attenuation, unlike the Bevalac experiment, a single target-catcher foil assembly was used. With the 13 mg/ cm^2 thick Al backing, the 292 MeV C beam energy was degraded by 8 MeV, as determined by use of the stopping power table[27]. The assembly shown in Fig.4 was set in the chamber and evacuated to 10^{-4} Torr. An advantage of this experiment was that the beam was better focused. Also, a carbon collimator could be used to obtain a small 1/4 inch diameter beam spot on the target.

After the bombardment, the same experimental procedure was used as before. The mathematical treatment used for this analysis was much easier than in the Bevalac experiments because of the relatively small beam spot size. The catcher foil was divided into five and four different angles for the Au and U target, respectively. The catching probability for each angular catcher foil was computed, again using the equations in Appendix A.

III Experimental Results

The angular distributions were measured with five different projectile energies involving three different types of accelerators. As described above we employed different target-catcher foil assemblies to correspond to the different beam parameters characteristic of the different machines. The numbers of identified nuclides ranged from only three nuclides from the 25.2 GeV ^{12}C + ^{238}U reaction to forty five from the 1.0 GeV ^{12}C+^{238}U reaction. The number of angular data points also ranged from four points for the Bevalac experiments to nine for those at the SC synchrocyclotron at CERN with the Au target. In order to extract physically meaningful results for use in comparison among these different experiments, a function to fit the experimental results was sought. The mathematical process was difficult and only a moderately good fit was accomplished. However, the obtained function enabled us to examine the five different types of results in a comparative manner.

III-A-1 Results from the 25 GeV, 12 GeV and 3 GeV $^{12}C+^{197}Au$ reactions

The experimental results are shown in Fig.5 , 6 and 7 and tabulated in Table I , III and V for the reactions of 25.2 GeV, 12.0 GeV and 3.0 GeV $^{12}C+^{197}Au$, respectively. The results of the angular distributions were normalized at the widest average angle, 73.8°. As was mentioned above, the total beam fluence for the 25 GeV ^{12}C ions was small and that for the 3 GeV ^{12}C ions was relatively large, which resulted in the identification of five nuclides from the 25 GeV energy experiment, nine from the 12 GeV experiment and twelve from the 3.0 GeV experiment. A more complete tabulation of the products from these nuclear reactions can be found in the work by Kaufman *et al* [25]. All the nuclides show forward peaked angular distributions. The relatively light products, ^{44m}Sc,^{97}Ru from the 25 GeV experiment, ^{89}Zr, ^{90}Nb and ^{97}Ru from the 12 GeV experiment and ^{89}Zr,^{90}Nb,^{97}Ru and ^{123}I from the 3 GeV reaction have mildly forward peaked distributions. The relatively heavy products, which are the rest of the products, are much more forward peaked. Fig.8 shows that the angular distribution become steeper with increase of the product mass number until the mass number reaches 167 in the 3 GeV ^{12}C experiment. Among the products heavier than ^{167}Tm, the forward peaking of angular distributions becomes milder with increase of mass number. The angular distributions from the 12 GeV ^{12}C experiments show a similar trend. The steepest forward distribution is observed at mass numbers between 149 and 155. These characteristics of the forward peaked angular distributions, observed in the 3 GeV and 12 GeV energy experiments, are in good agreement with the results for F/B (forward/backward) ratios measured by Kaufman *et al* [25]. The products which give steep forward distributions have large values of F/B ratios. The relation between these trends

and the impact parameters of the primary reaction will be of interest in order to understand high energy heavy ion nuclear reactions[31,32]. The error bars reflect only statistical errors. Since the effect of the evaporated target thickness was corrected for by use of the measured angular distributions of fission products from the 43 MeV ^{4}He +^{238}U reaction, the relatively light products, with estimated recoil energies which are almost the same as those of the ^{4}He induced fission products, do not have large errors as indicated by the results obtained here. However, the error caused by the target thickness is significant for the heavy products. The heavy products are estimated to have small recoil energies and the stopping power is large[28]. The correction factors were estimated by use of the equations given in Appendix A using an estimated 10 MeV for the recoil energy for the heavy products, together with the use of of the recoil range table[26]. The estimated error is significant at the largest angle. Since the angular distribution was normalized to this largest angle, we cannot simply compare the values at the small angles with those for the heavy products. A function to fit the angular distributions was sought in order to make comparison possible among the different products, ranging from the light ^{44m}Sc to the heavy ^{181}Re. Since we had only four data points in the distribution, the task was difficult. The function, $y=\frac{b}{\sin^{c}(a\vartheta)}$, was used to fit all the angular distributions from the Au target at all five different energy experiments. The mathematics involved to accomplish this purpose are shown in Appendix B. The derivatives of the angular distribution functions were computed at the angle, 26°. These derivative values are specially useful to find physical meaning for the angular distributions in comparison among different product mass numbers, since the small angle points (22.7°, 33.1°) do not have the significant errors caused by the target thickness. The function gives acceptable fit at the

small angles, independent of the errors at the largest angle, as seen in Fig. 5 -7. The derivative values are given in Fig.8 with respect to the product mass number. Table II, IV and VI tabulate these values with the parameters to give the best fit of the function by use of the least squares method.

III-A-2 Results from the 1 GeV $^{12}C+^{197}Au$ reaction

Because of the high intensity of the ^{12}C beam from the SC synchrocyclotron at CERN, we obtained much more precise results than those obtained from the Bevalac. Through our analysis, twenty eight nuclides were identified, giving nine angular points, five for the forward angles and four for the backward. Identification of more products is found in reference 33. The results are shown in Fig.9 and tabulated in Table VII. The differential cross sections were normalized to the largest forward angle, 71°. The general trend is similar to the Bevalac results. The relatively light products ($\leq^{121}Te$) show the mild forward peaks and the heavy products ($\geq^{145}Eu$) show steep forward peaks in the angular distributions. The steepest forward-peaked distribution was found around the mass number 167. Interesting isotopic effects in the angular distributions were observed for Rb, Y, Zr, Eu, Gd and Pt. The functional fit was good for the light products. Because of the steep forward distribution with the long tail, the fit was not good for the heavy products. In these cases, the function fit was attempted only for the forward angles.

The derivative values at 26° are given in Fig.10 and tabulated in Table VIII. The isotopes which have smaller mass numbers than those of the largest derivative value (shown in Fig.10) show an increase in the degree of forward peaking of angular distributions with increase of the mass number, but the isotopes of Pt show the opposite trend. This fact implies that Pt was produced by a different reaction process. In the reaction producing Pt isotopes, the momentum transfer from the projectile was small because of the large impact parameter. The reaction at smaller impact parameter is expected to produce smaller mass number products. This general character is very similar to the trend of the

Bevalac experiments, which shows an effective role of the impact parameter in relation to the forward momentum transfer. The small surface mass density will make the same reaction possible as that at the higher projectile energy. Fission products which are usually observed from ^{238}U fission were observed among the relatively light products ($\leq^{121}Te$). The reaction with relatively small impact parameters leaves the target nucleus in the highly excited energy level and leads to fission. The deexcitation of the fission products will evaporate nucleons. The evaporation and fission itself will smear out the forward momentum initially transferred from the projectile. In Fig.10, the derivative values are observed approximately similar among the relatively light products. However, the results described in this work show the angular distributions which do not include the angular points in the beam direction. The radioactive background produced by the reaction with the catcher foil material made it difficult for us to identify the products from the reaction with the target material.

A new analysis which is under progress will show that the data points of the angular distributions at ~0° are considerably different among those of the relatively light products. The results will be reported in the near future.

III-A-3 Results from the 292 MeV ^{12}C+ ^{197}Au Reaction

Eight nuclides were identified from the 292 MeV ^{12}C + ^{197}Au reaction and their angular distributions were obtained with five forward angular points. The angular distributions are shown in Fig.11 and tabulated in Table IX. The results were normalized to the largest angle. The relatively heavy products give steep forward peaked angular distributions. The derivative values at 26° were also obtained and shown in Fig.8 and tabulated in Table X. Isotopic effects were observed for the Au products. The derivative of ^{194}Au is much larger than that of ^{196}Au. The derivative of the ^{196}Au angular distribution is extremely small. The approximately isotropic angular distribution of ^{196}Au is due to the recoil by one neutron evaporation, after excitation by the primary reaction. Also, the momentum transfer from the primary reaction seems to be very small.

III-B-1 Results from the 25.2 GeV, 12.0 GeV and 3.0 GeV $^{12}C+^{238}U$ reaction

Only three nuclides were identified from the 25.2 GeV $^{12}C+^{238}U$ reaction, because of the low total beam fluence of the highest energy projectile from the Bevalac. Data for these are shown in Fig.12 and tabulated in Table XI. Six nuclides and seven nuclides were identified from the 12.0 GeV and 3.0 GeV $^{12}C+^{238}U$ reactions, respectively. The results are shown in Fig.13 and Fig.14 and tabulated in Table XII and Table XIII for the 12.0 GeV and 3.0 GeV projectile energy, respectively.

In Fig.13 and Fig.14, we can observe two different types of angular distributions. One is an almost flat distribution and the other is a forward peaked distribution similar to those observed with the Au target. The flat distributions are observed in the measurements for the nuclides, ^{72}As, ^{89}Zr,^{97}Zr,^{99}Mo and ^{133}I, which are typical fission products from ^{238}U. The peripheral collision kicks out several nucleons from the target nucleus, leaving it in excited states which are high enough to cause fission. The almost completely flat distributions, like those of ^{99}Mo, imply that the initial momentum given by the primary reaction is very small in comparison with the random recoil momentum arising from the fission process. The fission process has a significant role in the production of ^{99}Mo. On the other hand, the non-fission light product, ^{43}K, gives a slightly forward peaked angular distribution. The non-fission heavy product, ^{149}Gd, gives a steep forward peaked angular distribution. This trend is similar to the results obtained for the angular distributions from the Au target. The same type of reaction actually takes place for both reactions with ^{197}Au and ^{238}U targets, although the fission is dominant in the reaction with the U target, especially in the production of the typical fission nuclides. The angular distributions of the

products identified in this work are in good agreement with the measurements of F/B values[28,34]. Also, it is interesting to compare our results with those from 0.8 - 400 GeV proton bombardments[35-39].

From the results obtained with the 25.2 GeV projectile energy, we can see interesting features. The nuclides identified at this projectile energy are typical fission products. The distributions are almost flat like the fission nuclides obtained with the 3.0 GeV and 12.0 GeV projectile energies. However, we may observe a relative increase of the differential cross section at 73.8° for ^{89}Zr and ^{97}Zr angular distributions. As mentioned before, the experimental assembly and the analysis were exactly the same for the three different Bevalac experiments. With use of the same mathematical method as applied to the analyses of the other experiments, an attempt was made to find the best fit functions. But, even the best fit was not good enough to be meaningful for the 25.2 GeV projectile energy experiments. Therefore, the slopes for the differential cross sections at 44.3° and 73.8° were calculated .

The slopes calculated for the light products of the three Bevalac energy experiments are given in Fig. 15. Fig.15 shows that the slope values are large for the light products from the 25.2 GeV projectile energy reaction in comparison with the results from the 3.0 GeV and 12.0 GeV energy experiments. This observation may not contradict the fact that the observation of sideward peaked angular distributions of light products from the 400 GeV p + Heavy Elements reaction done by Stewart and Porile *et al* [36,37] is more obvious than the observation from the 3 GeV and 11.5 GeV p+U reaction[35]. A disagreement, however , is that the mild forward peak of the angular distribution was also observed in our studies. The observation of approximately equivalent forward and backward production cross sections by Loveland *et al* [34] also presents a question about our results of the forward peak of the angular distributions for the light products at this

projectile energy. The discrepancy between the two results may be understood, if we observe the increase of the angular distributions around 90° by performing the experiment for the backward angular distributions. The possible observation of the hump at the sideward angle is difficult to understand by use of the usual concepts developed for the relativistic heavy ion nuclear reaction. At the projectile energy of 2.1 GeV/n, π-meson production must be significant. However, the major fraction of pions does not recoil sidewards and therefore they cannot give such a sideward recoil momentum to the target residue.

III-B-2 Results from the 1.0 GeV $^{12}C+^{238}U$ Reaction

After the bombardment, nuclides of short half-lives were measured at CERN. The nuclides of relatively long half-lives were measured at LBL and at two other places in Europe. Forty five nuclides were identified alltogether from this experiment. Eight angular points were obtained and the angular distributions are shown in Fig.16 and tabulated in Table XIV. All the angular distributions are forward peaked in this reaction of 1.0 GeV ^{12}C + ^{238}U, but much less forward peaked than the distributions of the products from the Au target experiments of the same projectile energy. The distributions of the products, ^{169}Yb,^{153}Gd and ^{146}Gd have steep forward peaks. The functions were found to fit the experimental results with good agreement. The derivative at the angle, 26°, was calculated from the functions and is shown in Fig.17 and tabulated in Table XV. The isotopic effects for the angular distributions were observed among the relatively light nuclides as can be seen in Fig.17. The derivatives at 26° of the isotopes of Sc, Y, Zr, Ru, Rh, Ag, In, Sb, I, Te and Ba decrease with increase of mass number. This trend is opposite to those of the fission products from the Au experiments of the same projectile energy, but the same as the trend for the angular distributions of the Pt isotopes.

III-B-3 Results from the 292 MeV $^{12}C+^{238}U$ Reaction

Seven nuclides were observed in the 292 MeV ^{12}C + ^{238}U reaction. The angular distribuitons are shown in Fig.18 and tabulated in Table XVI. Although all the identified nuclides are typical fission products except ^{48}Sc, the angular distributions of all the nuclides are forward peaked. The kinetic energy of the projectile in this experiment is low and the primary reaction is a relatively slow process, such as an incomplete fusion reaction or a compound nucleus production[40]. The interaction in a relatively long time period allows the large forward momentum transfer to the target nucleus from the projectile.

III-C Summary of Results

The relations among the results of angular distribution measurements with five different ^{12}C projectile energies and ^{238}U and ^{197}Au targets were investigated with help of derivative values from least squares fit functions.

The derivative values of angular distributions from five different projectile enegies with a Au target are shown in Fig.8 and Fig.10. We observe large derivatives of the angular distributions around the product mass number of 160 for 3 GeV and 12 GeV $^{12}C+^{197}Au$ reactions. The largest derivative value from the 1 GeV projectile energy experiment is observed at a slightly larger product mass number than for the 3 GeV and 12 GeV projectile energy experiments. The 1 GeV projectile can produce the same reaction effects as those for the 3 GeV and 12 GeV energy projectiles only at larger impact parameters. The reaction must abrade more nucleons at the smaller impact parameters. (Assuming abrasion between the projectile and the target nucleus during the primary reaction, geometric characteristics between the two spherical nuclei were computed. Fig.19 shows the relation between the residual masses of the target nucleus and the impact parameters.) The abrasion model is again useful for interpreting the derivatives for the Pt and Au isotopes produced from the 1 GeV and 292 MeV C + Au experiments, as shown in Fig.8 and Fig.10. At the 292 MeV projectile energy, the observation of the large derivative values for ^{123}I, ^{181}Re and ^{194}Au (Fig.11) may imply that the reaction such as abrasion as observed for the relativistic energies took place between the nuclear surfaces of target and projectile. Since the mass density is small on the nuclear surface, the 292 MeV projectile can abrade the nucleons at the surface. The products of relatively small mass numbers ($\leq^{121}Te$) have similar values of derivatives of the angular

distributions in the range between 1 and 7 for all the five different projectile energies as we can observe in Fig.8 and Fig.10. The reaction to produce these products is different from the reaction to produce heavy products. The relatively light products are produced from the reactions with small impact parameters, which do not clearly show the effects of the primary reaction such as abrasion reaction. However, the angular distributions of the heavy products ($\geq^{145}$Eu) are useful to understand the relativistic heavy ion nuclear reaction mechanism; the information from peripheral interactions is particularly instructive.

The derivative values of angular distributions with the ^{238}U target are shown in Fig.17 only for the 1 GeV experiment. ^{238}U is much more fissionable than ^{197}Au and we therefore observe particular effects which we do not observe from the Au target experiments. The typical fission products give flat angular distributions from the reactions with relativistic projectile energies. The reactions with lower projectile energies show the forward peaked angular distributions even for these typical fission products. Since the non-relativistic energy projectile takes a longer time in the reaction with the target nucleus in comparison with the relativistic energies, it transfers more primary forward momentum. Comparing Fig.10 and Fig.17, the angular distributions from the Au target are steeper than those from the ^{238}U target by a factor of 10 . However, we must be careful to consider the following points. The largest nuclide observed from the U target has the mass number 169, formed by the loss of 69 nucleons from the original U mass number of 238. The product mass number from the Au target equivalent (by ratio) to this product mass number is 139. An interpolation in Fig.10 gives a value for the derivative of around 20, which is approximately equivalent to the derivative of the ^{169}Yb angular distribution as shown in Fig.17.

This fact implies that the same type of reaction produced the heavy products for both the Au and U targets. This reaction is heavily dependent on the impact parameter. We could not identify the heavy elements from the U target experiments corresponding to those observed from the Au target. Although the peripheral abrasion reaction actually occurs also for the U target, the heavy products do not survive fission. The increase of the angular distributions of the light products at the wide angle from the U target are observed at the 25.2 GeV projectile energy relatively to the 3.0 GeV and 12.0 GeV energy. The light product (^{44m}Sc) from the Au target produced with the 25.2 GeV energy projectile shows the similar increase in the angular distribution but not any heavier products, although the angular distribution of products heavier than ^{44m}Sc from the 400 GeV p + Heavy Elements reactions show obvious sideward peaks[37]. A target as heavy as ^{238}U or the lightest product from ^{197}Au and a projectile energy as high as 25.2 GeV/n seem necessary to produce this particular feature of the angular distribution. The isotopic effects for the angular distributions of the light products from the 1 GeV C + Au reaction are opposite to those from the 1 GeV C + U reaction. The isotopic effect for the Au angular distributions from the 292 MeV C + Au reaction is the same as that for the 1 GeV C + U reaction. These light products are fission products from ^{238}U and ^{197}Au. ^{197}Au must be excited to a higher level than ^{238}U to produce fission products. The smaller impact parameter giving the higher excitation would also transfer more forward momentum to the target nucleus. On the other hand, ^{238}U would fission even at the large impact parameter giving smaller forward momentum. The Pt products from the 292 MeV energy projectile reaction are produced from the peripheral interaction and the forward momentum transfer is also small. Thus, the small momentum transfer from the primary reaction gives the same isotopic effects for the products from the 1.0 GeV ^{12}C+ ^{238}U reaction and the Pt products from

the 292 MeV C + Au reaction. Thus, the large primary momentum transfer results in the isotopic effects opposite to those resulted by the small primary momentum transfer.

IV Computational Evaluations

The experimental measurements of the angular distributions of the residual target nuclei described here encourage us to investigate a reaction model to explain the results. The angular distributions are especially interesting in relation to impact parameters. Even simple geometric computations may give some insights into such nuclear reactions (Fig. 19). The angular distributions of the heavy nuclides produced from the reactions with large impact parameters show that the largest forward momentum transfer occurs to the product with mass number around 175 in the experiment of the 3.0 GeV energy projectile with the Au target. The steepest forward peaked angular distributions imply that, for the relatively heavy products, the forward momentum transferred to the target residue is largest, since the recoil momentum imparted by nucleon evaporation during the deexcitation of the residual nucleus gives approximately the same smearing effects among the peripheral reactions of different impact parameters. This experimental evidence will help us to test reaction models. Two extreme cases were tested here. One model is to treat the nucleus-nucleus reaction of the 250 MeV/nucleon projectile energy free as nucleon- nucleon scattering. The scattered nucleon penetrates the participant volume and (Fig.20) reaches the residual volume, and finally leaves the volume, or sometimes will be stopped inside the volume with a certain probability. Assuming the scattering differential cross section between the nucleons of the target and projectile nucleus, $d\sigma/d\Omega(\vartheta)$, to be the free p-p scattering cross section, the angular distributions of the target residues were computed for the different impact parameters. The other model is to treat the participant part of the target nucleus as a collective volume throughout the primary interaction. The binding energy was computed between the participant volume and the residual

volume over the abraded surface. The potential energy was calculated with respect to the displacement between the two volumes. The residual volume receives a forward momentum for each impact parameter.

The p-p scattering model does not seem applicable to the experimental results of the angular distributions. The latter nuclear potential model, treating the interacting parts of the nucleus as a collective matter, seems more effective. Cumming[41] suggested that the nucleus can be viewed as a single object, instead of a group of independent nucleons, from a projectile at a relativistic kinetic energy, because of the Lorentz contraction.

IV-A Application of proton-proton Elastic Scattering

For the 250 MeV/nucleon energy (3 GeV ^{12}C), one of the projectile energies for our experiments from the Bevalac, the rotational and vibrational motion of the target nucleus can be ignored. Also, the Fermi energy of ^{197}Au, which is approximately 40 MeV, is far below the kinetic energy of nucleons of the projectile nucleus. Since the binding energy of a nucleon in the nucleus is ~8 MeV, the reaction between two nuclei at 250 MeV/n incident energy will not result in the formation of a compound nucleus . The projectile nucleus residue will keep moving after the collision, leaving the rest of the projectile nucleus behind with the target nucleus. The part of the projectile nucleus participating in the collision will experience scattering with the nucleons of part of the target nucleus. Some of the scattering and scattered nucleons will penetrate the interacting volume and reach the target nucleus residue. The target nucleus residue will receive the momentum from those nucleons and will give rise to the angular distribution.

The following assumptions were used to pursue this scattering model:

1. All the nucleons were treated as protons in terms of the scattering cross section. 2. The motions of the nucleus and the Fermi motion of the nucleons were ignored during the primary interaction. 3. The nucleons were treated as free nucleons. 4. Only the first scattering was taken into account. The multiple scattering effects were ignored, although more sophisticated treatments use particular theories for multiple scattering[40,42]. 5. The number of nucleons along the beam direction inside the projectile and target nucleus remained unchanged during the primary reaction. The Fermi motion was ignored. 6. Only proton-proton elastic scattering was employed, although 250 MeV/n is

high enough to produce π-mesons by the scattering. The inelastic scattering is ~14 % at this energy[43] . The error from this assumption will be discussed later. 7. A clear-cut spherical nuclear shape was assumed and the R.M.S. radius was employed[44]. 8. The nuclear density inside the participant part was assumed unchanged from the original target nuclear density.

The analysis for the computation is described in Fig.21. The target and projectile nucleus are described by,

$$x^2+y^2+z^2=R^2 \text{.....eq.1}$$

$$x^2+y^2+z^2=r^2 \text{.....eq.2}$$

with the target radius, R=5.33fm and projectile radius, r=2.50fm. The projectile nucleus is described with the impact parameter, b, by the following equation,

$$(x-b)^2+y^2+z^2=r^2 \text{....eq.3}$$

At (x_0,y_0) inside the participant volume, the path lengths of the target and projectile nucleus in the beam direction are,

$$L_t=2\sqrt{R^2-x_0^2-y_0^2} \text{.....eq.4}$$

$$L_p=2\sqrt{r^2-(x_0-b)^2-y_0^2} \text{.....eq.5}$$

,respectively. The numbers of nucleons within the volume, $L_p dxdy$, is given, with the nuclear density, ρ_p, by

$$N_p=\rho_p L_p dxdy \text{.....eq.6}$$

where ρ_p is obtained from dividing the mass number by the spherical volume of the nucleus , ^{12}C. We must find the number of collisions at (x_0,y_0), when the projectile nucleus passes by the target nucleus. Nucleons of the projectile will interact with the target nucleons along the path length. The number of interactions of one nucleon of the projectile is given by,

$$N_t=\sigma_t\rho_t L_t \text{.....eq.7}$$

where σ_t is the 250 MeV proton- proton total cross section (elastic + inelastic)

and ρ_t is the original nucleon density of the target nucleus, obtained by dividing the mass number by the nuclear volume, $\frac{4}{3}\pi R^3$. The actual number of collisions along the z-direction at (x_0,y_0) is given by,

$$N=N_p x N_t \text{.....eq.8}$$

A scattering takes place at a point (x_0,y_0,z_0). The collision density inside the target nucleus volume is given by $d(x,y)=\frac{N}{L_t}$, eq.9

The straight trajectory of the scattering nucleon is given by,

$$\frac{x-x_0}{\sin\vartheta\cos\varphi}=\frac{y-y_0}{\sin\vartheta\sin\varphi}=\frac{z-z_0}{\cos\vartheta}\text{.....eq.10}$$

The scattering points, (x_0,y_0,z_0), are uniformly distributed along the beam direction, assuming there is no attenuation during the collision. Since we are dealing with only the elastic scattering, in the laboratory system, both the scattered and scattering nucleons should go forward beyond the scattering point, which means $z \geq z_0$ must be satisfied. With the assumption of a clear-cut abraded cylindrical surface produced by the nucleus-nucleus collision, the surface of the cylinder is given by,

$$(x-b)^2+y^2=r^2\text{.....eq.11}$$

The intersecting point of the line defined by eq. 10 with the surface given by eq. 11 is found to be,

$$x=\frac{B\pm\sqrt{\beta^2-AC}}{A}$$

$$y=y_0-x_0\frac{\sin\varphi}{\cos\varphi}+\frac{\sin\varphi}{\cos\varphi}\left\{\frac{\beta\pm\sqrt{\beta^2-AC}}{A}\right\}\text{.....eq.12}$$

$$z=\left\{\frac{\sin\varphi}{\cos\varphi}\frac{\beta\pm\sqrt{\beta^2-AC}}{A}-x_0\frac{\sin\varphi}{\cos\varphi}\right\}\frac{\cos\vartheta}{\sin\vartheta\sin\varphi}+z_0$$

where,

$$A=1+\frac{\sin^2\varphi}{\cos^2\varphi}$$

$$B=b+\frac{\sin^2\varphi}{\cos^2\varphi}x_0-\frac{\sin\varphi}{\cos\varphi}y_0$$

$$C=b^2+\frac{\sin^2\varphi}{\cos^2\varphi}x_0^2+y_0^2-r^2-2x_0y_0\frac{\sin\varphi}{\cos\varphi}$$

There are two physical situations to be considered. The scattering nucleon is recoiled and goes out without touching the target nucleus residual volume or it enters the residual volume. Since we are interested only in the scattering nucleons that go into the residual volume, the following condition must be satisfied to give the correct one of the + and - signs. The intersecting points, (x, y, z), must satisfy, $x^2+y^2+z^2\leq R^2$. Determining the point (x, y, z) as the entrance to the target residue, we find the distance from the scattering point to the entry point,

$$l_e=\left[(x-x_0)^2+(y-y_0)^2+(z-z_0)^2\right]^{\frac{1}{2}}\text{.....eq.13}$$

Now, we must find the path length of the scattered nucleon inside the target nucleus residue. Solving eq. 10, simultaneously with ,

$$x^2+y^2+z^2=R^2$$

we will find the point where the scattering nucleon goes out of the spherical target volume. This is given by,

$$x=\frac{-\beta\pm\sqrt{B^2-AC}}{A}$$

$$y=\left[\frac{-B\pm\sqrt{B^2-AC}}{A}-x_0\right]\text{.....eq.14}$$

$$z=\left[\frac{-B\pm\sqrt{B^2-AC}}{A}-x_0\right]\frac{\cos\vartheta}{\cos\varphi\sin\vartheta}+z_0$$

where,

$$A=\frac{1}{\cos^2\varphi\sin^2\vartheta}$$

$$B=-x_0\frac{\sin^2\varphi}{\cos^2\varphi}+y_0\frac{\sin\varphi}{\cos\varphi}-x_0\frac{\cos^2\vartheta}{\cos^2\varphi\sin^2\vartheta}+z_0\frac{\cos\vartheta}{\cos\varphi\sin\vartheta}$$

$$C=x_0^2\frac{\sin^2\varphi}{\cos^2\varphi}+y_0^2-2x_0y_0\frac{\sin\varphi}{\cos\varphi}+x_0^2\frac{\cos^2\vartheta}{\cos^2\varphi\sin^2\vartheta}+z_0^2-2z_0x_0\frac{\cos\vartheta}{\cos\varphi\sin\vartheta}-R^2$$

The obtained exit point (x, y, z) should satisfy the condition, $z \geq z_0$, because of the same reason as before. The scattering nucleon leaves the target volume at this point. The trajectory length of the scattering nucleon from the scattering point to the exit point is given by,

$$l_o=\left[(x-x_0)^2+(y-y_0)^2+(z-z_0)^2\right]^{\frac{1}{2}} \text{.....eq.15}$$

We must note that l_o should be larger than l_e, because we are not interested in the nucleons scattered in the positive x direction. A fraction of the scattering nucleons will be stopped by reacting with the nucleons of the target nucleus. The total proton-proton cross section, $\sigma_T(E)$, was found from the function,

$$S_t=Au^{-3}+Bu^{-2}+Cu^{-1}+D\text{....eq.16}$$

fitting the total cross section data from reference 41 by the least squares method. The variable, u, designates the kinetic energy of the scattering or scattered nucleon. The fraction of a nucleon to reach the target residual volume after the scattering is given by

$$P_1=\exp(-\sigma_T(E)l_e\rho_T)\text{.....eq.17}$$

and the fraction of a nucleon to leave the target nucleus volume is given by,

$$P_2=\exp(-\sigma_T(E)l_o\rho_T)\text{.....eq.18}$$

assuming the same nuclear density in the participant volume and residual volume of the target nucleus. σ_T is determined by the kinetic energy of the scattered nucleon and the kinetic energy is found from a given scattering angle, ϑ , at the first scattering, since the elastic scattering energy is only dependent on the scattering angle. Reference 45 shows the relativistic elastic scattering mechanics.

The relativistic relation for a proton with E_{Kin} = 250 MeV is,

$$(pc)^2=E_{Kin.}{}^2+2E_{Kin.}E_0$$

where m_p = proton mass and c = light speed.

With the momentum pc, we define,

$$E=M^2/2M=\frac{M}{2}$$

$$M=((2m_pc^2)^2+2m_pc^2E_{Kin})^{\frac{1}{2}}$$

In order to treat the mechanics in the C.M. system, we define,

$$p=(E^2-(mc^2)^2)^{\frac{1}{2}}$$

$$\beta'=p/E$$

$$\beta=(E_{Kin}^2+2m_pc^2E_{Kin})^{\frac{1}{2}}/(2m_pc^2+E_{Kin})$$

$$\gamma=(1-\beta^2)^{-\frac{1}{2}}$$

and the scattering angle $\Theta_{C.M.}$ is given by,

$$\Theta_{C.M.}=\cos^{-1}((-B+\frac{\sqrt{(B^2-AC)}}{A}))$$

Here

$$A=(1+\gamma\tan^2\Theta)\beta'^2$$

$$B=\beta\beta'\gamma^2\tan^2\Theta$$

$$C=\gamma^2\beta^2\tan^2\Theta-\beta'^2$$

where Θ is the scattering angle in the LAB system. Now, with given Θ_{LAB} , $\Theta_{C.M.}$ is calculated. With this scattering angle, $\Theta_{C.M.}$, the scattering energy is given by,

$$E_{Kin}=(\gamma E-m_pc^2)+p\beta\gamma\cos(\Theta_{C.M.})$$

Now given the scattering angle, Θ_{LAB}, the scattering energy is found through the calculation of $\Theta_{C.M.}$. The experimental data of the differential cross section, $d\sigma/d\Omega$, for the 250 MeV p-p elastic scattering in the C.M. system[43] were used to fit the function of the Legendre polynomials,

$$S_d=A+BP_2(\cos\Theta_{C.M.})+CP_4(\cos\Theta_{C.M.}),.....eq.19$$

The total cross section was computed from this function by integrating over Θ.

The comparison with the total elastic scattering cross section at 250 MeV in eq. 16 normalized the differential cross section function, eq.19. Also, conversion from the differential cross section in the C.M. system to those in the LAB system is given by $d\sigma/d\Omega(\Theta LAB) = \frac{d\sigma}{d\Omega}(\Theta_{C.M.}) \frac{\sin\Theta_{C.M.}}{\sin\Theta_{LAB}} (\frac{d\sigma}{d\Omega}(\Theta_{C.M.}) = S_d)$. Now, we have the scattering energy and the probability of a nucleon scattered in the given angle, Θ_{LAB}.

With the scattering energies at the different scattering angles, eq.16 gives the total cross sections. The nucleons scattered at 90° in C.M. have a very low scattering energy (~ 0 MeV) and give a very large total cross section. The correction was made to improve this situation by taking into account the Fermi motion of the target nucleons.

To calculate the Fermi motion levels of nucleons in the ^{197}Au nucleus, the energy levels of the harmonic oscillator model in ref. 46 were utilized. Only protons were taken into account. With a given momentum of the scattered nucleon, P (ϑ), (ϑ is the scattering angle in the LAB system at the first p-p scattering, accordingly $\vartheta=\Theta$), and the i-th oscillator level of the proton in the nucleus calculated from the oscillator model, P_i, the compound momentum is given by,

$$P(\vartheta)+P_i\sin\vartheta'\cos\varphi'$$

The momentum that was averaged over the different oscillator levels and the angles, ϑ' and φ' is,

$$<P(\vartheta)> = \frac{\sum_i n_i \int\int (P(\vartheta)+P_i\sin\vartheta'\cos\varphi')d\vartheta'd\varphi'}{4\pi N_p} \quad \text{.....eq.20}$$

where n_i is the number of protons on the i-th energy level of the oscillator model and N_p is the total number of protons. This averaged momentum gives the kinetic energy resulting from the relative motion between the scattered

nucleons and the nucleons of the target nucleus under Fermi motion. Eq.16 gives the total cross section for this averaged kinetic energy of the nucleon. Finally, the function of the scattered nucleons remaining in the target residual volume is given by,

$$d\sigma/\,d\Omega(\vartheta)=\int\int\int\int 2d(x_0,y_0)\frac{\sigma(\vartheta)}{\sigma_T}\sin\vartheta\Delta\vartheta(P_1-P_2)d\varphi dx_0dy_0dz_0$$

$$=\int\int\int\int f(x_0,y_0,z_0,\vartheta,\varphi)dx_0dy_0dz_0d\varphi.....\text{eq.21}$$

where

$$\sigma_T(E)=S_t$$

$$P_1=\exp(-\rho_T\sigma_T(E)l_e(x,y,z,\vartheta,\varphi))$$

$$P_2=\exp(-\rho_T\sigma_T(E)l_o(x,y,z,\vartheta,\varphi)$$

as given before. $\sigma(\vartheta)$ is the differential cross section for p-p elastic scattering at 250 MeV, which gives the scattering probability at the angle, ϑ, with normalization by σ_T. σ_T , shown in Fig.22 , is the total cross section for 250 MeV p-p scattering. The integrals of x_0,y_0,z_0 are over the participant volume of the target nucleus. φ is given by $\mathrm{Tan}^{-1}(\frac{y-y_0}{x-x_0})$ from eq.10, having the (x, y, z) to satisfy the conditions given before. The multiplication factor, 2, rises from the fact that, in p-p elastic scattering, we cannot distinguish the scattered protons from the scattering ones. Also, $\sin\vartheta$ comes from the fact that we are seeking the differential function with the ϑ variable, keeping the function out of the ϑ integral.

The momentum given to the target residues is calculated through multiplying the core of eq.21 by the momentum of a scattered proton. p is given by,

$$cp=(E_{Kin}(E_{Kin}+2m_pc^2))^{\frac{1}{2}}$$

$$P=\int cpf(x,y,z,\vartheta,\varphi)dxdydzd\varphi=\int cpf(V)dV.....\text{eq.22}$$

In this equation, E_{Kin} is the kinetic energy of the scattered nucleon and is a

function of the scattering angle, ϑ. The excitation energy of a target residue is given by multiplying E_{Kin} of a scattered nucleon instead of the momentum term, cp. However, we must note the relation, $\int E_{Kin} f(\Omega) d\Omega$= Recoil Energy + Excitation Energy. The recoil energy and excitation energy also depend on the azimuthal angle in this reaction model. Table XVII gives the computational results of the excitation energies and recoil energies of the target residual products with respect to the mass numbers. Fig.24 shows the result of the differential cross section of the product mass number 195, $d\sigma / d\Omega(\vartheta)$, for the impact parameter, b=7.11 fm. The largest value of the differential cross section occurs at the angle, ~41°, in the laboratory system. The total cross section rapidly increases at low kinetic energy as shown in Fig.22. The nucleons are scattered strongly in the forward direction and the scattered nucleons at large angles are attenuated very rapidly inside the participant volume. The nucleons must reach the residual volume to give recoil energy to the target . The nucleons can reach the volume only at small scattering angles corresponding to the small total cross section with a large kinetic energy (small attenuation). The calculated recoil energies using this model seem to be too small, since a large fraction of the scattering nucleons do not reach the residual volume because of the large attenuation in the participant volume.

Thus, the proton-proton elastic scattering model does not lead to a reasonable picture. As indicated above, proton-neutron or neutron-neutron scattering and the inelastic pion-production were not taken into account. However, the proton-neutron or neutron-neutron scattering effects[41,45] will give even less forward peaked distribution, since a larger fraction of the nucleons are scattered at large angles. Also, the pion[46] distribution will enhance the sideward peak of the distribution.

The program for this computation was tested as follows:

The computational result of the target residue angular distribution should be isotropic under the assumptions of the isotropic p-p differential cross section in the LAB system (*i.e.* S_d= const. in eq. 19) and the uniform attenuation of the scattering nucleons over axial angles inside the participant volume (*i.e.* P_1-P_2 = const. in eq. 21). Also, a steep forward peaked differential cross section and a steep sideward peaked cross section were used for S_d in eq. 19 instead of the approximately isotropic distribution (Fig. 23) used in this computation. The computational results showed a forward peak and sideward peak in the target residue angular distributions, respectively.

IV-B Application of Nuclear Potential Energy

The nuclear potential model was next applied to try to explain the forward momentum observed in the angular distribution measurements reported here. The 3.0 GeV ^{12}C (250 MeV/n) projectile and the ^{197}Au target were again used to apply this model. The binding energy of a nucleon in the nucleus is approximately 8 MeV. Since the kinetic energy of a nucleon of the projectile nucleus has much higher energy than the binding energy, the concept of the abrasion model is useful to understand the reaction mechanism. The Fermi motion was ignored for both the target and projectile nucleus. The idea for applying the nuclear potential energy to the relativistic nucleus-nucleus reaction is the following; When one nucleon is pulled out of the nucleus, the rest of the nucleus will be pulled together. According to the abrasion model, the projectile abrades a part of the nuclear volume away from the rest of the nucleus. The abraded volume may pull the rest of target nucleus in the same way as a nucleon pulled the nucleus. The recoil momentum was calculated from the intersection geometry of a cylindrical path of the projectile nucleus in the spherical target nucleus volume using the R.M.S. radii for the both projectile and target nucleus. The abraded surface area is described as a function of the displacement (Fig.20), as shown in Fig.25. Since all the nucleons inside a nucleus are in the nuclear potential energy, the residual nuclear volume is under the potential energy of the abraded volume. The square well potential with 1.4 fm width and -38.5 MeV depth[49] was used to compute the potential energy of the target nucleus residue with respect to the abraded part of the target. The abrasion process was treated as simple displacement of the partial volume of the target nucleus ignoring the addition of the volume from the projectile and even the shape of the abraded partial sphere was assumed unchanged. The computation

to find the potential energy of the target residue with respect to the abraded part is given by the equation;

$$V_0=-\int_P\int_T U(1.4)r^2r'^2\sin\vartheta\sin\vartheta'd\vartheta d\varphi drd\vartheta' d\varphi' dr'....eq.23$$

where U(1.4), square well potential, is defined by

$$U(1.4)=0.....R>1.4$$

$$U(1.4)=38.5.....R\leq 1.4$$

where $R=|\vec{r}-\vec{r}'|$. $\vec{r}'$ and $\vec{r}$ are the positions inside the target residual volume and the abraded volume, respectively.

The integral was carried out over the abraded volume of the target sphere, P, and the residual volume of the target, T. The value, V_0, is the depth of the potential energy of the residual volume with respect to the abraded volume.

The actual computation for the momentum given to the target residues in the beam direction goes as follows: Generally, the surface area is given by the equation,

$$S=\int_{x_1}^{x_2}\int_{y_1}^{y_2}\sqrt{1+(\frac{\partial z}{\partial x})^2+(\frac{\partial z}{\partial y})^2}dxdy....eq.24$$

The boundary conditions are found in the following way:

The target and projectile nuclei are described by the following equation as well as equations given in the previous section,

$$x^2+y^2+z^2=R^2.....eq.25$$

$$x^2+y^2+(z-b)^2=r^2.....eq.26$$

where R, r are the radii of the target nucleus and the projectile, respectively. b is the impact parameter. The cylindrical trajectory of the projectile nucleus is given by,

$$y^2+(z-b)^2=r^2.....eq.27$$

The projectile nucleus moves in the negative direction of x axis. The boundary conditions are calculated by using the equations for a circle in the y-z plane,

$$y^2+z^2=R^2 \text{.....eq.28}$$

Solving this with the use of eq.27, simultaneously, we obtain

$$Z_a=\frac{b^2+R^2-r^2}{2b} \text{.....eq.29}$$

Z_a is the largest Z component of the intersection between the projectile path and the target nucleus. With Z_a, the boundary condition for x and y are given by,

$$x_{1,2}=-(\pm\sqrt{R^2-Z_a^2-y^2})$$

$$y_{1,2}=-(\pm\sqrt{R^2-Z_a^2})$$

To find the surface area function dependent on the displacement, d, we need the equation,

$$(x+d)^2+y^2+z^2=R^2 \text{.....eq.30}$$

describing the part of the target nucleus under abrasion in the negative direction of the x-axis. The surface area function is given by,

$$f(d)=\int_{x_1}^{x_2}\int_{y_1}^{y_2}\sqrt{1+(\frac{\partial z}{\partial x})^2+(\frac{\partial z}{\partial y})^2}dxdy+2\int_{x'_1}^{x'_2}\int_{y'_1}^{y'_2}\sqrt{1+(\frac{\partial z}{\partial x})^2+(\frac{\partial z}{\partial y})^2}dxdy \text{..eq.31}$$

with boundary conditions,

$$x_1=-\sqrt{R^2-Z_a^2-y^2}$$

$$x_2=d-\sqrt{R^2-Z_a^2-y^2}$$

$$y_{1,2}=-(\pm\sqrt{r^2-(\frac{R^2-r^2-b^2-d^2/4}{2b})^2})$$

and

$$x'_{1,2}=-(\pm\sqrt{R^2-Z_a^2-y^2})$$

$$y'_1=\sqrt{r^2-(\frac{R^2-r^2-b^2-d^2/4}{2b})^2}$$

$$y'_2=\sqrt{R^2-Z_a^2}$$

The term, $\sqrt{r^2-(\frac{R^2-r^2-b^2-d^2/4}{2b})}$, is the value of the y-component of the intersection between the abraded part of the target and the residual part on

the abraded surface. In Fig.25, the abraded surface area of the target nucleus is shown as a function of the displacement, d, for the impact parameter, 5.61 fm. When the target nucleus is being abraded, the binding energy between the abraded volume and the residual volume is a function of the abraded surface area. The potential energy of the residual volume with respect to the abraded volume at displacement,d, is given by,

$$V(d)=V_0(1-\frac{f(d)}{S_a}).....eq.32$$

where V_0 is given by eq.23. f(d) is the abraded surface area function dependent on the displacement, d. S_a is the final abraded surface area at a given impact parameter and used as a normalization factor. According to the classical mechanics, the momentum and force are related by,

$$P=\int F(t)dt$$

where t is the time period when the force works on the target residue. The force is given using the potential energy,

$$F=-\frac{dV(r)}{dr}$$

finally,

$$P=-\int \frac{dV(r)}{dr}dt.....eq.33$$

where r is the displacement of the abraded volume and can be related to the time, t, by

$$r = v\,t \qquad eq.34$$

where v is the velocity of the abraded volume to be calculated from the momentum given by the primary collision and r denotes the displacement, d, in eq. 32. The following relations give the momentum estimates for the abraded part of the target nucleus.

$$P=P_{\Delta p}\Delta V_p/(\Delta V_T+\Delta V_P)$$

where

ΔV_T = abraded volume from the target

ΔV_P= abraded volume from the projectile

and

$P_{\Delta P}$= momentum carried by the projectile volume to be abraded through the collision.

The velocity of the abraded volume used in eq.33 is calculated from this momentum, by using the relativistic relation,

$$p=\frac{(\Delta V_T+\Delta V_P)\rho m_p v}{\sqrt{1-v^2/c^2}}$$

where ρ is the nucleon density of the original target nucleus.

The results giving recoil energies for five impact parameters are given in Table XVIII. The conversion from momentum to energy was simply given by,

$$E=\frac{p^2}{2M}$$

M is obtained from,

$$M=197x\frac{V_T-\Delta V_T}{V_T}$$

The general trend of the results is in good agreement with the trend implied from the experimental analysis based on the two step vector model. The computation was attempted only for impact parameters larger than 4.71 fm, which is the region, B, in Fig. 19.

IV-C Discussion of Computational Models

Use of the nucleon-nucleon scattering model failed to give correct estimates of the angular distributions. The basic assumption was to treat the nucleons of the projectile and target nucleus as free, independent nucleons. In the computation attempted here, only elastic proton-proton scattering was applied. However, consideration of the other factors, p-n, n-n scattering or even inelastic scattering (π-meson production) will not satisfactorily improve the results. The sideward peaked differential cross section of the target residue obtained by the computation is due to the extremely large total cross section at the low proton kinetic energy, as shown in Fig.22. The nucleons scattered from the primary reaction away from the target residual volume do not influence the residue, since, because of the large total cross section, the nucleons scattered at large angles with low kinetic energies are stopped before they reach the target residual volume. If the nucleons of the participant volume have a very high temperature caused by the projectile collision, a larger fraction of the scattered nucleons will reach the target residue, penetrating the participant volume. By taking into account this high temperature effect, the computation will be improved. Also, the approximately isotropic distribution of p-p elastic scattering function, shown in Fig. 23, was obtained by fitting the Legendre polynomials to the experimental data. The actual distribution function is more forward peaked. The results may be improved by introducing significantly forward peaked function for p-p scattering cross section. However, the difficulty in applying the free nucleon-nucleon scattering model to the explanation of the results of relativistic nucleus-nucleus reactions seems to imply that the nucleons cannot be treated as free for such relativistic nucleus-nucleus reactions[50].

On the other hand, upon treating the participating volume as a collective volume instead of a group of independent nucleons, which is the opposite extreme case, the computational results seem much more reasonable. The recoil energy estimates are close to the observed values. Our use of this model, with the recoil effects given by evaporation which was not included here , will give angular distributions consistent with the measurements. Our computation was done only for impact parameters larger than 4.71 fm. This impact parameter corresponds to the target residue mass number, 175. The computations at smaller impact parameters must be done to see if the recoil momentum decreases with the decrease of the impact parameter. However, this nuclear potential model may not be valid at impact parameters less than 4.71 fm. The momentum given to the edge of the residues (Fig.19) may remove this part from the rest of the target. Despite the lack of computations with impact parameters less than 4.71 fm, use of this reaction model gave reasonable agreement for values of the target recoil energies. In comparison with the p-p elastic scattering model, the collective treatment of the abraded parts seems more applicable.

V Conclusion

The first success of the measurements of the angular distributions from the Bevalac experiments have revealed interesting characteristics of the relativistic nucleus-nucleus reaction. Surprisingly, there were some common characteristics between the Bevalac energies and the other two lower energy experiments.

The angular distributions from the ^{197}Au target were all forward peaked. Steep forward-peaked angular distributions were observed for product mass number, ~160, from the reactions of 3.0 GeV and 12.0 GeV ^{12}C + ^{197}Au , and also the 1.0 GeV ^{12}C+^{197}Au reaction showed the steep distribution at mass number ~170. Even the reaction of 292 MeV ^{12}C+^{197}Au gave a similar trend of the angular distributions. Since only five nuclides were identified from the 25.2 GeV ^{12}C+^{197}Au reaction, we could not confirm this trend. The product mass number which corresponds to the steep forward angular distribution slightly shifts to the larger mass numbers with a decrease of the projectile energy. This shift may be due to the low mass density at the nuclear surface. The low kinetic energy projectile can knock off a small number of nucleons at the surface. It is interesting to note that the product mass number , ~170, which corresponds to the large derivative value of the angular distribution, corresponds to the change (from B to C in Fig. 19) for the geometric relation between the projectile and target nucleus. The cross section of the groove created by the projectile nucleus abrading the target exceeds the semi-circle. The target residual volume unlikely possesses the volume left from the simple geometric abrasion process by the projectile.

Two different types of angular distributions were observed from the ^{238}U target.

There were flat angular distributions of the fission products and forward angular distributions of the non-fission products. The forward angular distributions were produced from the same reaction process as with those of heavy products from ^{197}Au. The fission products were produced from excited target residues, from which several nucleons were chipped off by the primary interaction with the high energy projectile. The relativistic energy projectile transferred little momentum in this case and the angular distributions of the fission products were quite flat. The low energy (292 MeV, 1.0 GeV) projectile produced even steeper forward angular distributions, as the result of the transfer of the larger momentum to the target nucleus.

The angular distributions of the light products showed a slight, relative increase of the differential cross section at large angles in the 25.2 GeV $^{12}C+^{238}U$ reaction in comparison with the 3.0 GeV and 12.0 GeV reaction.

According to the model computations attempted here, the abraded parts of both the projectile and target nucleus behave as collective matter rather than as groups of the loosely linked nucleons.

Appendix A

The "catching probability" for the isotropic emission from the finite size of the target must be found for the calculation of the differential cross section. Fig. A-1 shows the diagram of the catcher foil disc and target plate placed parallel to each other.

The solid angle is generally obtained by use of the equation,

$$\int\int d\Omega=\int_{\varphi_1}^{\varphi_2}\int_{\vartheta_1}^{\vartheta_2} d\vartheta d\varphi \text{.....eq.A-1}$$

The boundary conditions are determined by the geometry of the catcher foil subtending from a point on the target. Taking a point on the target disc as it is shown in Fig. A-1, the boundary conditions were found for eq. A-1 as follows:

We easily find the relation,

$$\vartheta=\mathrm{Tan}^{-1}\frac{r}{h}\text{.....eq.A-2}$$

The projection of the catcher disc on the target plane with the coordinate origin at the point taken above gives the relation between r' and, φ, (r' is the radial component in the new coordinate)

$$(r'\cos\varphi+l)^2+r'\sin^2\varphi=a^2\text{.....eq.A-3}$$

given r'=r, the relation between φ and r is found,

$$\cos\varphi=\frac{a^2-l^2r^2}{2rl}\text{.....eq.A-4}$$

Eliminating r from eq.A-2 and eq. A-4 gives,

$$\cos\varphi=\frac{a^2-l^2h^2\tan^2\vartheta}{2lh\tan\vartheta}\text{.....eq.A-5}$$

For the case that the target is smaller than the catcher foil,

the boundary conditions are,

$$\varphi_1=0$$

$$\varphi_2=2\pi$$

From eq. A-5,

$$\vartheta = \mathrm{Tan}^{-1}\frac{-l\cos\varphi \pm \sqrt{l^2\cos^2\varphi - l^2 + a^2}}{h}$$

Taking + for the positive value of ϑ, finally,

$$\vartheta_1 = 0$$

$$\vartheta_2 = \mathrm{Tan}^{-1}\frac{-l\cos\varphi + \sqrt{l^2\cos^2\varphi - l^2 + a^2}}{h}$$

Considering the finite size of the target, the "catching probability" is given by,

$$P(W(\vartheta)) = \frac{\int_0^a 2\pi l\,dl \int_{\varphi_1}^{\varphi_2}\int_{\vartheta_1}^{\vartheta_2} W(\vartheta)\sin\vartheta\,d\vartheta\,d\varphi}{4\pi d^2\pi} \text{----....eq.A-6}$$

with $W(\vartheta) = 1$.

For the case that the target is larger than the catcher foil,

we need the equation,

$$P(W(\vartheta)) = \left[\int_0^a 2\pi l\,dl \int_0^{2\pi} d\varphi \int_{\vartheta_1}^{\vartheta_2} W(\vartheta)\sin\vartheta\,d\vartheta + \int_a^d 2\pi l\,dl \int_{\varphi'_1}^{\varphi'_2} d\varphi \int_{\vartheta'_1}^{\vartheta'_2} W(\vartheta)\sin\vartheta\,d\vartheta\right] / 4\pi\pi d^2$$

- eq.A-7

where $W(\vartheta) = 1$. The boundary conditions, $\vartheta'_{1,2}$ and $\varphi'_{1,2}$, are given on the basis of a similar analysis as before,

$$\vartheta'_1 = \mathrm{Tan}^{-1}\frac{-l\cos\varphi - \sqrt{l^2\cos^2\varphi - l^2 + a^2}}{h}$$

$$\vartheta'_2 = \mathrm{Tan}^{-1}\frac{-l\cos\varphi + \sqrt{l^2\cos^2\varphi - l^2 + a^2}}{h}$$

and

$$\varphi'_1 = \pi - \mathrm{Cos}^{-1}\frac{\sqrt{l^2 - a^2}}{l}$$

$$\varphi'_2 = \pi + \mathrm{Cos}^{-1}\frac{\sqrt{l^2 - a^2}}{l}$$

The average angle, $\langle\vartheta\rangle$, for each angular catcher foil was obtained using eq.A-6 or A-7, and setting $W(\vartheta) = \vartheta$.

$$\langle\vartheta\rangle=\frac{P(\vartheta)}{P(1)}$$

Obtaining $\langle\vartheta_1\rangle$, $\langle\vartheta_2\rangle$, and $\langle\vartheta_3\rangle$ for the catcher foil parts, a, b and c in Fig.3, respectively, the final average angles were found by the following relations, $\langle\vartheta_a\rangle=\langle\vartheta_1\rangle$, $\langle\vartheta_b\rangle=\langle\vartheta_2\rangle-\langle\vartheta_1\rangle$, $\langle\vartheta_c\rangle=\langle\vartheta_3\rangle-\langle\vartheta_2\rangle$ and $\langle\vartheta_d\rangle=\langle\vartheta_4\rangle-\langle\vartheta_3\rangle$. $\langle\vartheta_4\rangle$ was obtained by use of eq. A-6. The boundary conditions used for this purpose are $\vartheta_1=0$, $\vartheta_2=\pi$, $\varphi_1=0$ and $\varphi_2=2\pi$.

We can also find the relative activities on the angular catcher foils used in our experiments, knowing the angular distribution function, $W(\vartheta)$, in eq.A-6 and A-7.

The calibration factors were obtained by comparing the relative activities computed with the angular distribution function, $W(\vartheta)$, and the experimental measurements .

The error caused by the short recoil range of the heavy products in the target evaporation was computed by limiting the integral over ϑ, in this case the actual limitation of ϑ being given by,

$$\vartheta=\mathrm{Cos}^{-1}\frac{d}{r}$$

d is the depth at which the reaction takes place, and r is the recoil range for the product with the estimated recoil energy. The target thickness ($1\mathrm{mg/cm^2}$) was divided into ten layers and the accumulative effects were calculated to obtain the final correction factors beside the correction for the light products by the calibration experiment. The results show that the yield of the heavy products ($A\geq140$) was underestimated by 31 % to 89 % at the largest angle, depending on the recoil range estimates.

The average angles should have been found by iteration, considering the angular distribution function . To avoid the confusion of change of the average angles depending on the product nuclides, they were computed in the way described here, represented by the isotropic distribution. The largest error occurs at the smallest angle, since the angular distribution is very steep, which differs from the flat distribution. The error estimate shows that there is a 7° overestimate in the smallest angle for the very steep forward peaked angular distributions.

Appendix B

As the function to fit the measured angular distribution, $y=\frac{b}{\sin^c a\vartheta}$ was chosen. This function looks complicated to use as a fit function. Polynomials were attempted to fit the distribution, such as $y=a+bx^n+cx^m$, $y=a+bx^{-n}+cx^{-m}$, $y=a+b\exp(-cx)$, $y=a+bx+\exp(-cx)$ or $y=a+bP_2(x)+cP_4(x)$. None of them gave a satisfactory fit. The Legendre polynomials did not drop rapidly enough after fitting by the least square method. The x^n, x^{-n}-polynomials also had the same problems. Even the exponential term did not drop rapidly enough. Obviously, the difficulty is that we have only four data points in the angular distribution from the Bevalac experiments. We can include only less than four parameters in the function. Practically, three unknown parameters is the allowable number. The most important thing to obtain from the function fit is the derivative values at the forward angles. The function must drop rapidly enough to correspond with the measured results. In terms of using the function, $y=\frac{b}{\sin^c a\vartheta}$, we should note that the angular distributions given in the text already correspond to the differential cross sections. The use of the sin ϑ term is merely to fit a function to the measurements. There is no physical meaning for this function. $1/\sin\vartheta$ makes the function drop rapidly and gives a long tail, because sin ϑ remains small and becomes large only slowly at large ϑ. Besides, the factor,b, adjusts the horizontal scale. The power of c can produce any steep curve at small angles.

The fitting process must follow the least squares method. The least squares method for this function is described below. Knowing the partial derivatives of a, b and c, the following three equations must be simultaneously solved for a, b and c.

$$\frac{\partial s}{\partial a}=2\sum_i\left(\frac{b}{\sin^c a\vartheta_i}-y_i\right)\frac{-abc\sin^{c-1}a\vartheta_i\cos a\vartheta_i}{\sin^{2c}a\vartheta_i}=0..\text{eq.B}-1$$

$$\frac{\partial s}{\partial b}=2\sum_i\left(\frac{b}{\sin^c a\vartheta_i}-y_i\right)\frac{1}{\sin^c a\vartheta_i}=0....\text{eq.B}-2$$

$$\frac{\partial s}{\partial c}=2\sum_i\left(\frac{b}{\sin^c a\vartheta_i}-y_i\right)\sin^c a\vartheta_i\ln(\sin a\vartheta_i)=0...\text{eq.B}-3$$

Because of the non-linear relation between a, b and c, we cannot analytically solve this equation. We solved the equations with use of a computer: First, given a and c, we obtain b from eq.B-1. With the new b and using the same a, we get c from eq.B-2. With the new b and c, we find a from eq.B-3. And, then, we go back to eq.B-1. We continue this iteration until the three equations simultaneously go close to zero.

However, the convergence process was very slow and did not reach satisfactory conditions. So, in actual process we used only eq.B-1 and B-2, under the fixed c and the two equations were solved simultaneously to find a and b. Still, for some cases, the computation to solve the equations took a very long time. (The situation was not improved by choosing the other two sets of the equations.) The reason for this slow convergence was the extremely rapid drop of the function of eq.B-2 around the zero point. (intersection with the a -axis) as shown in Fig.B-1. Since we need only to find approximate values of the parameters, eq.B-2 was modified as,

$$\frac{\partial y}{\partial b}\leq 100$$

After obtaining a and b values with a given c, χ^2 was calculated with the following definition,

$$\chi^2=\sum_i(y(\vartheta_i)-y_i)^2\left[\frac{\frac{y_i}{\sigma_i}}{\sum_i\frac{y_i}{\sigma_i}}\right]\text{....eq.B-4}$$

where ϑ_i is the average angle of the data points in the measured angular distributions. y_i is the experimental yield at ϑ_i and σ_i is the standard deviation for y_i. Changing the value, c, with use of the computer we found the values, a, b and c to give the minimum χ^2 . Then, these values of a, b and c at the minimum χ^2 were taken as the parameters of the fit functions.

References

1. L. Wilets, E. Guth and J. S. Tenn, Phys. Rev. *156*, 1349, (1967)

2. J. Bisplinghoff, A. Mignerey, M. Blann, P. David and W. Scobel, Phys. Rev. C., *16*, 1058 (1977)

3. R.J. Otto, M.M. Fowler, D. Lee and G.T. Seaborg, Phys. Rev. Lett., *36*, 135 (1976)

4. U. Reus, A.M. Habbestad Wâtzig, R.A. Esterlund and P. Patzelt, Phys. Rev. Lett., *39*, 171 (1977)

5. A.M. Poskanzer LBL-Report 6586 (1977)

6. M. Gyulassy, LBL-Report 11040 (1980)

7. A.S. Goldhaber and H.H. Heckman, Ann. Rev. Nucl. Part. Sci. *28*, 161 (1978)

8. W.D. Myers and S. Landowne, LBL- Report 8612 (1979)

9. S. Nagamiya and M. Gyulassy, LBL-Report 14035 (1982)

10. W.D. Myers, Nucl. Phys., *A296*, 177 (1978)

11. W.G. Meyer, H.H. Gutbrod, Ch. Lukner and A. Sandoval, Phys. Rev. C, *22*, 179 (1980)

12. D.E. Greiner, P.J. Lindstrom, H.H. Heckman, B. Cork and F.S. Bieser, Phys. Rev. Lett., *35*, 152 (1975)

13. K.K. Gudima and V.D. Toneev, Sov. J. Nucl. Phys., *27*, 351 (1978)

14. A.A.Amsden, F.H. Harlow and J.R. Nix, Phys. Rev. C, *15*, 2059 (1977)

15. H.G. Baumgardt, J.U. Schott, Y. Sakamoto, E. Shcopper, H. Stocker, J. Hofmann, W. Scheid, W. Greiner, Z. Physik. *A 273*, 359 (1975)

16. J. Randrup, Phys. Lett., *76B*, 547 (1978)

17. J. Hufner and J. Knoll, Nucl. Phys., *77*, 460 (1977)

18. J. Gosset, H.H. Gutbrod, W.G. Meyer, A.M. Poskanzer, A. Sandoval, R. Stock and G.D. Westfall, Phys. Rev. C, *16*, 629 (1977)

19. Y. Yariv and Z. Fraenkel, Phys. Rev. C, *20*, 2227 (1979)

20. W. Loveland, R.J. Otto, D.J. Morrissey and G.T. Seaborg, Phys. Rev. Lett., *39*, No. 6, 320 (1977)

21. Y. Morita, W. Loveland, P.L. McGaughey and G.T. Seaborg, Phys. Rev. C, *26*, 511 (1982)

22. J.T. Routti, UCRL-Report 19452, (1969)

23. D.J. Morrissey, D. Lee, R.J. Otto and G.T. Seaborg, Nucl. Inst. Methods., *158*, 499 (1979)

24. W. Loveland, R.J. Otto, D.J. Morrissey and G.T. Seaborg, Phys. Lett., *69B*, 284 (1977)

25. S.B. Kaufman, E.P. Steinberg, B.D. Wilkins and D. J. Henderson, Phys. Rev. C, *22*, 1897 (1980)

26. L.C. Northcliffe and R.F. Schilling, Nucl. Data, *A7*, 233 (1970)

27. F. Hubert, A. Fleury, R. Bimbot and D. Gardes, Supplement aux Annales de Phys., *5*, 1 (1980)

28. W. Loveland, C. Luo, P.L. McGaughey, D.J. Morrissey and G.T. Seaborg, Phys. Rev. C, *24*, 464 (1982)

29. R. Vandenbosch, H. Warhanek and J.R. Huizenga, Phys. Rev., *124*, 846 (1961)

30. R. Gunnink and J.B. Niday UCRL-51061 (1972) implemented for use at CERN and Oslo by B. Erdal and O. Scheidemann.

31. J.O. Rasmussen, R. Donangelo and L. Oliveira, LBL-Report 6580 (1977)

32. L.F. Oliveira, R. Donangelo and J.O. Rasmussen, Phys. Rev. C, *19*, 826 (1979)

33. T. Lund, D. Molzahn, B. Bergersen, E. Hagebo, I.R. Haldorsen, C. Richard-Serre, Z. Phys. A, *306*, 43 (1982)

34. W. Loveland Private Communication

35. D.R. Fortney and N.T. Porile, Phys. Lett., *76B*, 553 (1978)

36. N.T. Porile, D.R. Fortney , S. Pandian, R.A. Johns, T. Kaiser, K. Wielgoz, T.S.K. Chang, N. Sugarman, J.A. Urbon, D.J. Henderson, S.B. Kaufman and E.P.

Steinberg, Phys. Rev. Lett., *43*, 918 (1979)

37. J.S. Stewart and N.T. Porile, Phys. Rev. C, *25*, 478 (1982)

38. Y.W. Yu and N.T. Porile, Phys. Rev. C, *12*, 938 (1975)

39. Y.W. Yu and N.T. Porile, Phys. Rev. C, *10*, 167 (1974)

40. H.C. Chiang, J. Hufner, Nucl. Phys. *A349*, 466 (1980)

41. J.B. Cumming, Phys. Rev. Lett., *44*, 17 (1980)

42. R.J. Glauber, Lecture in Theor. Phys. edited by W.E. Brittin and L.G. Dunham, (Interscience, N.Y., 1958)

43. W.N. Hess, Rev. Mod. Phys., *30*, 368 (1958)

44. H. Uberall, Electron Scattering from Complex Nuclei, Vols. A and B, Academic Press, N.Y., 1971

45. P.E. Hodgson and R.N. Maddison, Oxford Kinematical Tables, Rutherford High Energy Lab. (1961)

46. C.M. Lederer and V.S. Shirley, Table of Isotopes, Seventh Ed., (1979)

47. M.H. Hull, K.E. Lassila, H.M. Ruppel, F.A. McDonald and G. Breit, Phys. Rev., *122*, 1606 (1961)

48. L. Orphanos, J. Kalne, R. Altemus, P.C. Gugelot, J.S. McCarthy R.C. Minehart, P.A.M. Gram, B. Hoistad, C.L. Morris, E.A. Wadlinger and C. Perdrisat, Phys. Rev. Lett., *46*, 1562 (1981)

49. P. Marmier and E. Sheldon, Physics of Nucl. and Paricles, Vol. II, Academic Press, 1969

50. J. Hufner, K. Schafer and B. Schurmann, Phys. Rev. C, *12*, 1888 (1975)

Figure captions

Fig. 1. Schematic figure of relativistic heavy ion nuclear reaction showing three separate parts, A, B, C after the primary reaction.

Fig. 2. Schematic figure of target-catcher foil assemblies used in the Bevalac experiments.

Fig. 3. Schematic figure showing analysis for computation of the "catching probability".

Fig. 4. Cross section figures in the beam plane of target and cylindrical catcher foil assemblies. The one above was for use in the 1 GeV ^{12}C energy experiment at CERN and the one below was for use in the 292 MeV ^{12}C energy experiment at the 88-inch cyclotron, LBL.

Fig. 5. Angular distributions of target fragments from the reaction of 25.2 GeV $^{12}C+ {}^{197}Au$. The curves show the fits of the function to the data points.

Fig. 6. Angular distributions of target fragments from the reaction of 12.0 GeV $^{12}C+ {}^{197}Au$. The curves show the fits of the function to the data points.

Fig. 7. Angular distributions of target fragments from the reaction of 3.0 GeV $^{12}C+ {}^{197}Au$. The curves show the fits of the function to the data points.

Fig. 8. Absolute values of derivatives of the fit functions at 26° with respect to the product mass number. $\square$ denotes the absolute derivatives from the 25.2 GeV $^{12}C+ {}^{197}Au$, X from 12.0 GeV, Δ from 3.0 GeV and o from 292 MeV reactions.

Fig. 9. Angular distributions of target fragments from the reaction of 1.0 GeV $^{12}C+ {}^{197}Au$. The curves show the fits of the function to the data points.

Fig. 10. Absolute values of derivatives of the fit functions at 26° with respect to the product mass number from the reaction of 1.0 GeV $^{12}C+^{197}Au$.

Fig. 11. Angular distributions of target fragments from the reaction of 292 MeV $^{12}C+^{197}Au$. The curves show the function fits.

Fig. 12. Angular distributions of target fragments from the reaction of 25.2 GeV $^{12}C+ ^{238}U$.

Fig. 13. Angular distributions of target fragments from the reaction of 12.0 GeV $^{12}C+ ^{238}U$.

Fig. 14. Angular distributions of target fragments from the reaction of 3.0 GeV $^{12}C+ ^{238}U$.

Fig. 15. The slope values of angular distributions at wide angles, $\frac{s(74°)-s(44°)}{74°-44°}$

X denotes the slopes from the 25.2 GeV $^{12}C+ ^{238}U$, O from 12.0 GeV and Δ from 3.0 GeV reactions.

Fig. 16. Angular distributions of target fragments from the reaction of 1.0 GeV $^{12}C+ ^{238}U$. The curves show the function fits.

Fig. 17. Absolute values of derivatives of the fit functions at 26° with respect to the product mass number from the reaction of 1.0 GeV $^{12}C+^{238}U$.

Fig. 18. Angular distributions of target fragments from the reaction of 292 MeV $^{12}C+ ^{238}U$.

Fig. 19. Abraded surface area and residual nucleus mass number as functions of the impact parameter in the reaction of $^{12}C+^{197}Au$. The geometric relations between the two nuclei are also shown. Region A is for an impact parameter larger than 7.83 fm. Region B is for an impact parameter range where the nuclear potential model computation was applied, $4.71 \leq b \leq 7.83$ fm. Region C is for an impact parameter between 4.71 and 2.83 fm. Region D is for an impact parameter less than 2.83 fm.

Fig. 20. Schematic figure showing the primary scattering point A, the point B for the scattered nucleon to enter the residual volume and the point C for the nucleon to leave the target nucleus. The distance d is the displacement used as a valuable in the computation of the nuclear potential model.

Fig. 21. Diagram showing the computation based on p-p elastic scattering. P is the projectile and T is the target nucleus. L_P is the path length of the projectile part interacting with the target and L_T is that of the target at (x_0, y_0).

Fig. 22. Least squares fit function of p-p total cross section used in the computations. The data were obtained from ref. 43.

Fig. 23. Least squares fit function of differential cross section of 250 MeV p-p elastic scattering used in the computation. The data were obtained from ref. 43.

Fig. 24. Computational result of angular distribution based on p-p elastic scattering for the reaction of 250 MeV/n $^{12}C+^{197}Au$ at the impact parameter 7.11 fm.

Fig. 25. Abraded surface area as a function of the displacement of the abraded part of the target nucleus with respect to the residual volume.

Fig. A-1. Diagram explaining the mathematics employed to compute the catching probability.

Fig. B-1. Behaviour of function G defined by $G=\log(\partial S/\partial b)$ for $\partial S/\partial b>0$ and $G=-\log(-\partial S/\partial b)$ for $\partial S/\partial b<0$ using $\partial S/\partial b$ in eq.B-2 as a function of a.

Table I. Differential cross section from the reaction of 25.2 GeV $^{12}C + ^{197}Au$, normalized at the average angle 74°.

Nuclide	Average Angle <θ>			
	23°	33°	44°	74°
^{44m}Sc	2.69±0.57	1.11±0.44	0.50±0.13	1.00±0.17
^{97}Ru	2.05±0.98	1.58±0.34	0.87±0.14	1.00±0.17
^{145}Eu	6.43±1.57	2.20±0.59	1.15±0.20	1.00±0.22
^{149}Gd	7.80±1.40	1.81±0.37	0.73±0.20	1.00±0.21
^{171}Lu	7.92±1.83	2.40±0.60	0.96±0.27	1.00±0.23

Table II. Least squares fit of $f = b/\sin^{c} a\,\theta$ to the angular distribution from the reaction of 25.2 GeV ^{12}C + ^{197}Au.

Nuclide	a	b	c	$df / d\theta$ (26°)
^{44m}Sc	0.1554	0.0848	1.2	-5.40
^{97}Ru	0.1568	0.1689	0.9	-3.61
^{145}Eu	0.1543	0.0230	2.0	-20.6
^{149}Gd	0.1634	0.0299	2.0	-29.3
^{171}Lu	0.1588	0.0100	2.4	-24.0

Table III. Differential cross section from the reaction of 12.0 GeV $^{12}C + ^{197}Au$, normalized at the average angle 74°.

Nuclide	Average Angle <θ>			
	23°	33°	44°	74°
^{89}Zr	2.78±0.72	2.78±0.50	0.67±0.17	1.00±0.22
^{90}Nb	3.21±0.50	3.03±0.35	1.54±0.15	1.00±0.14
^{97}Ru	2.15±0.53	1.29±0.21	1.26±0.11	1.00±0.13
^{145}Eu	4.29±1.14	2.29±0.43	1.14±0.29	1.00±0.14
^{149}Gd	9.33±1.58	3.00±0.58	1.67±0.25	1.00±0.33
^{155}Dy	9.60±2.26	5.15±0.58	2.77±0.31	1.00±0.27
^{167}Tm	5.87±1.27	2.73±0.47	1.13±0.20	1.00±0.27
^{170}Hf	4.73±0.73	2.03±0.42	1.97±0.29	1.00±0.19
^{181}Re	3.71±1.13	2.19±0.58	1.23±0.33	1.00±0.27

Table IV. Least squares fit of $f = b/\sin^{c} a\,\theta$ to the angular distribution from the reaction of 12.0 GeV $^{12}C + {}^{197}Au$.

Nuclide	a	b	c	df / dθ (26°)
^{89}Zr	0.1659	0.1927	1.0	-5.63
^{90}Nb	0.1685	0.2305	1.0	-6.64
^{97}Ru	0.1649	0.2996	0.7	-2.83
^{145}Eu	0.1649	0.0908	1.4	-10.6
^{149}Gd	0.1656	0.0225	2.2	-32.4
^{155}Dy	0.1671	0.0560	1.9	-31.5
^{167}Tm	0.1660	0.0328	1.9	-18.7
^{170}Hf	0.1656	0.0997	1.4	-11.5
^{181}Re	0.1658	0.1057	1.3	-8.74

Table V. Differential cross section from the reaction of 3.0 GeV ^{12}C + ^{197}Au, normalized at the average angle 74°.

Nuclide	Average Angle <θ>			
	23°	33°	44°	74°
^{89}Zr	2.25±0.27	1.31±0.09	1.06±0.05	1.00±0.04
^{90}Nb	2.49±0.18	1.77±0.09	1.55±0.05	1.00±0.03
^{97}Ru	3.13±0.20	1.53±0.13	2.08±0.06	1.00±0.05
^{123}I	4.04±0.16	2.27±0.07	2.24±0.03	1.00±0.02
^{145}Eu	6.26±0.37	5.19±0.26	3.19±0.15	1.00±0.07
^{149}Gd	6.17±0.21	4.06±0.11	3.48±0.05	1.00±0.05
^{152}Tb	4.28±0.31	3.68±0.16	2.80±0.08	1.00±0.05
^{155}Dy	7.00±0.28	5.82±0.19	4.64±0.09	1.00±0.05
^{167}Tm	8.21±0.36	4.91±0.17	5.01±0.09	1.00±0.07
^{170}Hf	7.23±0.56	5.58±0.27	3.71±0.14	1.00±0.08
^{171}Lu	5.00±0.52	4.03±0.16	2.87±0.10	1.00±0.06
^{181}Re	5.83±0.39	3.50±0.21	4.23±0.11	1.00±0.06

Table VI. Least squares fit of $f = b/\sin^{c}a\ \theta$ to the angular distribution from the reaction of 3.0 GeV $^{12}C + {}^{197}Au$.

Nuclide	a	b	c	df / dθ (26°)
^{89}Zr	0.1611	0.2988	0.7	-4.23
^{90}Nb	0.1674	0.2835	0.8	-4.41
^{97}Ru	0.1661	0.2562	0.9	-5.82
^{123}I	0.1664	0.1989	1.1	-8.26
^{145}Eu	0.1691	0.2009	1.3	-16.2
^{149}Gd	0.1683	0.1888	1.3	-15.3
^{152}Tb	0.1704	0.2405	1.1	-18.6
^{155}Dy	0.1691	0.3853	1.1	-15.7
^{167}Tm	0.1670	0.3182	1.2	-18.6
^{170}Hf	0.1683	0.2270	1.3	-18.4
^{171}Lu	0.1683	0.2689	1.1	-11.0
^{181}Re	0.1684	0.3016	1.1	-12.4

Table VII. Differential cross section from the reaction of 1.0 GeV $^{12}C + {}^{197}Au$, normalized at the average angle 71°.

Nuclide	Average Angle <θ>								
	21°	32°	44°	57°	71°	114°	133°	148°	159°
^{59}Fe		2.47±1.05	1.31±0.20	1.22±0.15	1.00±0.10	1.01±0.08	1.06±0.12	1.09±0.24	0.91±0.04
^{74}As	1.91±0.22	1.78±0.08	1.37±0.06	1.14±0.03	1.00±0.03	0.89±0.06	0.96±0.06	0.98±0.07	0.96±0.05
^{75}Se	2.00±0.28	1.64±0.23	1.34±0.10	1.16±0.08	1.00±0.04	0.91±0.03	0.94±0.11	0.90±0.08	0.97±0.05
^{77}Br	1.61±0.41		1.18±0.33	1.19±0.22	1.00±0.19	0.90±0.07	0.73±0.36	0.89±0.08	1.09±0.01
^{83}Rb	1.97±0.08	1.75±0.12	1.33±0.09	1.15±0.04	1.00±0.05	0.88±0.03	0.95±0.12	0.86±0.04	0.95±0.05
^{84}Rb	2.71±0.77	2.22±0.46	1.59±0.19	1.22±0.06	1.00±0.03	0.88±0.02	0.95±0.07	0.95±0.05	1.02±0.05
^{87}Y	1.86±0.07	1.73±0.19	1.34±0.06	1.15±0.04	1.00±0.06	0.88±0.02	0.83±0.02	0.86±0.03	0.79±0.04
^{88}Y	2.26±0.80	2.00±0.47	1.33±0.17	1.16±0.10	1.00±0.07	0.91±0.05	0.91±0.11	0.91±0.06	1.00±0.04
^{88}Zr	1.70±0.21	1.68±0.14	1.32±0.08	1.15±0.04	1.00±0.03	0.82±0.02	0.81±0.10	0.75±0.05	0.62±0.06
^{89}Zr	1.86±0.39	1.75±0.09	1.39±0.12	1.16±0.05	1.00±0.04	0.87±0.01	0.84±0.04	0.85±0.04	0.80±0.04
^{95}Zr	2.63±0.80	2.08±0.41	1.47±0.24	1.29±0.28	1.00±0.12	0.91±0.06	1.18±0.16	1.21±0.13	1.37±0.30
^{95}Nb	2.04±0.14	1.85±0.13	1.42±0.12	1.22±0.17	1.00±0.07	0.95±0.07	1.00±0.10	1.05±0.07	1.08±0.10
^{97}Ru	1.53±1.17	2.96±1.16	1.33±0.16	1.21±0.09	1.00±0.14	0.88±0.17	0.75±0.14	0.68±0.07	0.68±0.07
^{111}In	2.54±1.17	1.95±0.48	1.46±0.14	1.17±0.05	1.00±0.09	0.71±0.02	0.59±0.03	0.59±0.07	0.59±0.09
^{121}Te	2.26±0.46	2.07±0.29	1.64±0.20	1.31±0.13	1.00±0.12	0.60±0.05	0.46±0.07	0.40±0.06	0.40±0.06
^{145}Eu	15.1 ±0.64	10.4 ±0.73	5.29±0.32	2.48±0.12	1.00±0.03	0.22±0.02	0.24±0.02	0.14±0.02	0.10±0.02
^{147}Eu	25.0 ±1.75	16.2 ±1.17	6.23±0.66	3.43±0.26	1.00±0.13				

^{146}Gd	19.9±1.11	12.9±0.59	6.02±0.28	2.67±0.10	1.00±0.06				
^{147}Gd	16.7±1.29	11.6±3.30	5.50±0.36	2.49±0.12	1.00±0.20				
^{149}Gd	23.5±0.34	14.9±0.27	6.67±0.17	2.80±0.04	1.00±0.03	0.22±0.02	0.25±0.01	0.17±0.02	
^{155}Tb	29.5±1.73	17.9±0.64	7.30±0.49	2.95±0.22	1.00±0.07	0.20±0.01	0.22±0.01	0.18±0.02	0.13±0.03
^{167}Tm	36.0±0.91	20.9±0.66	8.57±0.10	3.33±0.11	1.00±0.04	0.14±0.01	0.22±0.01	0.14±0.03	
^{169}Yb	33.7±1.69	19.5±1.07	8.42±0.37	3.22±0.16	1.00±0.08				
^{171}Lu	30.3±0.47	18.3±0.24	8.09±0.12	3.20±0.10	1.00±0.03	0.16±0.02	0.24±0.03	0.18±0.03	0.20±0.02
^{175}Hf	24.4±0.52	15.7±0.30	7.63±0.14	3.14±0.10	1.00±0.05	0.24±0.02	0.36±0.01	0.26±0.02	
^{185}Os	16.0±1.14	11.8±0.82	7.02±0.42	3.14±0.19	1.00±0.05	0.12±0.01	0.25±0.03	0.14±0.03	0.16±0.03
^{188}Pt	17.9±0.43	13.2±0.25	7.22±0.16	3.30±0.09	1.00±0.04				
^{191}Pt	11.9±0.61	9.3±0.87	4.85±0.46	2.50±0.15	1.00±0.11	0.36±0.06	0.43±0.06	0.37±0.11	0.41±0.15

Table VIII. Least squares fit of $f=b/\sin^{c}a\ \theta$ to the angular distributions from the reaction of 1.0 GeV ^{12}C + ^{197}Au.

Nuclide	a	b	c	$df / d\theta$ (26°)
^{59}Fe	0.0130	0.1088	0.6	-3.12
^{74}As	0.0219	0.2781	0.4	-1.55
^{75}Se	0.0182	0.2582	0.4	-1.55
^{77}Br	0.0415	0.4461	0.3	-0.97
^{83}Rb	0.0165	0.2495	0.4	-1.56
^{84}Rb	0.0038	0.0147	0.8	-4.19
^{87}Y	0.0161	0.1490	0.5	-1.92
^{88}Y	0.0092	0.0441	0.7	-3.16
^{88}Zr	0.0158	0.1396	0.5	-1.81
^{89}Zr	0.0161	0.1501	0.5	-1.94
^{95}Zr	0.0125	0.0617	0.7	-3.55
^{95}Nb	0.0260	0.1332	0.6	-2.53
^{97}Ru	0.0107	0.1316	0.5	-2.08
^{111}In	0.0010	0.0047	0.8	-3.85
^{121}Te	0.0010	0.0043	0.8	-3.69
^{145}Eu	0.2676	0.1226	2.1	-47.5
^{147}Eu	0.4078	0.2731	2.4	-83.0
^{146}Gd	0.3068	0.1707	2.2	-63.4
^{147}Gd	0.2764	0.1449	2.1	-52.5
^{149}Gd	0.3984	0.2426	2.4	-78.0
^{155}Tb	0.4868	0.3450	2.6	-100.7
^{167}Tm	0.5023	0.4536	2.6	-122.1
^{169}Yb	0.4928	0.4045	2.6	-114.4
^{171}Lu	0.4980	0.3758	2.6	-103.5

$^{175}_{Hf}$	0.4216	0.2893	2.4	-81.2
$^{185}_{Os}$	0.2820	0.1846	2.0	-49.7
$^{188}_{Pt}$	0.2869	0.2135	2.0	-55.5
$^{191}_{Pt}$	0.1794	0.0965	1.8	-35.0

Table IX. Differential cross section from the reaction of 292 MeV ^{12}C + ^{197}Au, normalized at the average angle 74°.

Nuclide	Average Angle <θ>				
	10°	21°	32°	47°	74°
^{96}Nb	5.30±0.40	3.40±0.13	3.00±0.12	1.50±0.05	1.00±0.03
^{97}Zr	5.43±1.15	2.76±0.41	3.77±0.50	1.56±0.18	1.00±0.10
^{97}Ru	7.48±1.38	3.14±0.41	3.17±0.38	1.91±0.11	1.00±0.06
^{99}Mo	5.95±0.12	2.82±0.04	2.72±0.03	1.97±0.04	1.00±0.09
^{123}I	13.8 ±0.46	2.74±0.07	2.56±0.07	1.35±0.03	1.00±0.02
^{181}Re	17.7 ±3.10	4.10±0.70	4.00±0.87	2.30±0.30	1.00±0.20
^{194}Au	16.8 ±2.46	5.60±0.69	4.14±0.73	3.06±0.25	1.00±0.11
^{196}Au	2.34±0.53	2.13±0.17	0.99±0.14	1.30±0.08	1.00±0.04

Table X. Least squares fit of $f=b/\sin^{c}a\ \theta$ to the angular distribution from the reaction of 292 MeV ^{12}C + ^{197}Au.

Nuclide	a	b	c	df / dθ (26°)
^{96}Nb	0.1755	0.3254	0.8	-4.34
^{97}Zr	0.1758	0.3291	0.8	-4.38
^{97}Ru	0.1662	0.2074	1.0	-6.05
^{99}Mo	0.1683	0.3390	0.8	-4.67
^{123}I	0.1644	0.0874	1.4	-10.2
^{181}Re	0.1667	0.1609	1.3	-13.2
^{194}Au	0.1333	0.1720	1.2	-13.2
^{196}Au	0.1360	0.5231	0.4	-1.40

Table XI. Differential cross section from the reaction of 25.2 GeV ^{12}C + ^{238}U, normalized at the average angle 74° .

Nuclide	Average Angle <θ>			
	23°	33°	44°	74°
^{89}Zr	1.93±0.37	1.73±0.34	0.66±0.13	1.00±0.19
^{97}Zr	2.50±0.90	1.06±0.30	0.79±0.14	1.00±0.12
^{99}Mo	1.07±0.22	0.79±0.10	0.94±0.05	1.00±0.05

Table XII. Differential cross section from the reaction of 12.0 GeV ^{12}C + ^{238}U, normalized at the average angle 74°.

Nuclide	Average Angle <θ>			
	23°	33°	44°	74°
^{43}K	1.97±0.31	0.85±0.13	1.02±0.07	1.00±0.10
^{72}As	2.80±0.78	0.71±0.16	0.75±0.14	1.00±0.16
^{97}Zr	1.86±0.30	0.81±0.14	1.18±0.09	1.00±0.10
^{99}Mo	1.12±0.12	0.96±0.05	1.15±0.03	1.00±0.02
^{133}I	1.16±0.27	0.68±0.14	0.61±0.08	1.00±0.13
^{149}Gd	5.67±1.56	4.78±1.22	1.22±0.22	1.00±0.33

Table XIII. Differential cross section from the reaction of 3.0 GeV ^{12}C + ^{238}U, normalized at the average angle 74°.

Nuclide	Average Angle <θ>			
	23°	33°	44°	74°
^{43}K	1.15±0.11	0.94±0.05	1.08±0.03	1.00±0.03
^{72}As	1.13±0.20	0.89±0.09	1.01±0.08	1.00±0.09
^{89}Zr	0.80±0.17	0.66±0.07	0.77±0.05	1.00±0.05
^{97}Zr	0.84±0.10	0.80±0.04	0.96±0.03	1.00±0.04
^{99}Mo	1.05±0.02	0.88±0.01	1.04±0.01	1.00±0.01
^{133}I	1.13±0.12	0.89±0.06	1.04±0.04	1.00±0.05
^{149}Gd	2.34±0.28	1.73±0.13	1.68±0.07	1.00±0.08

Table XIV. Differential cross section from the reaction of 1.0 GeV $^{12}C + ^{238}U$, normalized at the average angle 71°.

Nuclide	Average Angle <θ>							
	21°	32°	44°	57°	71°	114°	133°	151°
^{28}Mg	3.32±0.26	2.27±0.48	1.76±0.21	1.18±0.08	1.00±0.08	0.61±0.07	0.47±0.04	0.61±0.07
^{46}Sc	3.66±0.74	1.70±0.24	1.11±0.33	1.15±0.16	1.00±0.18	0.92±0.23	0.69±0.08	0.89±0.11
^{48}Sc	1.65±0.23	1.37±0.08	1.25±0.07	0.98±0.12	1.00±0.13	0.81±0.18	0.79±0.08	0.82±0.19
^{59}Fe	1.50±0.05	1.50±0.04	1.21±0.04	0.98±0.06	1.00±0.03	0.85±0.03	0.78±0.05	0.74±0.03
^{74}As	1.68±0.16	1.57±0.11	1.36±0.07	1.17±0.04	1.00±0.07	0.93±0.03	0.86±0.04	0.80±0.04
^{75}Se	2.03±0.35	1.46±0.16	1.41±0.20	1.22±0.14	1.00±0.15	0.85±0.01	0.90±0.04	0.80±0.13
^{83}Rb	1.66±0.08	1.57±0.06	1.40±0.04	1.16±0.07	1.00±0.03	0.88±0.04	0.83±0.04	0.84±0.04
^{84}Rb	1.74±0.12	1.56±0.13	1.47±0.12	1.18±0.03	1.00±0.03	0.91±0.01	0.85±0.05	0.84±0.05
^{91}Sr	1.16±0.23	1.21±0.16	1.23±0.06	1.07±0.03	1.00±0.20	0.99±0.11	0.96±0.06	1.08±0.05
^{87}Y	1.81±0.11	1.72±0.09	1.45±0.13	1.23±0.08	1.00±0.10	0.83±0.08	0.83±0.13	0.86±0.07
^{88}Y	1.69±0.07	1.55±0.10	1.40±0.08	1.14±0.03	1.00±0.05	0.85±0.06	0.87±0.02	0.81±0.03
^{89}Zr	1.79±0.10	1.73±0.09	1.46±0.08	1.23±0.07	1.00±0.06	0.88±0.05	0.87±0.05	0.86±0.06
^{95}Zr	1.38±0.27	1.31±0.29	1.08±0.14	1.02±0.05	1.00±0.12	0.92±0.08	0.90±0.11	0.95±0.09
^{97}Zr	1.00±0.20	1.22±0.14	1.09±0.15	1.03±0.10	1.00±0.12	0.99±0.08	0.92±0.07	1.03±0.06
^{99}Mo	1.49±0.05	1.44±0.08	1.29±0.04	1.13±0.07	1.00±0.07	0.99±0.09	1.00±0.08	1.06±0.09
^{97}Ru	1.74±0.06	1.74±0.14	1.42±0.08	1.21±0.07	1.00±0.14	0.78±0.16	0.86±0.11	0.88±0.11
^{103}Ru	1.53±0.07	1.51±0.05	1.38±0.03	1.22±0.03	1.00±0.02	0.93±0.05	0.99±0.06	1.05±0.02

^{101m}Rh	1.77±0.39	1.70±0.31	1.50±0.19	1.26±0.06	1.00±0.27	0.79±0.08	0.80±0.08	0.76±0.16
^{105}Rh	1.42±0.08	1.40±0.05	1.26±0.05	1.14±0.04	1.00±0.03	0.96±0.05	1.01±0.14	1.05±0.04
^{112}Pd	1.38±0.12	1.15±0.17	1.17±0.14	1.12±0.15	1.00±0.04	1.07±0.06	1.02±0.08	1.12±0.05
^{105}Ag	1.84±0.17	1.70±0.17	1.43±0.43	1.21±0.08	1.00±0.12	0.79±0.13	0.89±0.10	
^{106m}Ag	1.67±0.27	1.73±0.26	1.44±0.12	1.33±0.11	1.00±0.05	0.84±0.09	0.80±0.05	0.82±0.04
^{110m}Ag	1.77±0.32	1.68±0.09	1.46±0.04	1.24±0.07	1.00±0.03	0.94±0.02	0.95±0.07	0.94±0.11
^{115}Cd	1.42±0.16	1.35±0.06	1.31±0.06	1.21±0.08	1.00±0.06	1.02±0.06	1.11±0.09	1.16±0.05
^{111}In	2.12±0.13	1.99±0.11	1.63±0.09	1.32±0.07	1.00±0.05	0.79±0.05	0.79±0.05	0.96±0.05
^{114m}In	1.60±0.17	1.58±0.06	1.48±0.12	1.28±0.08	1.00±0.08	0.93±0.06	0.93±0.07	0.90±0.03
^{117m}Sn	1.82±0.35	1.61±0.27	1.48±0.17	1.28±0.19	1.00±0.16	0.88±0.11	0.91±0.12	0.91±0.81
^{120m}Sb	1.97±0.17	1.75±0.17	1.53±0.12	1.32±0.05	1.00±0.05	0.88±0.02	0.96±0.03	0.98±0.05
^{122}Sb	1.68±0.09	1.65±0.05	1.43±0.05	1.28±0.03	1.00±0.02	0.96±0.02	1.03±0.06	1.09±0.04
^{124}Sb	1.44±0.07	1.44±0.01	1.43±0.07	1.21±0.11	1.00±0.04	1.06±0.07	1.06±0.10	1.04±0.09
^{126}Sb	1.25±0.27	1.38±0.20	1.31±0.18	1.23±0.15	1.00±0.21	1.06±0.10	1.13±0.15	1.11±0.26
^{128}Sb	0.96±0.29	1.09±0.20	0.97±0.17	1.12±0.29	1.00±0.27	0.97±0.09	0.98±0.05	1.09±0.12
^{119m}Te	1.89±0.11	1.91±0.06	1.63±0.11	1.36±0.10	1.00±0.04	0.81±0.04	0.92±0.02	0.88±0.06
^{121m}Te	1.85±0.05	1.85±0.10	1.58±0.04	1.35±0.04	1.00±0.06	0.91±0.02	0.95±0.04	0.85±0.04
^{132}Te	1.26±0.10	1.29±0.10	1.16±0.08	1.15±0.01	1.00±0.10	1.06±0.04	1.07±0.02	1.16±0.05
^{124}I	1.55±0.29	1.53±0.25	1.47±0.08	1.28±0.09	1.00±0.09	0.92±0.09	1.00±0.34	1.01±0.27
^{131}I	1.22±0.26	1.29±0.07	1.27±0.14	1.17±0.08	1.00±0.07	0.98±0.08	1.10±0.09	1.13±0.07
^{133}I	1.22±0.08	1.21±0.10	1.24±0.06	1.04±0.03	1.00±0.04	1.08±0.07	1.10±0.03	1.12±0.13

^{136}Cs	1.00±0.39	1.68±0.33	1.42±0.22	1.30±0.18	1.00±0.09	1.13±0.09	1.17±0.12	1.08±0.19
^{133m}Ba	1.46±0.45	1.57±0.27	1.36±0.14	1.28±0.11	1.00±0.07	1.08±0.16	1.00±0.15	1.10±0.11
^{140}Ba	1.23±0.07	1.22±0.07	1.28±0.03	1.21±0.04	1.00±0.03	1.08±0.04	1.13±0.09	1.15±0.05
^{139}Ce	2.42±0.10	2.21±0.07	1.86±0.12	1.50±0.08	1.00±0.06	0.80±0.06	0.94±0.06	0.82±0.04
^{146}Gd	6.05±0.36	4.32±0.22	3.01±0.17	1.97±0.11	1.00±0.13	0.51±0.03	0.53±0.08	0.52±0.05
^{153}Gd	3.80±0.93	3.24±1.11	3.33±0.93	1.88±0.30	1.00±0.42	0.93±0.50	0.92±0.56	0.85±0.42
^{169}Yb	8.29±0.62	6.30±0.57	4.69±0.95	2.32±0.43	1.00±0.13	0.47±0.08		

Table XV. Least squares fit of $f = b/\sin^{c}a\ \theta$ to the angular distributions from the reaction of 1.0 GeV $^{12}C + ^{238}U$.

Nuclide	a	b	c	$df/d\theta$ (26°)
^{28}Mg	0.1237	0.1522	1.0	-5.97
^{46}Sc	0.1090	0.1331	1.0	-5.93
^{48}Sc	0.0296	0.2669	0.4	-1.32
^{59}Fe	0.0370	0.2840	0.4	-1.28
^{74}As	0.0345	0.3036	0.4	-1.41
^{75}Se	0.0164	0.1526	0.4	-1.95
^{83}Rb	0.0346	0.3029	0.4	-1.41
^{84}Rb	0.0313	0.2995	0.4	-1.45
^{91}Sr	0.1693	0.9157	0.1	-0.26
^{87}Y	0.0226	0.2737	0.4	-1.51
^{88}Y	0.0314	0.2922	0.4	-1.41
^{89}Zr	0.0262	0.2904	0.4	-1.51
^{95}Zr	0.0878	0.6770	0.2	-0.57
^{97}Zr	0.2086	0.8701	0.1	-0.24
^{99}Mo	0.0882	0.7439	0.2	-0.62
^{97}Ru	0.0258	0.2832	0.4	-1.48
^{103}Ru	0.0788	0.5560	0.3	-1.00
^{101m}Rh	0.0218	0.1714	0.5	-1.90
^{105}Rh	0.1020	0.7441	0.2	-0.61
^{112}Pd	0.1423	0.9511	0.1	-0.28
^{105}Ag	0.0277	0.1954	0.5	-1.92
^{106m}Ag	0.0305	0.2994	0.4	-1.46
^{110m}Ag	0.0373	0.3321	0.4	-1.50

^{115}Cd	0.1399	0.8009	0.2	-0.61
^{111}In	0.0135	0.1553	0.5	-2.19
^{114m}In	0.0525	0.5118	0.3	-1.04
^{117m}Sn	0.0305	0.3078	0.4	-1.50
^{120m}Sb	0.0241	0.2986	0.4	-1.60
^{122}Sb	0.0596	0.5491	0.3	-1.07
^{124}Sb	0.1108	0.7879	0.2	-0.63
^{126}Sb	0.1638	0.9972	0.1	-0.28
^{128}Sb	0.2800	0.8570	0.1	-0.23
^{119m}Te	0.0224	0.1881	0.5	-2.06
^{121m}Te	0.0265	0.3068	0.4	-1.59
^{132}Te	0.1684	0.9625	0.1	-0.27
^{124}I	0.0732	0.5553	0.3	-1.02
^{131}I	0.1693	0.9641	0.1	-0.27
^{133}I	0.1836	0.9470	0.1	-0.27
^{136}Cs	0.2117	1.0288	0.1	-0.29
^{133m}Ba	0.1019	0.7934	0.2	-0.65
^{140}Ba	0.1923	0.9774	0.1	-0.27
^{139}Ce	0.0073	0.0737	0.6	-3.00
^{146}Gd	0.1188	0.1460	1.2	-12.8
^{153}Gd	0.1686	0.4447	0.8	-6.12
^{169}Yb	0.1815	0.0910	1.7	-23.8

Table XVI. Differential cross section from the reaction of 292 MeV ^{12}C + ^{238}U, normalized at the average angle 47°.

Nuclide	Average Angle <θ>			
	10°	21°	32°	47°
^{72}Zn	1.48±0.04	1.17±0.02	1.06±0.01	1.00±0.01
^{73}Ga	2.49±0.07	1.22±0.19	1.34±0.10	1.00±0.04
^{103}Ru	1.87±0.10	1.46±0.06	1.16±0.04	1.00±0.02
^{105}Rh	1.72±0.17	1.41±0.07	1.15±0.05	1.00±0.02
^{131}I	1.53±0.16	1.23±0.07	1.15±0.05	1.00±0.03
^{132}Cs	1.17±0.10	1.00±0.06	0.90±0.04	1.00±0.02
^{135}Xe	1.95±0.26	1.44±0.09	1.00±0.05	1.00±0.02

Table XVII. Recoil energy and excitation energy of target fragments estimated from the computation based on the p-p elastic scattering model for the reaction of 3.0 GeV ^{12}C + ^{197}Au.

Product Mass Number	Impact Parameter (fm)	Excitation Energy (MeV)	Recoil Energy (MeV)
181	5.31	238.5	1.76
184	5.61	203.6	1.28
187	5.91	168.9	0.88
190	6.21	134.6	0.55
192	6.51	100.7	0.31
194	6.81	68.1	0.14
195	7.11	38.2	0.04
196	7.41	14.1	0.006

Table XVIII. Recoil energies of the target fragments from the computation based on the nuclear potential model for the reaction of 3.0 GeV ^{12}C + ^{197}Au.

Impact parameter (fm)	Product mass number	Recoil energy (MeV)
4.71	174	13.2
4.83	175	12.7
5.61	184	5.3
6.33	191	1.8
7.23	196	0.1

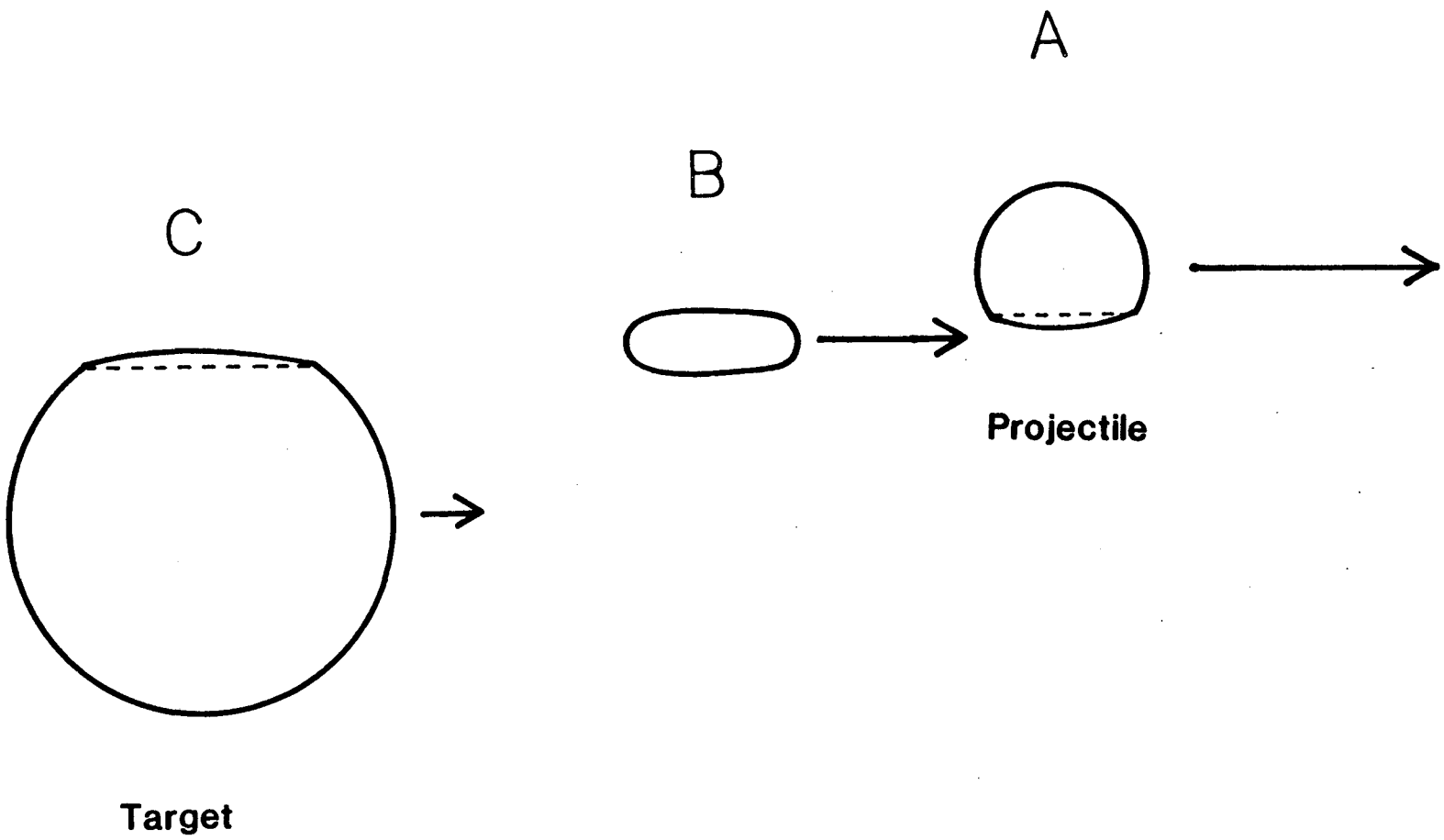

Fig.1

XBL 832-8356

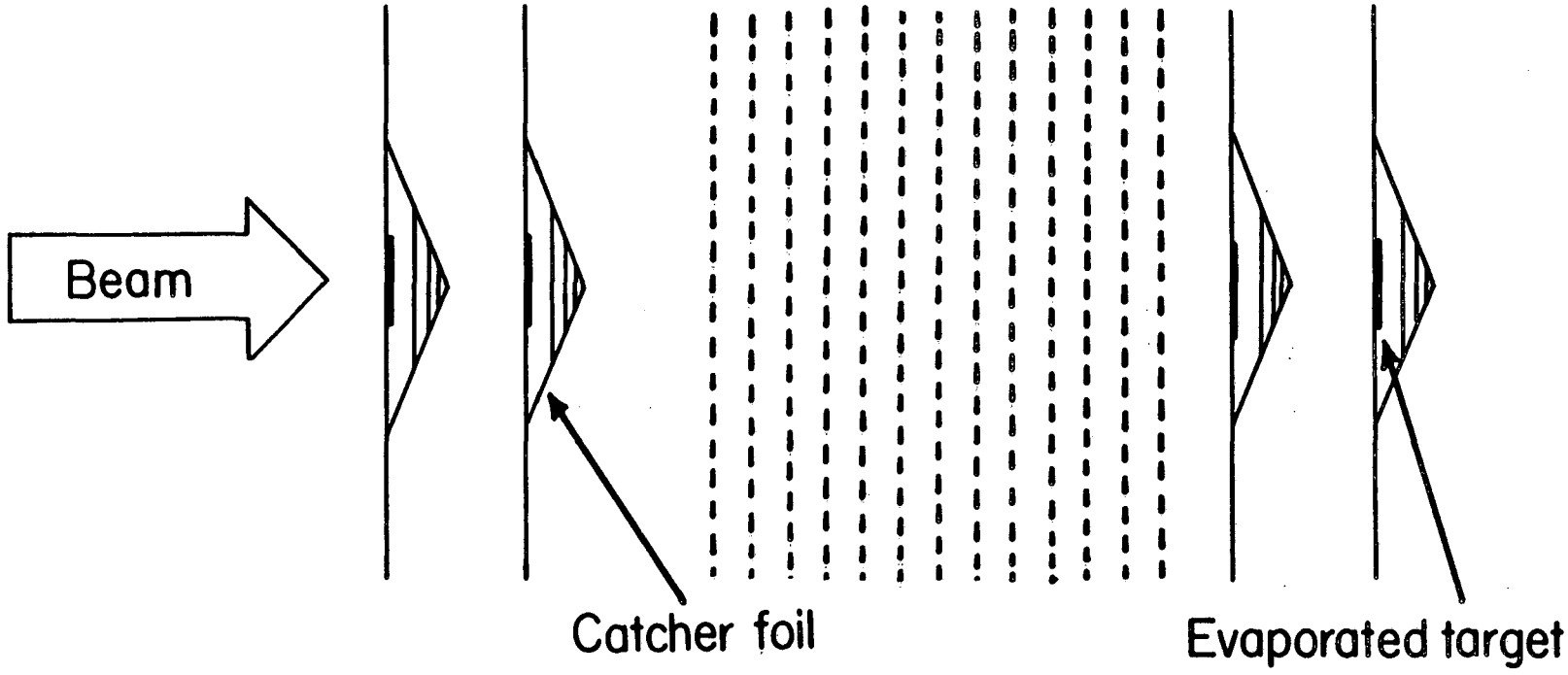

Fig.2

XBL 8110-1479

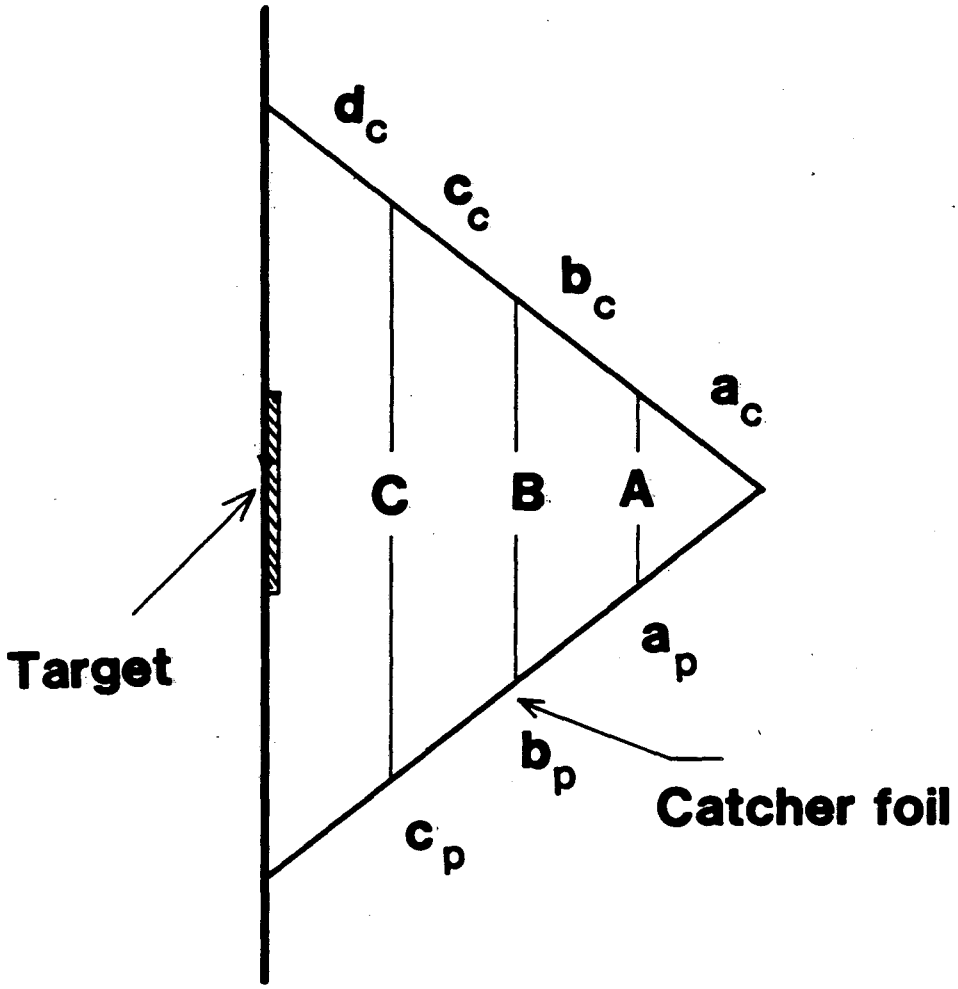

XBL 832-8149

Fig.3

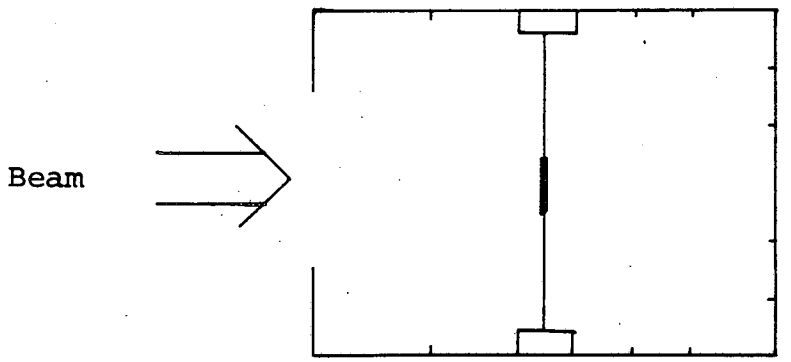

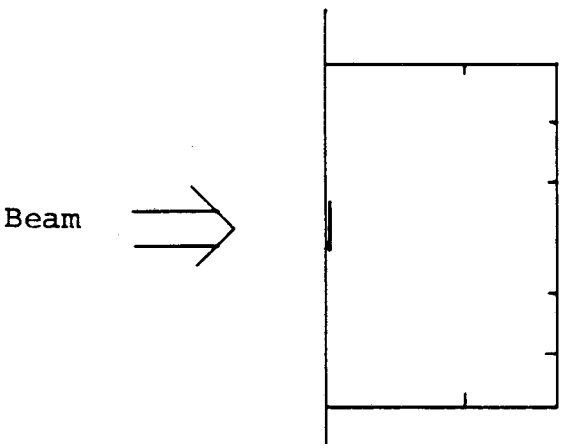

XBL 832-8243

Fig.4

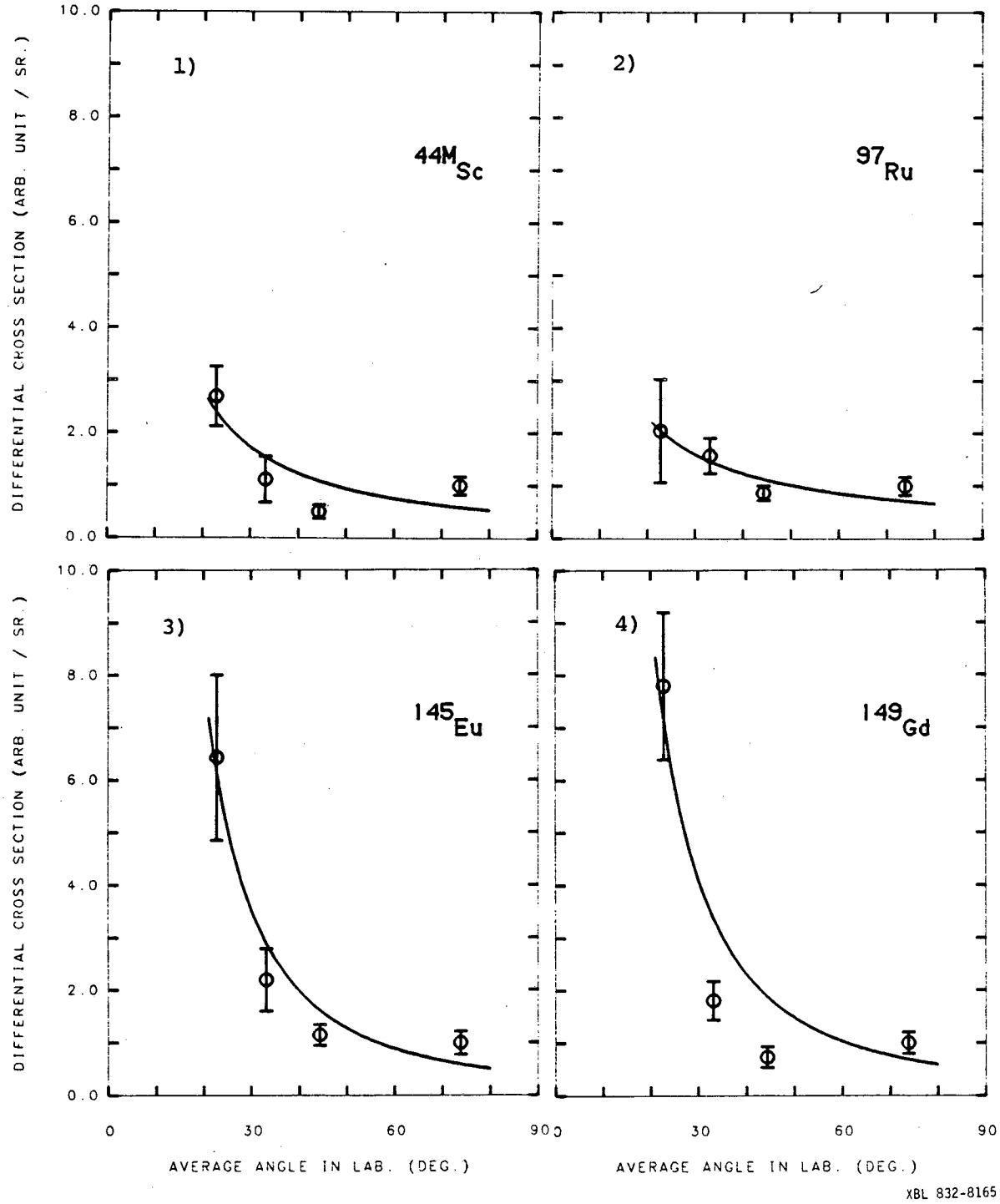
1)
^{44M}Sc
2)
^{97}Ru
3)
^{145}Eu
4)
^{149}Gd
DIFFERENTIAL CROSS SECTION (ARB. UNIT / SR.)
DIFFERENTIAL CROSS SECTION (ARB. UNIT / SR.)
10.0
8.0
6.0
4.0
2.0
0.0
0
30
60
90
AVERAGE ANGLE IN LAB. (DEG.)
AVERAGE ANGLE IN LAB. (DEG.)
XBL 832-8165

Fig.5

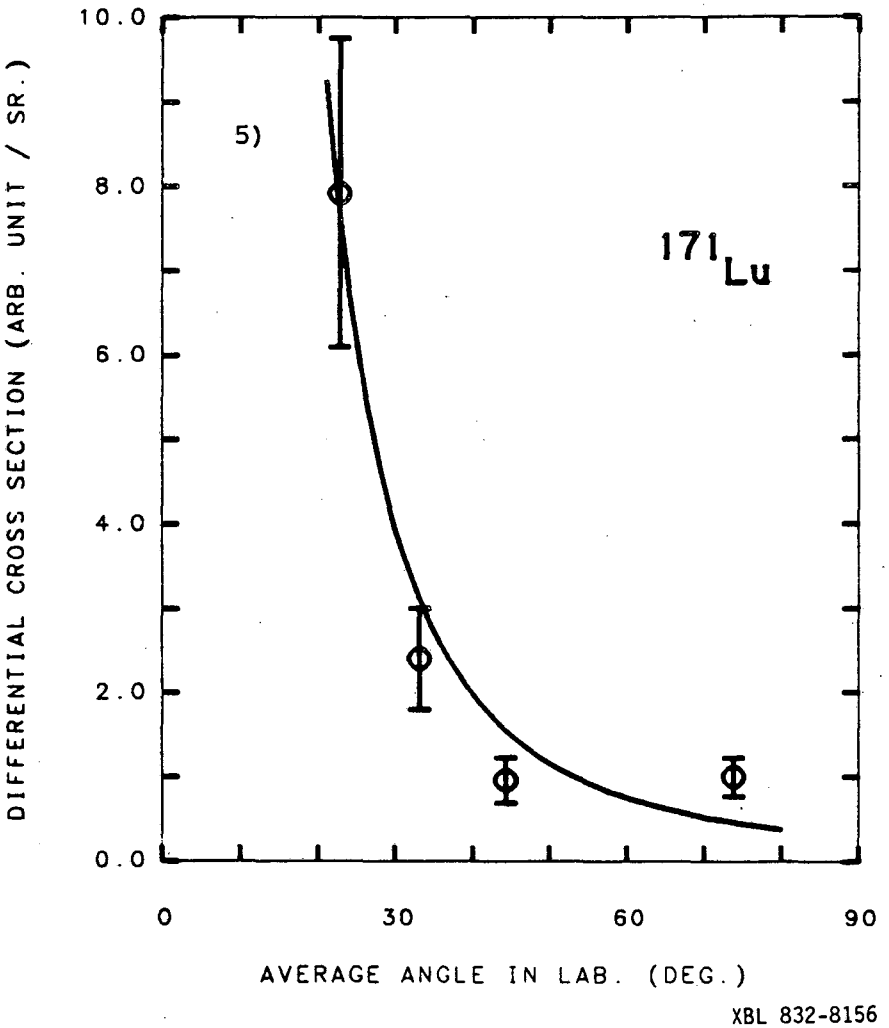
10.0
8.0
6.0
4.0
2.0
0.0
5)
171Lu
DIFFERENTIAL CROSS SECTION (ARB. UNIT / SR.)
0
30
60
90
AVERAGE ANGLE IN LAB. (DEG.)
XBL 832-8156

Fig.5

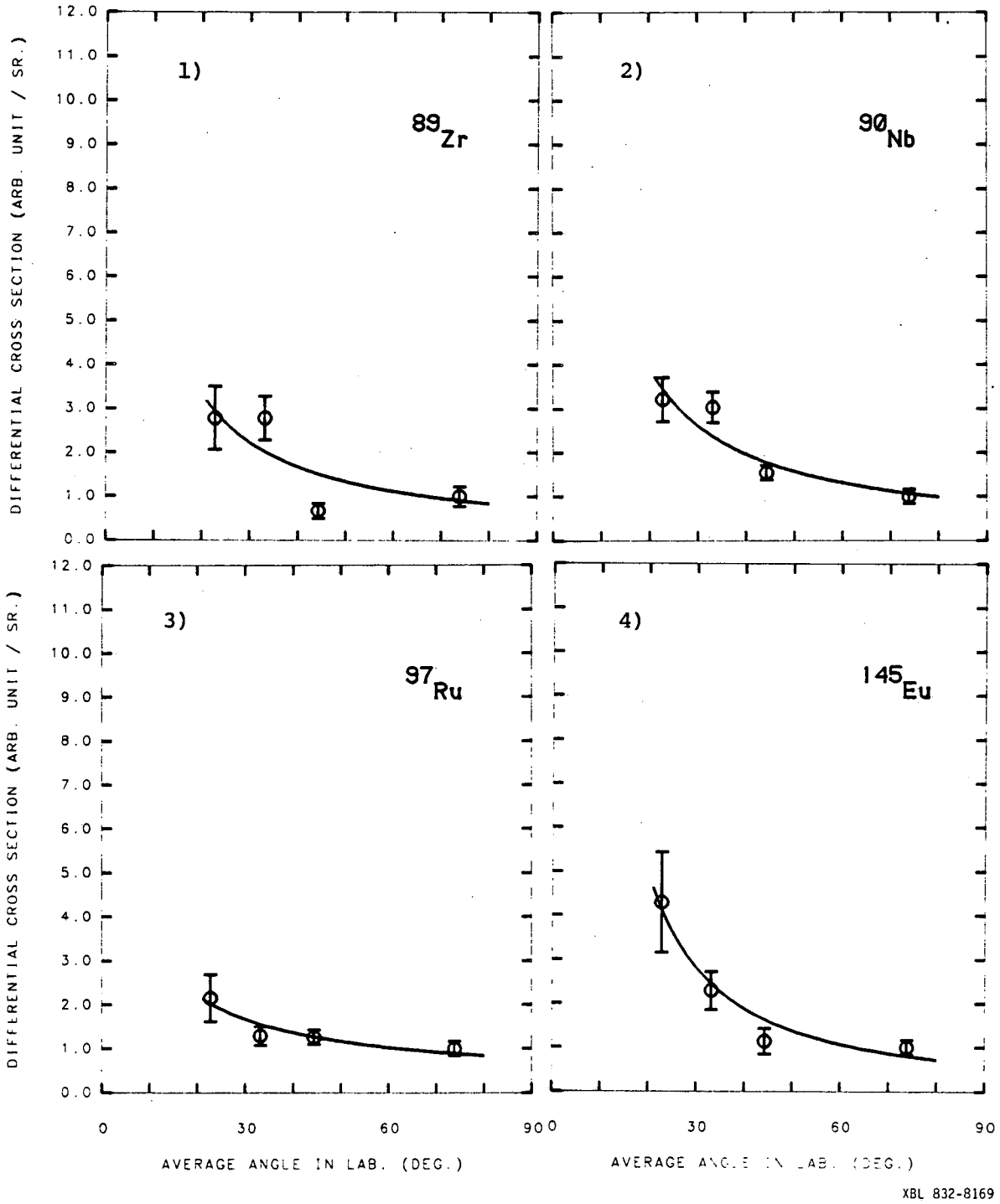
1)
^{89}Zr
2)
^{90}Nb
3)
^{97}Ru
4)
^{145}Eu
DIFFERENTIAL CROSS SECTION (ARB. UNIT / SR.)
AVERAGE ANGLE IN LAB. (DEG.)
0.0
1.0
2.0
3.0
4.0
5.0
6.0
7.0
8.0
9.0
10.0
11.0
12.0
0
30
60
90
XBL 832-8169

Fig.6

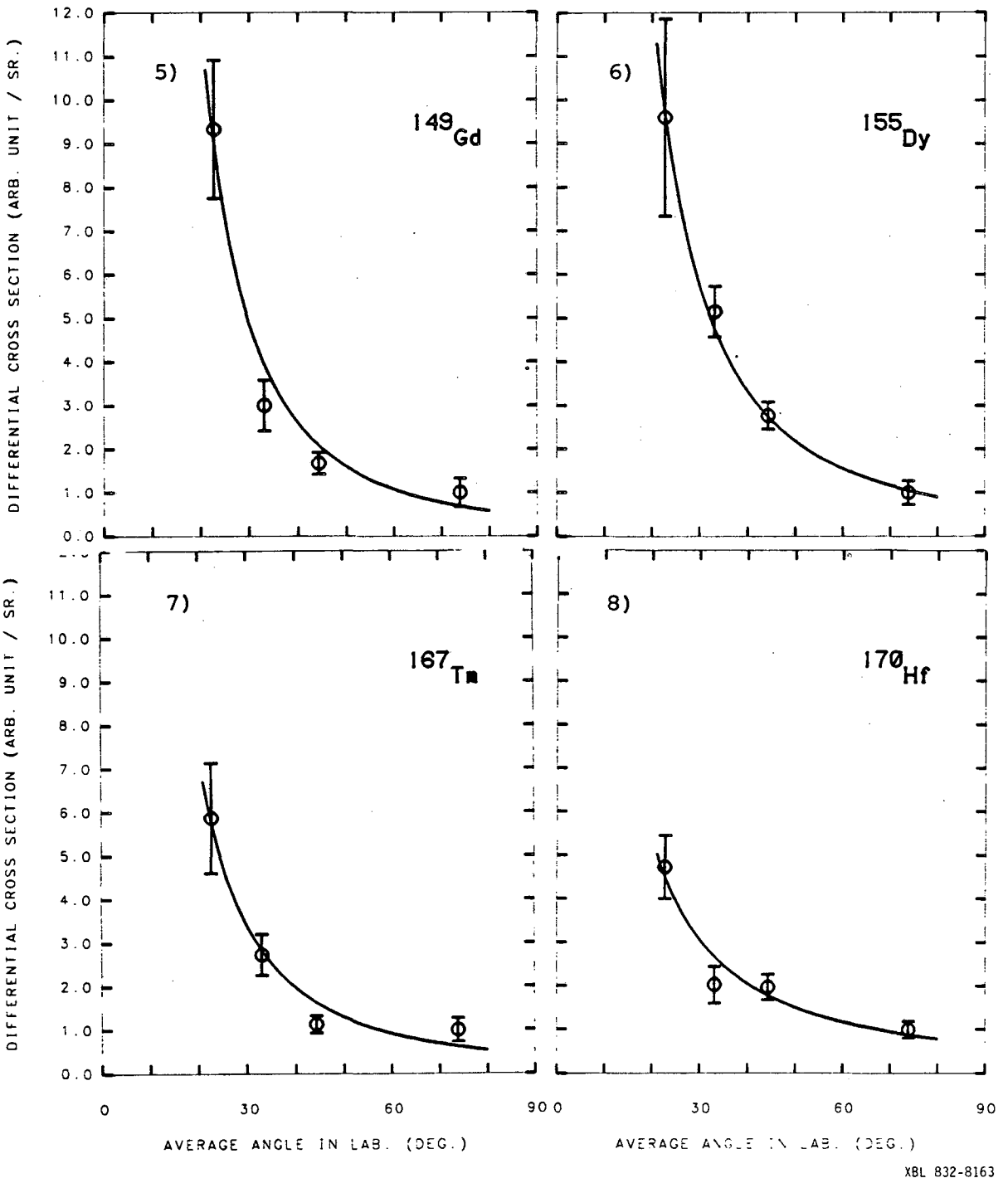
5) 149Gd
6) 155Dy
7) 167Tm
8) 170Hf
DIFFERENTIAL CROSS SECTION (ARB. UNIT / SR.)
AVERAGE ANGLE IN LAB. (DEG.)
0
30
60
90
XBL 832-8163

Fig.6

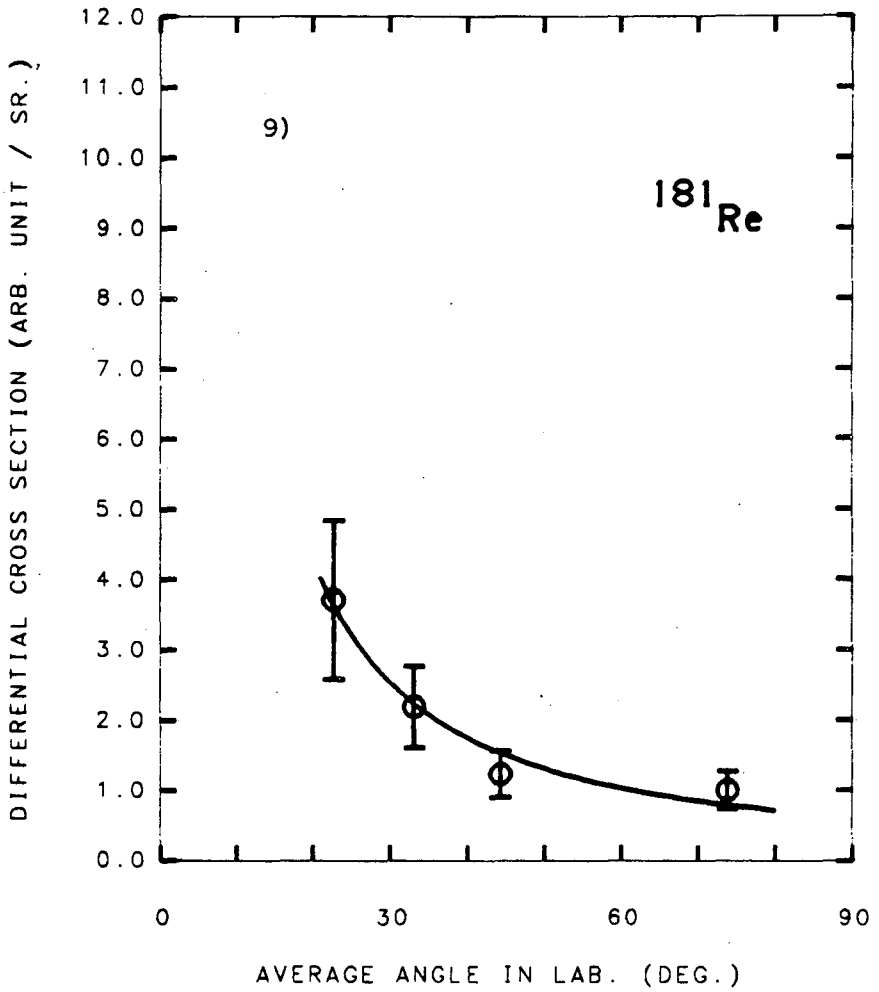

XBL 832-8151

Fig.6

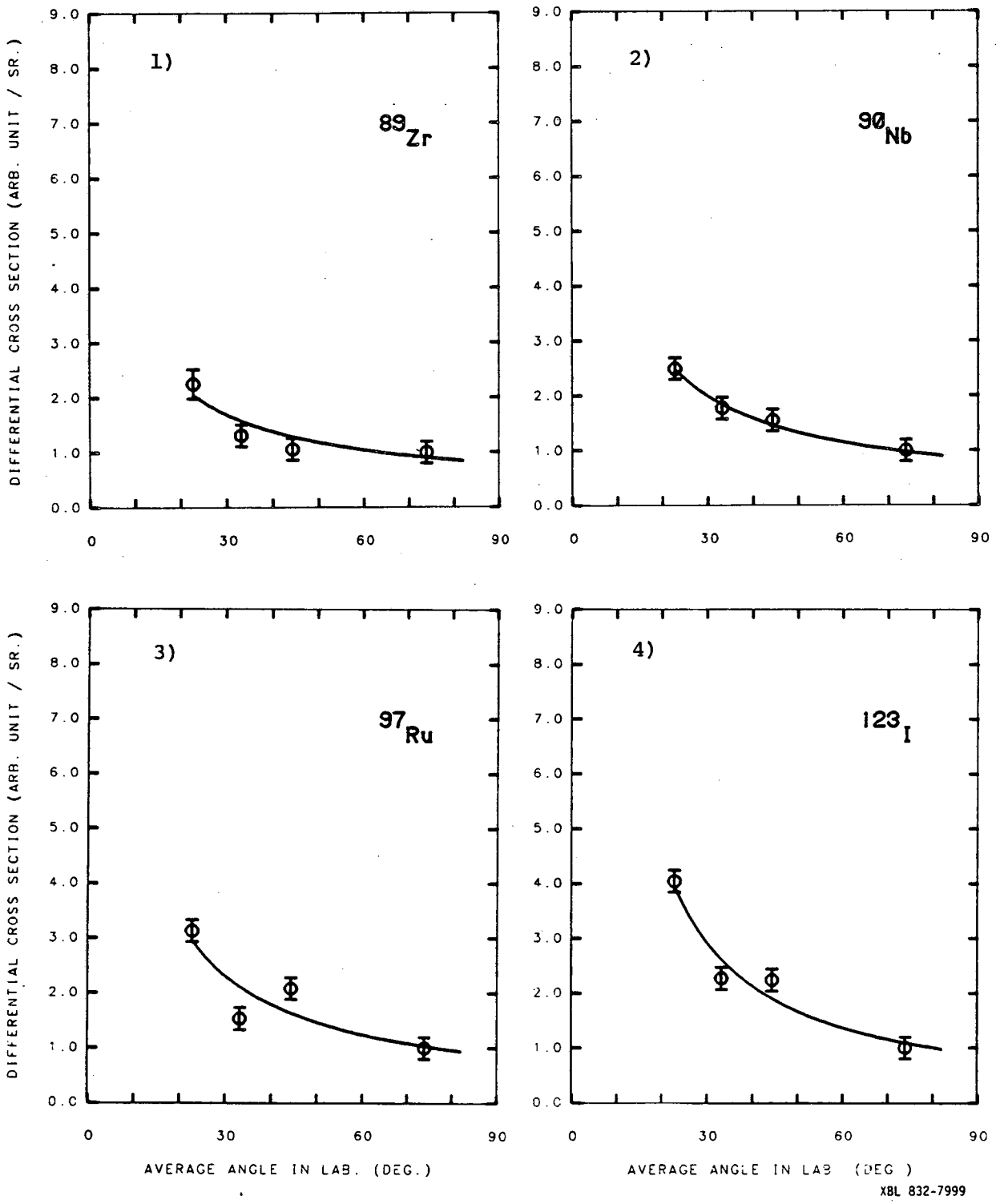
1)
^{89}Zr
2)
^{90}Nb
3)
^{97}Ru
4)
^{123}I
DIFFERENTIAL CROSS SECTION (ARB. UNIT / SR.)
AVERAGE ANGLE IN LAB. (DEG.)
AVERAGE ANGLE IN LAB (DEG.)
XBL 832-7999

Fig.7

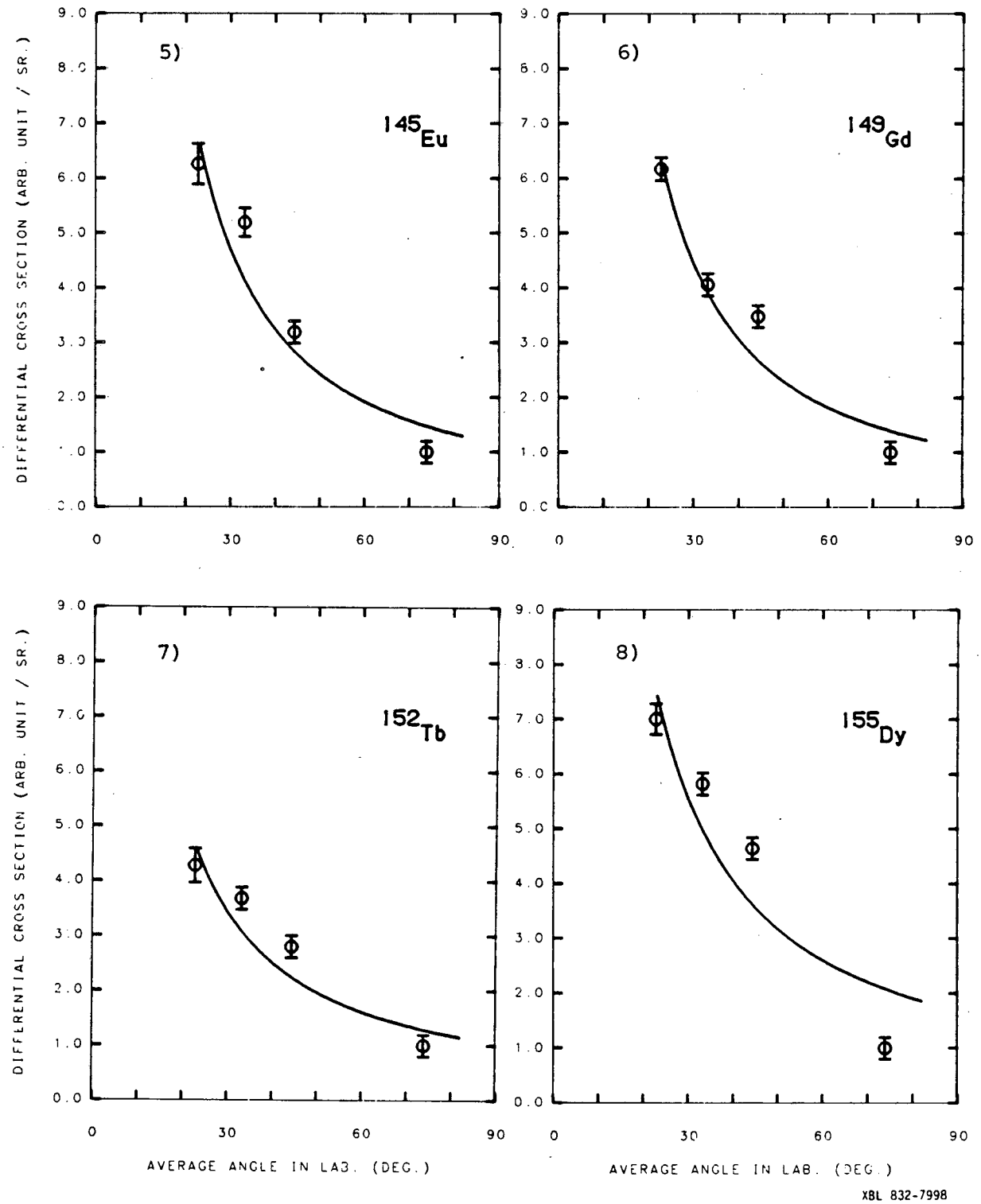
5)
^{145}Eu
6)
^{149}Gd
7)
^{152}Tb
8)
^{155}Dy
DIFFERENTIAL CROSS SECTION (ARB. UNIT / SR.)
AVERAGE ANGLE IN LAB. (DEG.)
XBL 832-7998

Fig.7

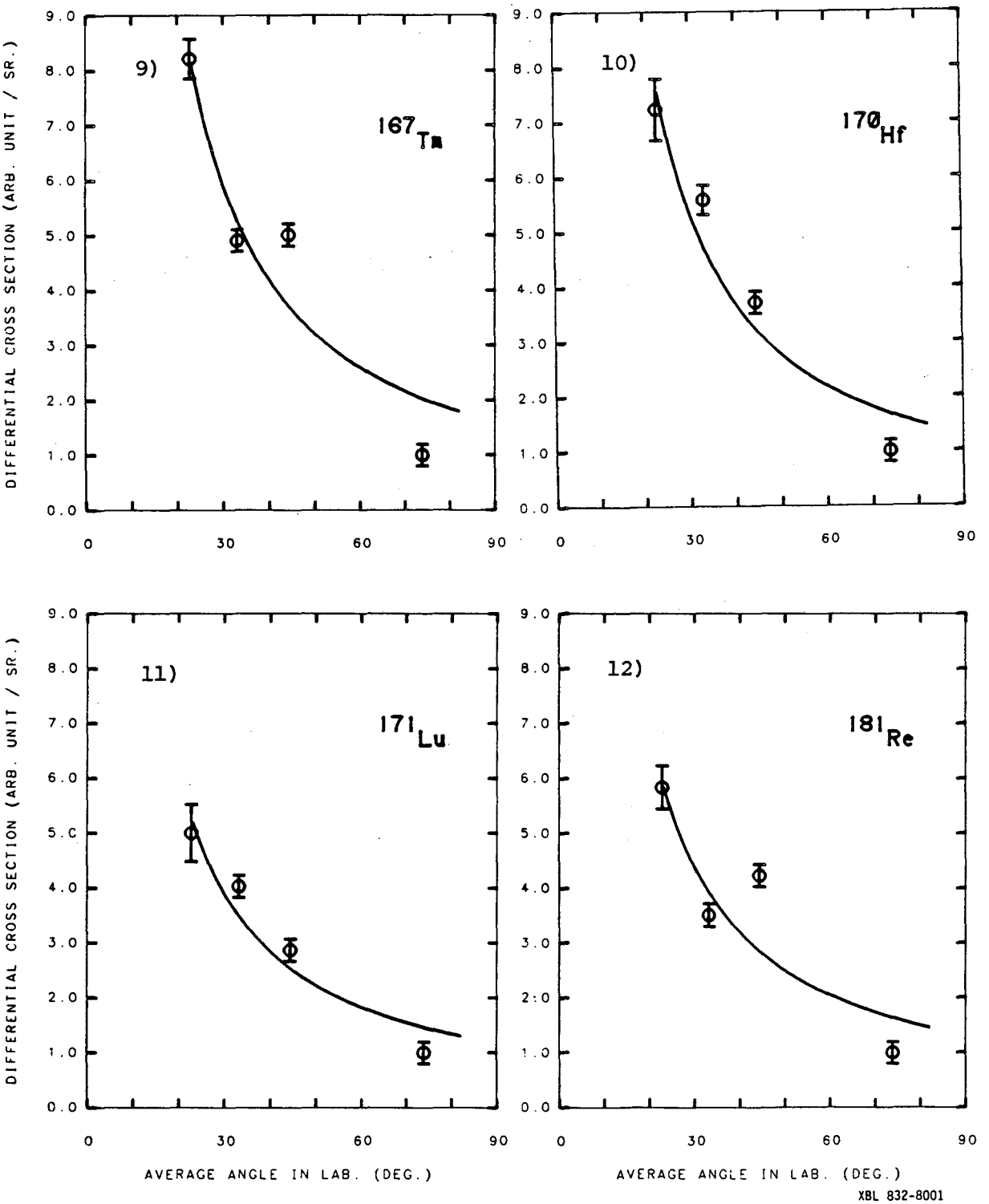
9)
^{167}Tm
10)
^{170}Hf
11)
^{171}Lu
12)
^{181}Re
DIFFERENTIAL CROSS SECTION (ARB. UNIT / SR.)
AVERAGE ANGLE IN LAB. (DEG.)
0.0
1.0
2.0
3.0
4.0
5.0
6.0
7.0
8.0
9.0
0
30
60
90
XBL 832-8001

Fig.7

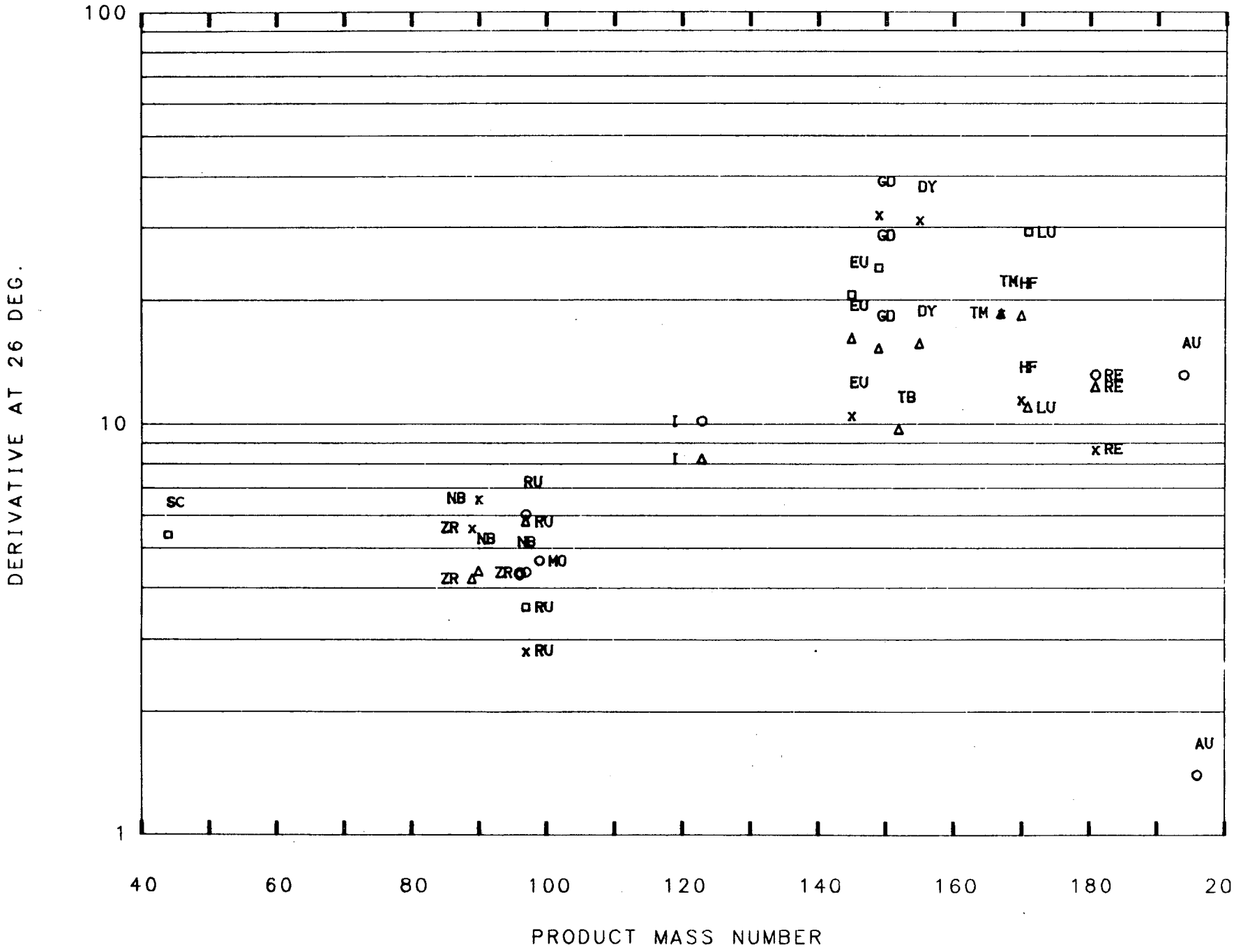

XBL 832-8157

Fig.8

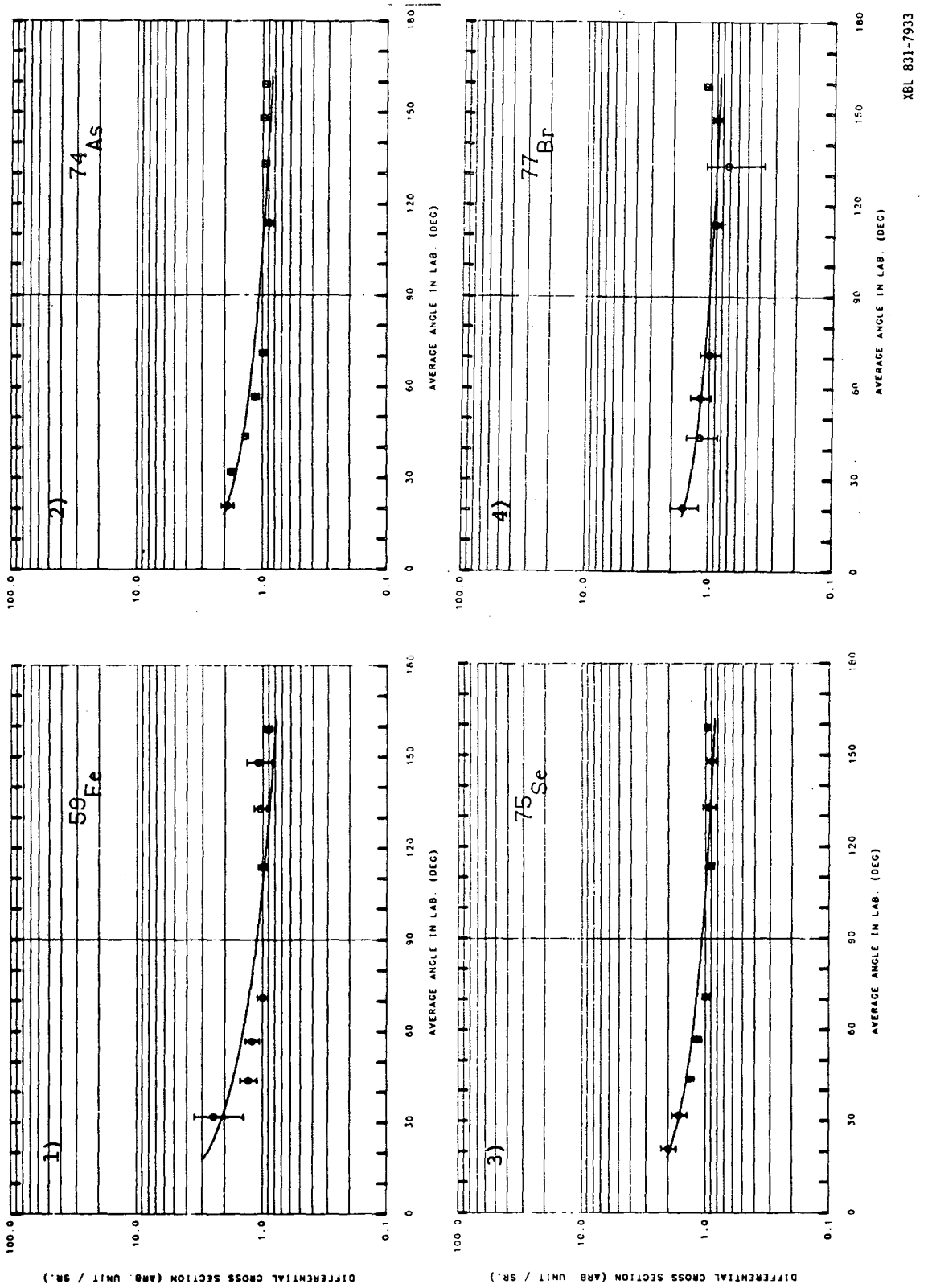
1) 59Fe
2) 74As
3) 75Se
4) 77Br
DIFFERENTIAL CROSS SECTION (ARB. UNIT / SR.)
AVERAGE ANGLE IN LAB. (DEG)
XBL 831-7933

Fig.9

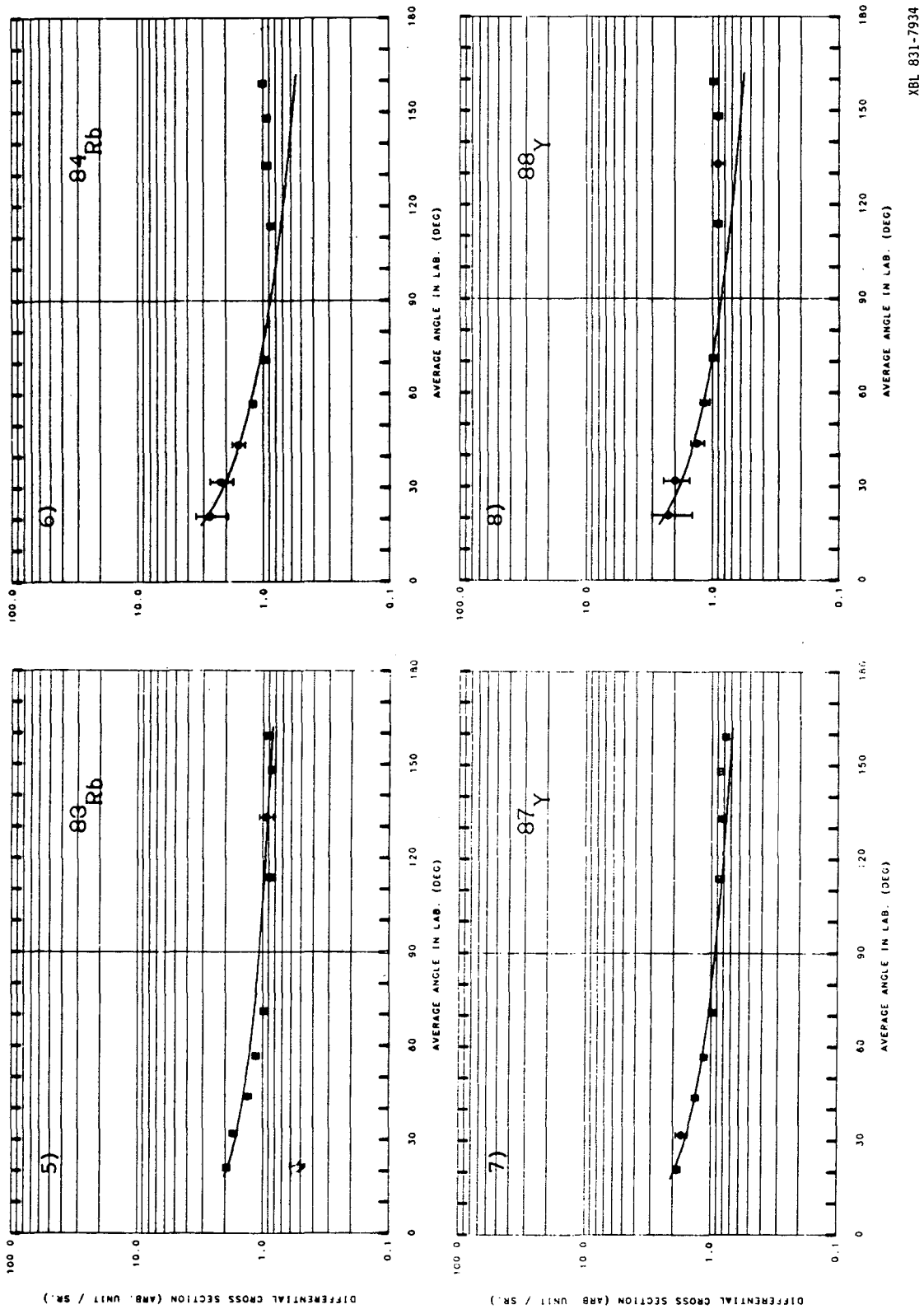

XBL 831-7934

Fig.9

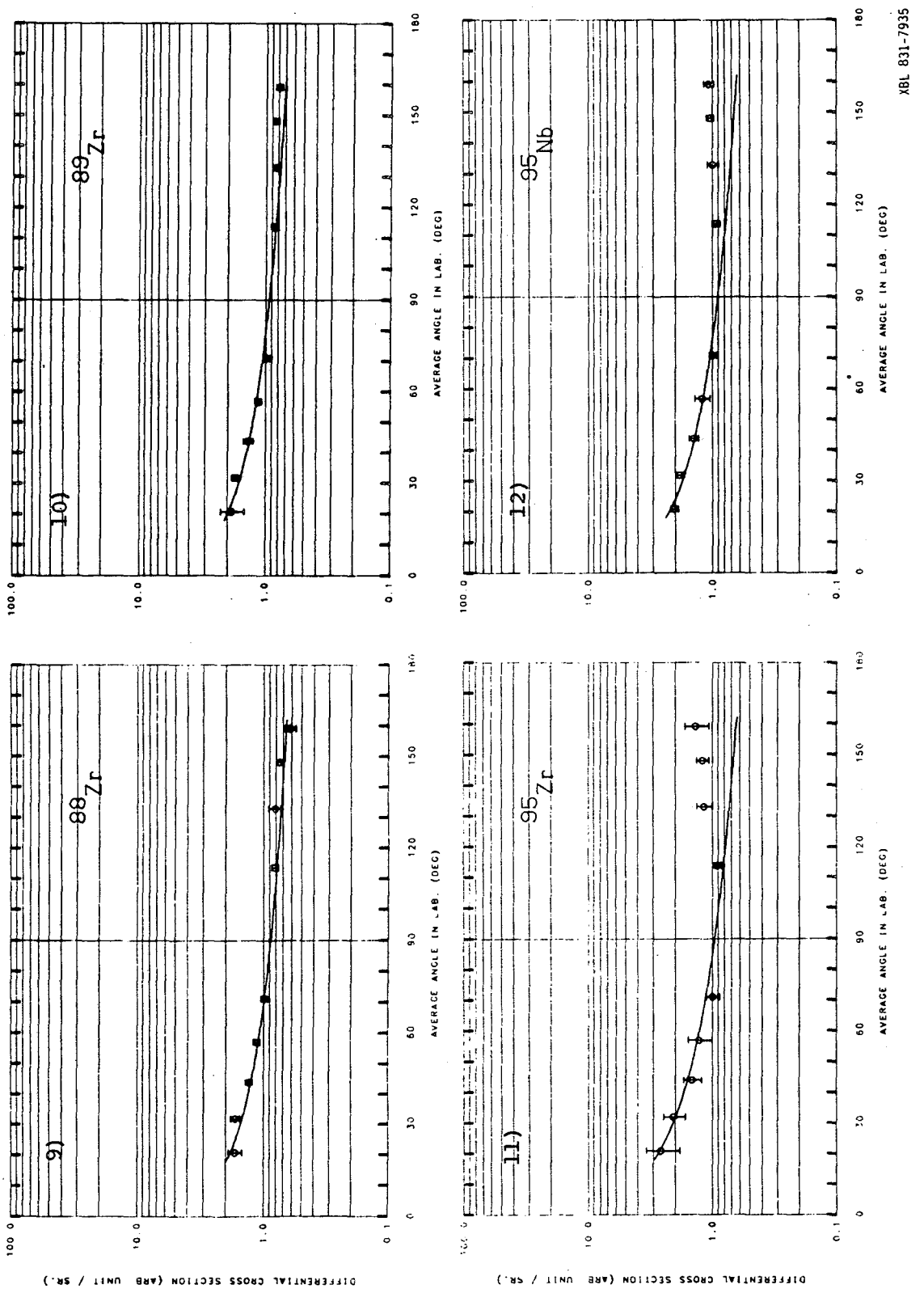
9) ^{88}Zr
10) ^{89}Zr
11) ^{95}Zr
12) ^{95}Nb
DIFFERENTIAL CROSS SECTION (ARB UNIT / SR.)
AVERAGE ANGLE IN LAB. (DEG)
XBL 831-7935

Fig.9

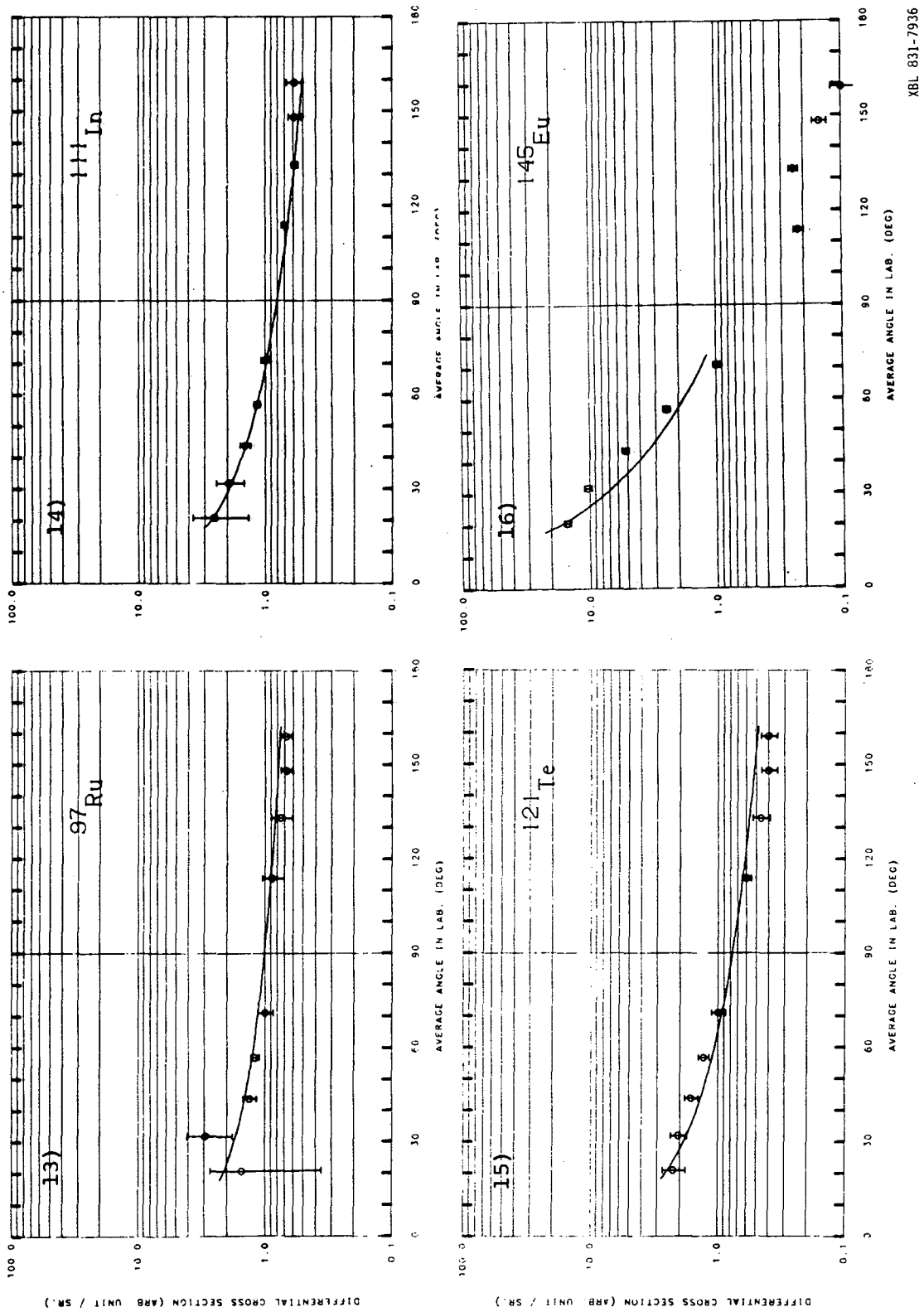
13) 97Ru
14) 111In
15) 121Te
16) 145Eu
DIFFERENTIAL CROSS SECTION (ARB. UNIT / SR.)
AVERAGE ANGLE IN LAB. (DEG)
XBL 831-7936

Fig.9

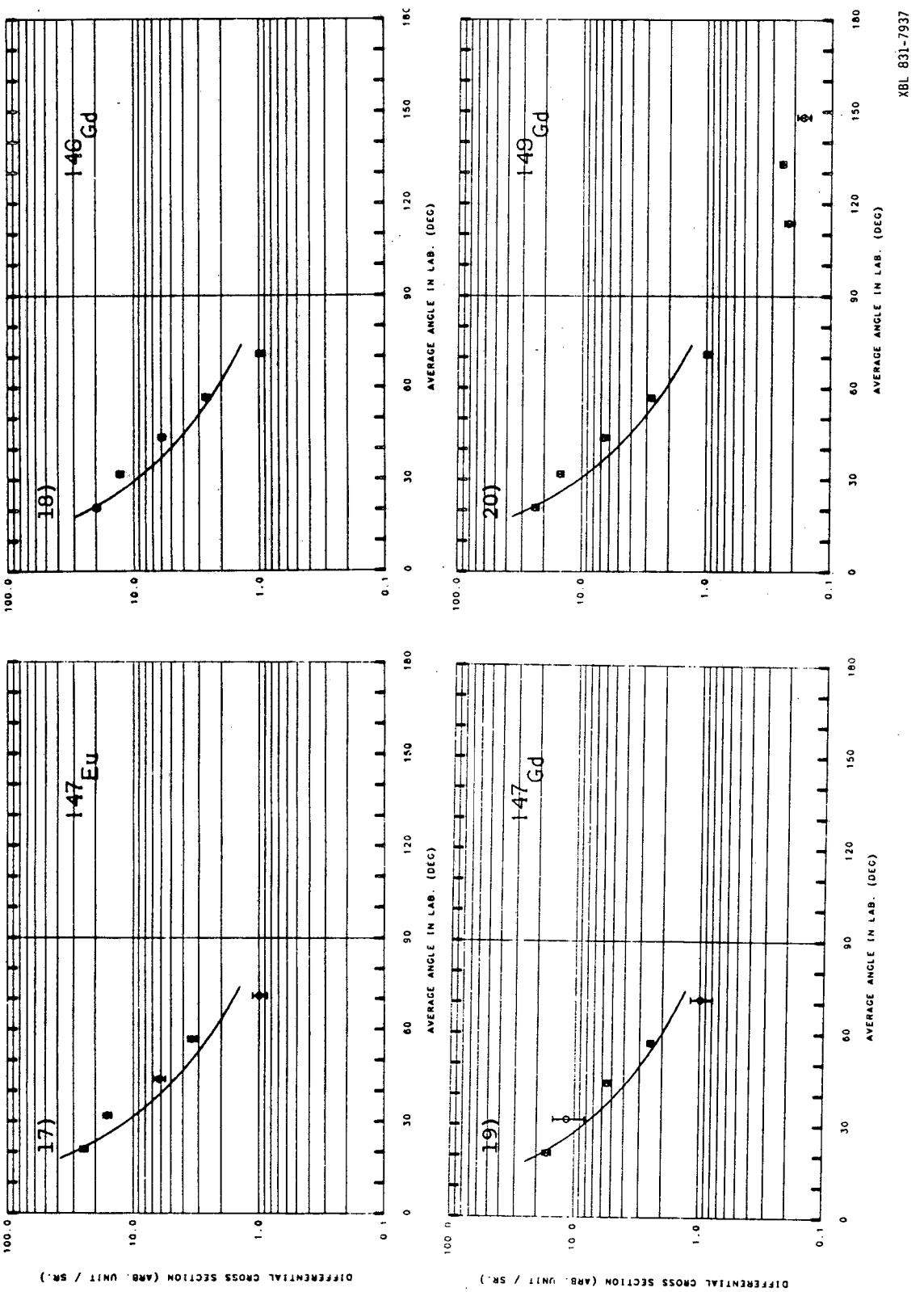
17) 147Eu
18) 146Gd
19) 147Gd
20) 149Gd
DIFFERENTIAL CROSS SECTION (ARB. UNIT / SR.)
AVERAGE ANGLE IN LAB. (DEG)
XBL 831-7937

Fig.9

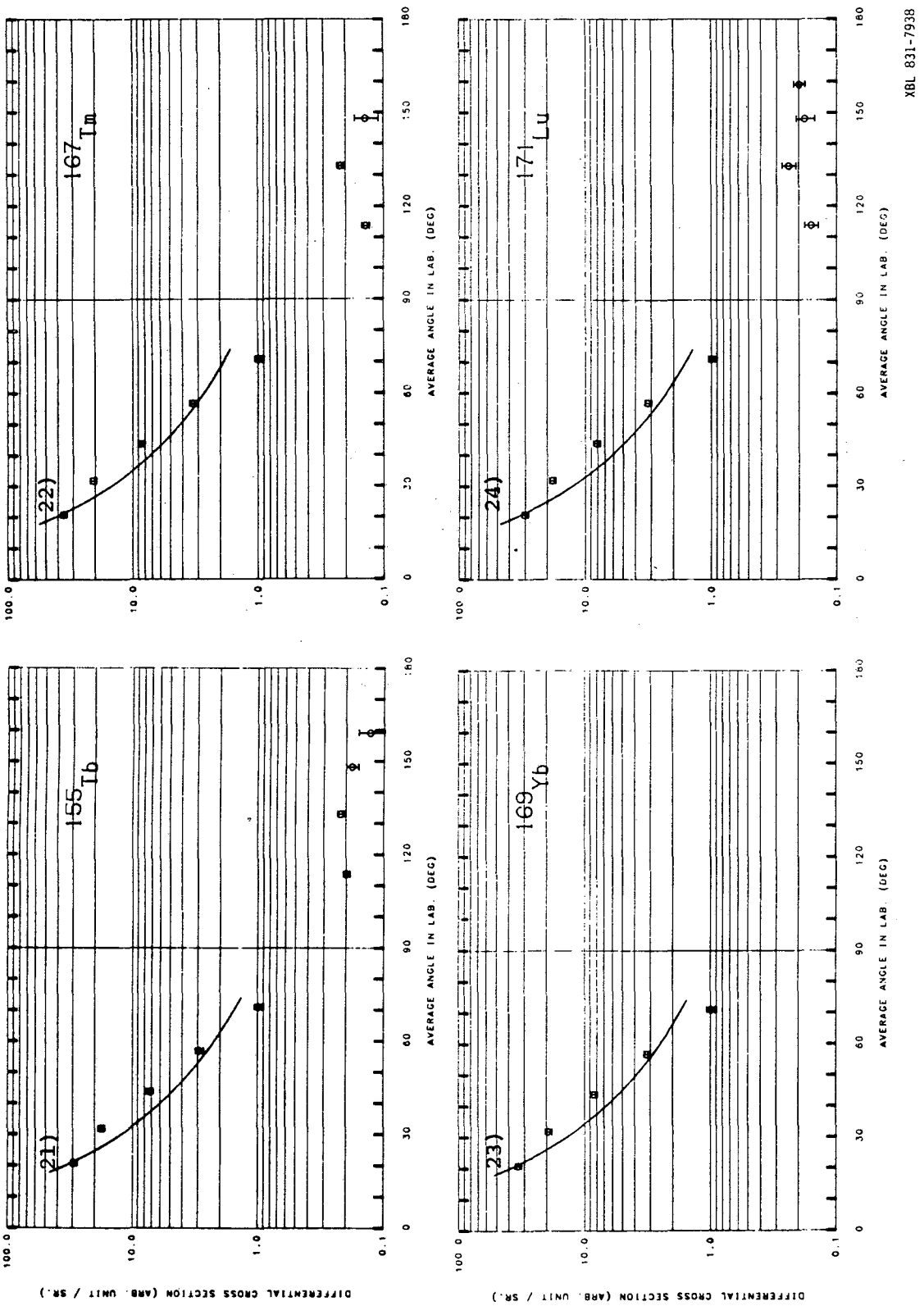
155Tb
167Tm
169Yb
171Lu
21)
22)
23)
24)
DIFFERENTIAL CROSS SECTION (ARB. UNIT / SR.)
AVERAGE ANGLE IN LAB. (DEG)
XBL 831-7938

Fig.9

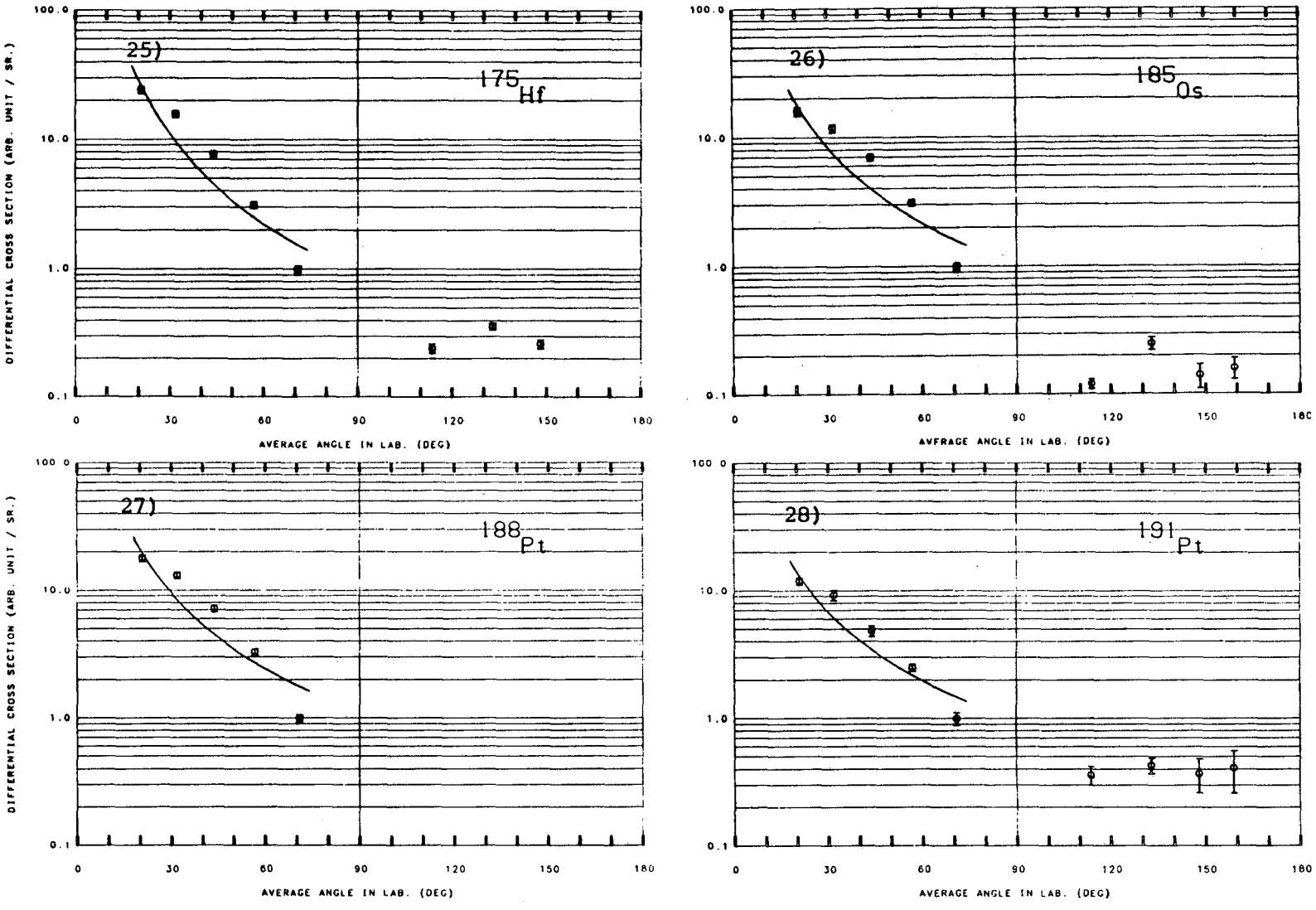

XBL 831-7939

Fig.9

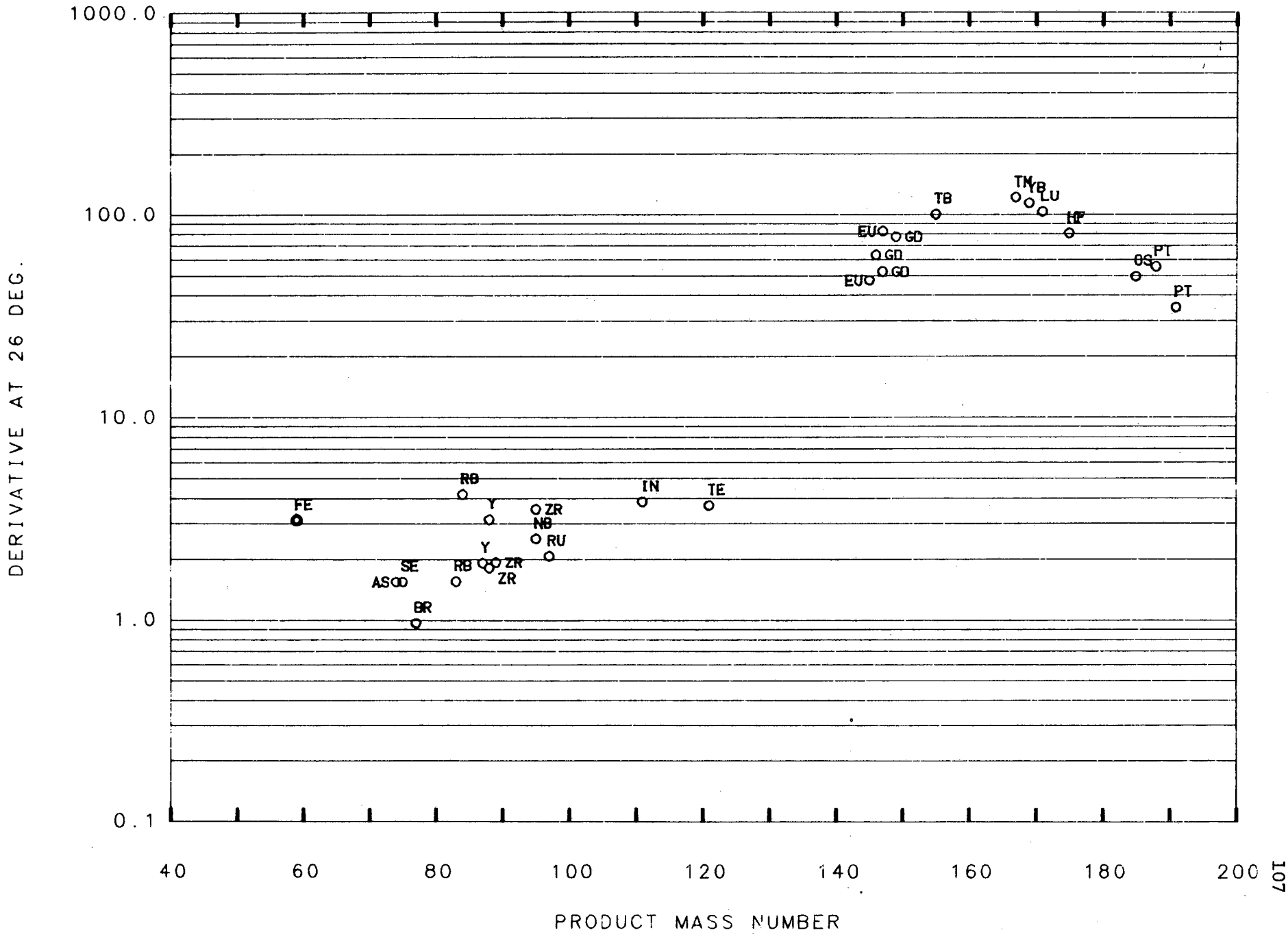

XBL 832-8159

Fig.10

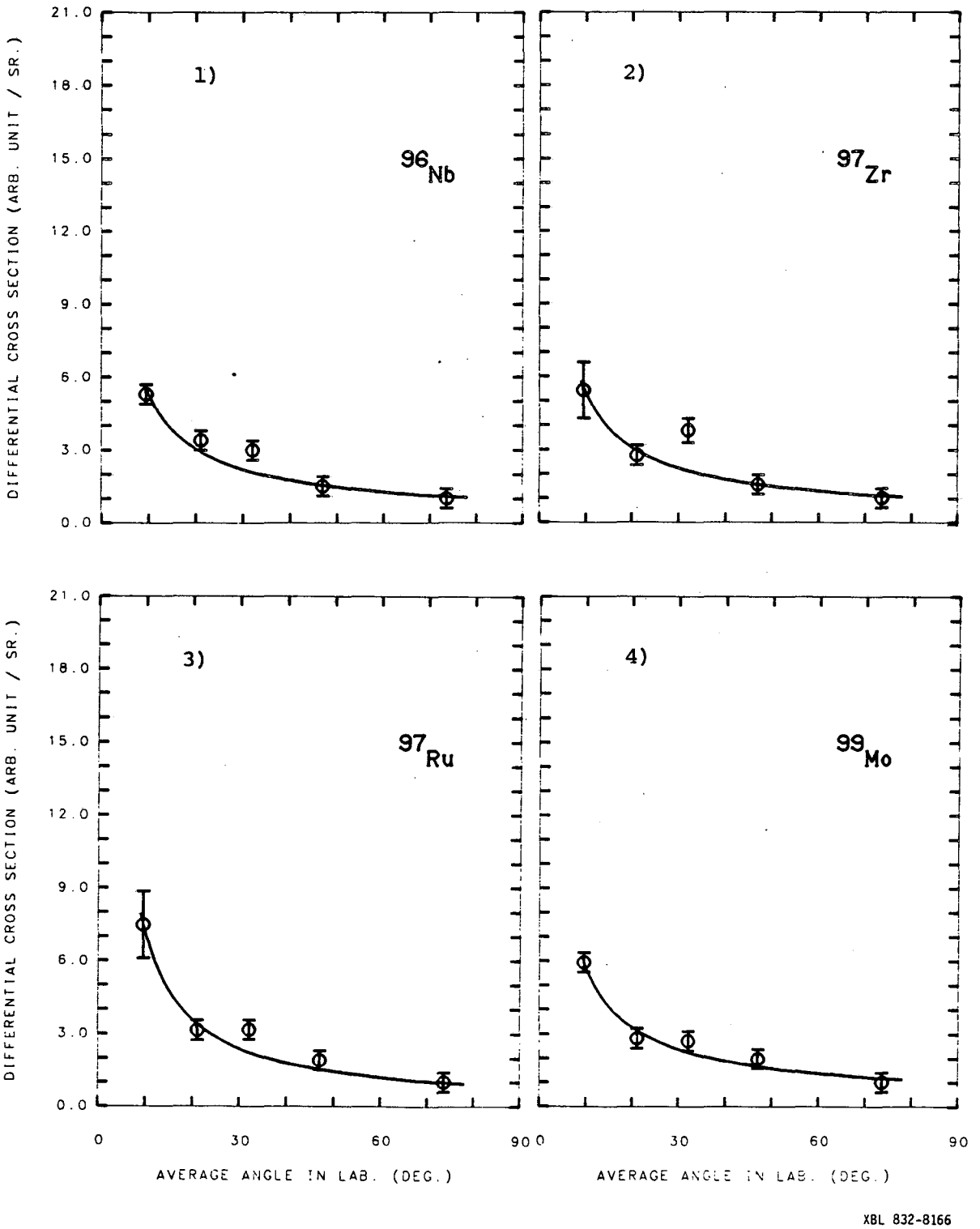
1)
^{96}Nb
2)
^{97}Zr
3)
^{97}Ru
4)
^{99}Mo
DIFFERENTIAL CROSS SECTION (ARB. UNIT / SR.)
AVERAGE ANGLE IN LAB. (DEG.)
0.0
3.0
6.0
9.0
12.0
15.0
18.0
21.0
0
30
60
90
XBL 832-8166

Fig.11

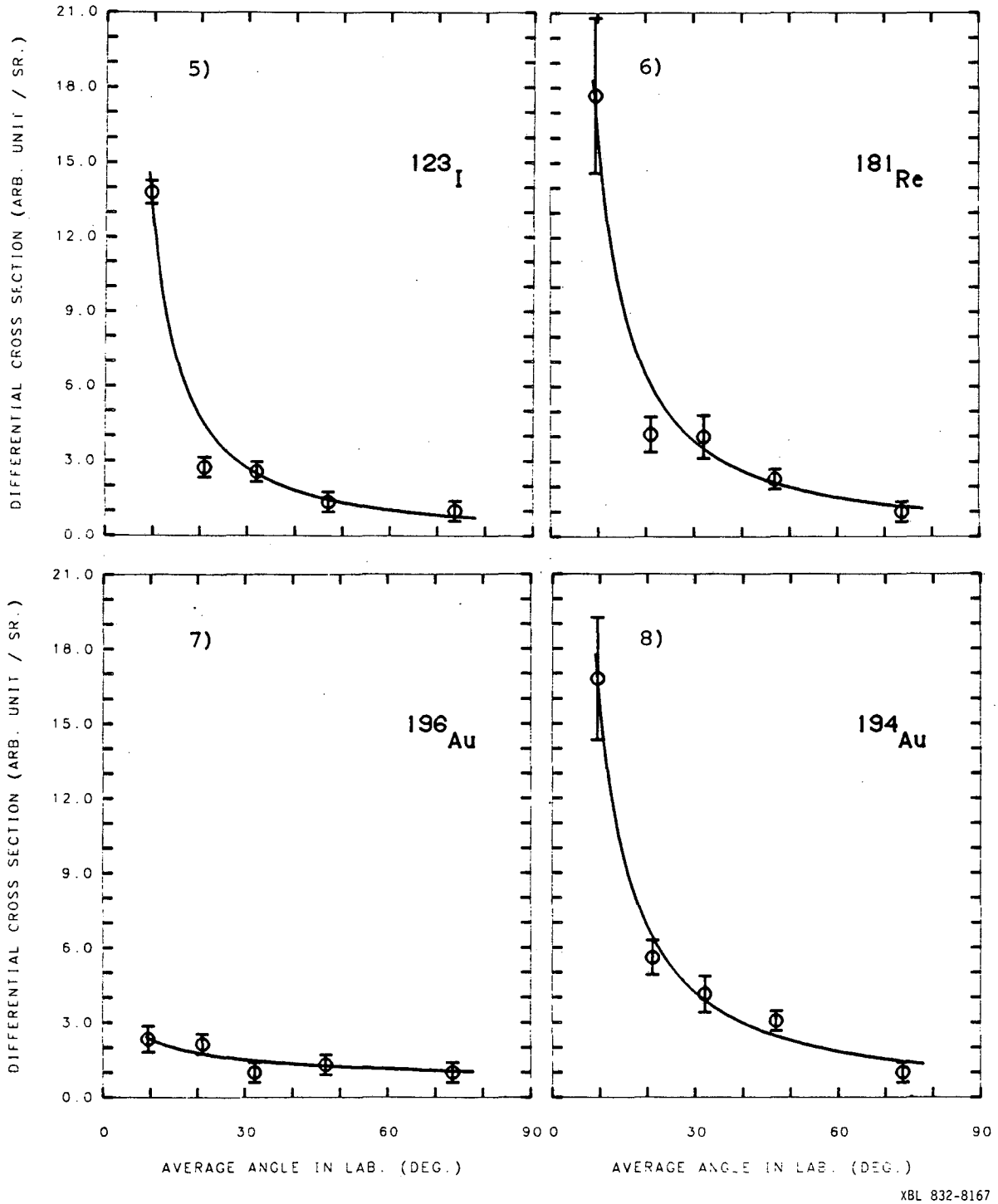
5)
123I
6)
181Re
7)
196Au
8)
194Au
DIFFERENTIAL CROSS SECTION (ARB. UNIT / SR.)
DIFFERENTIAL CROSS SECTION (ARB. UNIT / SR.)
21.0
18.0
15.0
12.0
9.0
6.0
3.0
0.0
0
30
60
90
AVERAGE ANGLE IN LAB. (DEG.)
AVERAGE ANGLE IN LAB. (DEG.)
XBL 832-8167

Fig.11

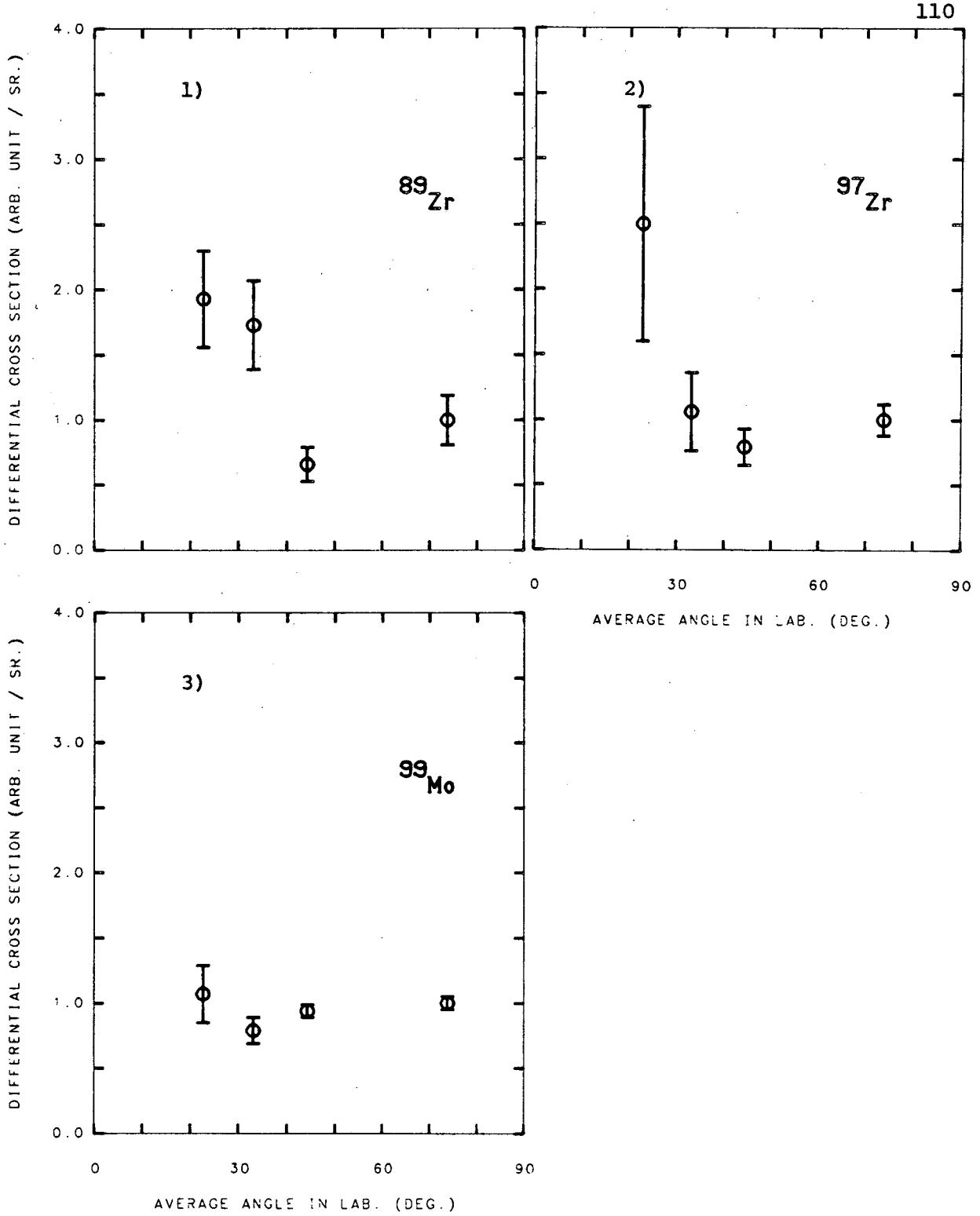
1)
89Zr
2)
97Zr
3)
99Mo
DIFFERENTIAL CROSS SECTION (ARB. UNIT / SR.)
AVERAGE ANGLE IN LAB. (DEG.)
0.0
1.0
2.0
3.0
4.0
0
30
60
90

XBL 834-9039

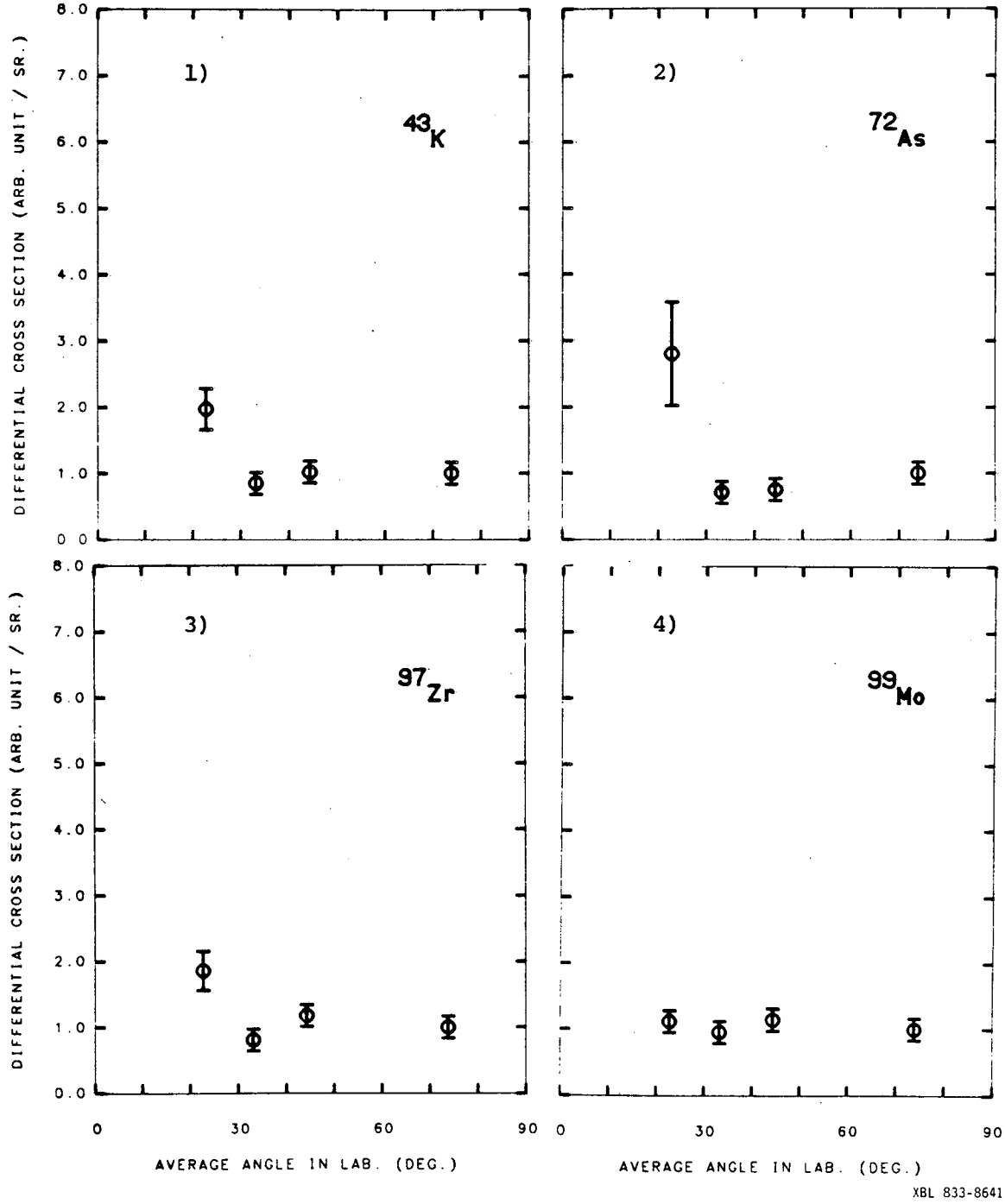
1)
^{43}K
2)
^{72}As
3)
^{97}Zr
4)
^{99}Mo
DIFFERENTIAL CROSS SECTION (ARB. UNIT / SR.)
DIFFERENTIAL CROSS SECTION (ARB. UNIT / SR.)
0.0
1.0
2.0
3.0
4.0
5.0
6.0
7.0
8.0
0
30
60
90
AVERAGE ANGLE IN LAB. (DEG.)
AVERAGE ANGLE IN LAB. (DEG.)
XBL 833-8641

Fig.13

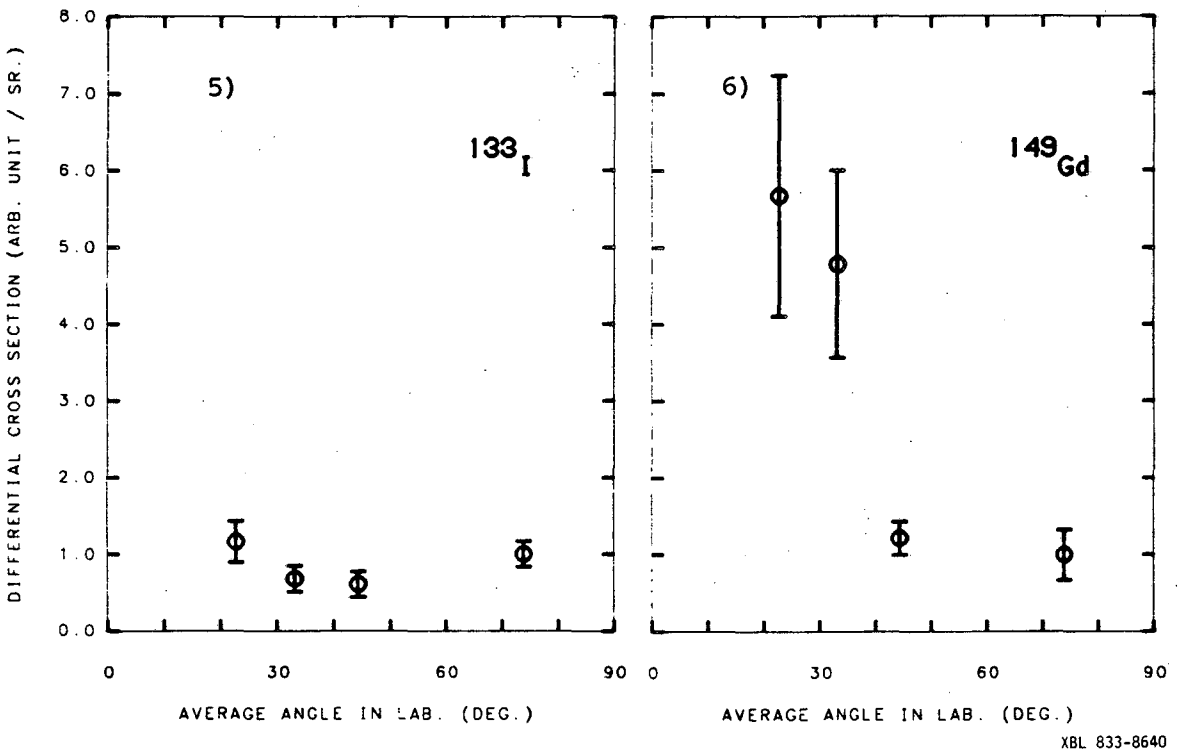
DIFFERENTIAL CROSS SECTION (ARB. UNIT / SR.)
8.0
7.0
6.0
5.0
4.0
3.0
2.0
1.0
0.0
5)
133I
6)
149Gd
0
30
60
90
AVERAGE ANGLE IN LAB. (DEG.)
AVERAGE ANGLE IN LAB. (DEG.)
XBL 833-8640

Fig.13

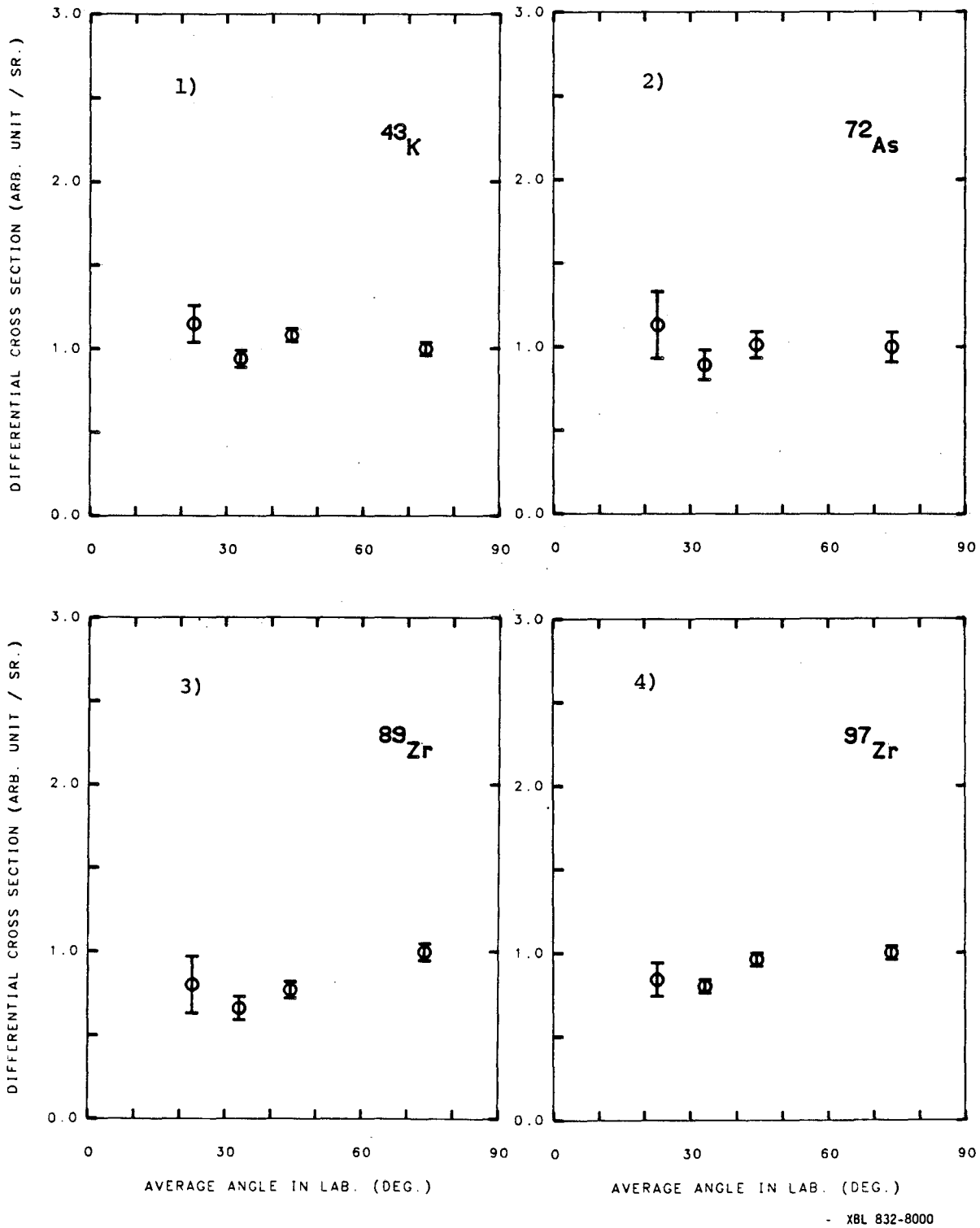
1)
^{43}K
2)
^{72}As
3)
^{89}Zr
4)
^{97}Zr
DIFFERENTIAL CROSS SECTION (ARB. UNIT / SR.)
AVERAGE ANGLE IN LAB. (DEG.)
0.0
1.0
2.0
3.0
0
30
60
90
XBL 832-8000

Fig.14

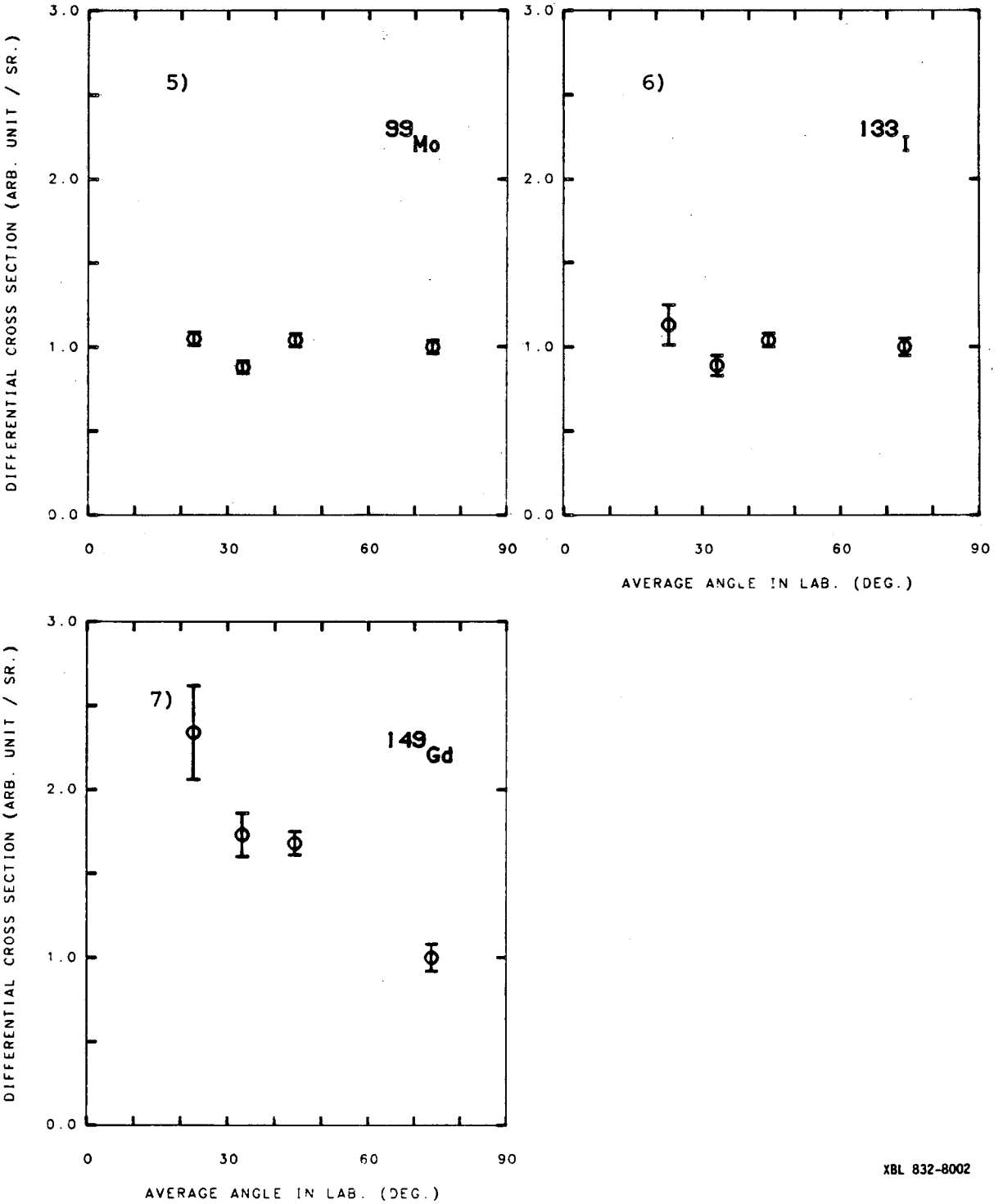
5)
^{99}Mo
6)
^{133}I
7)
^{149}Gd
DIFFERENTIAL CROSS SECTION (ARB. UNIT / SR.)
AVERAGE ANGLE IN LAB. (DEG.)
0.0
1.0
2.0
3.0
0
30
60
90
XBL 832-8002

Fig.14

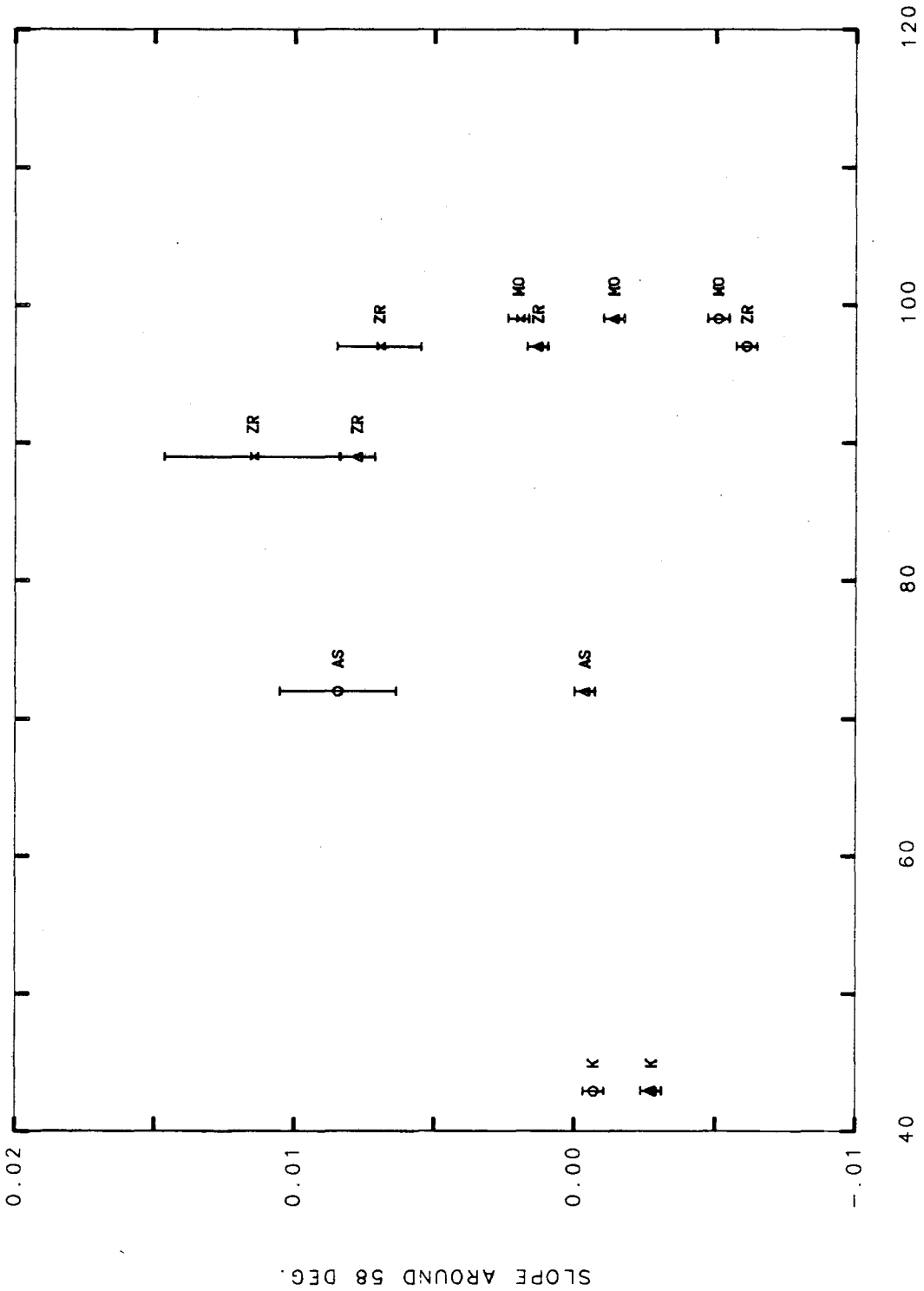
SLOPE AROUND 58 DEG.
0.02
0.01
0.00
-.01
40
60
80
100
120
PRODUCT MASS NUMBER
ZR
ZR
ZR
ZR
MO
MO
MO
AS
AS
K
K

XBL 834-9038

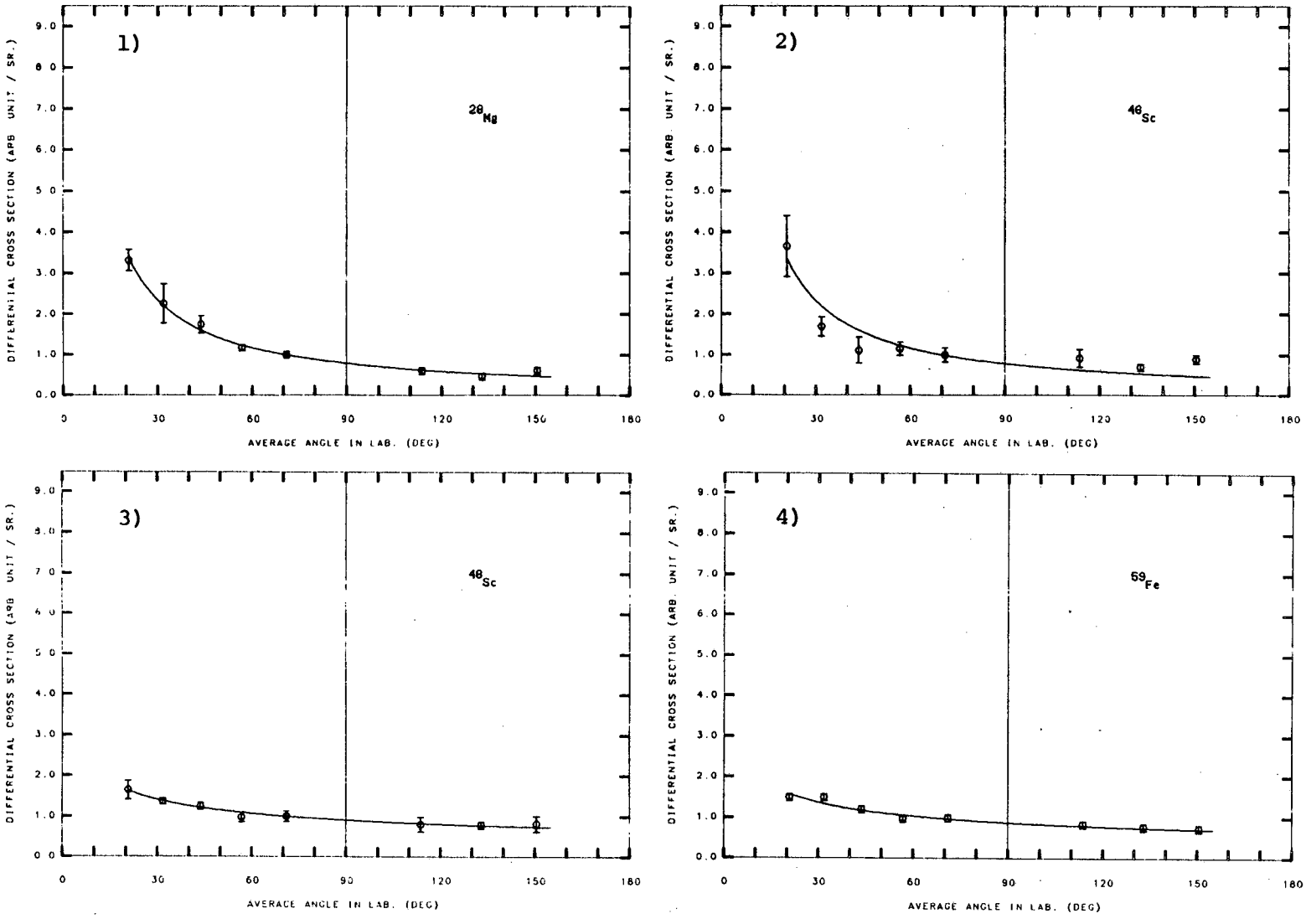
1)
^{28}Mg
2)
^{46}Sc
3)
^{48}Sc
4)
^{59}Fe
DIFFERENTIAL CROSS SECTION (ARB. UNIT / SR.)
AVERAGE ANGLE IN LAB. (DEG)
0
30
60
90
120
150
180
XBL 831-7867

Fig.16

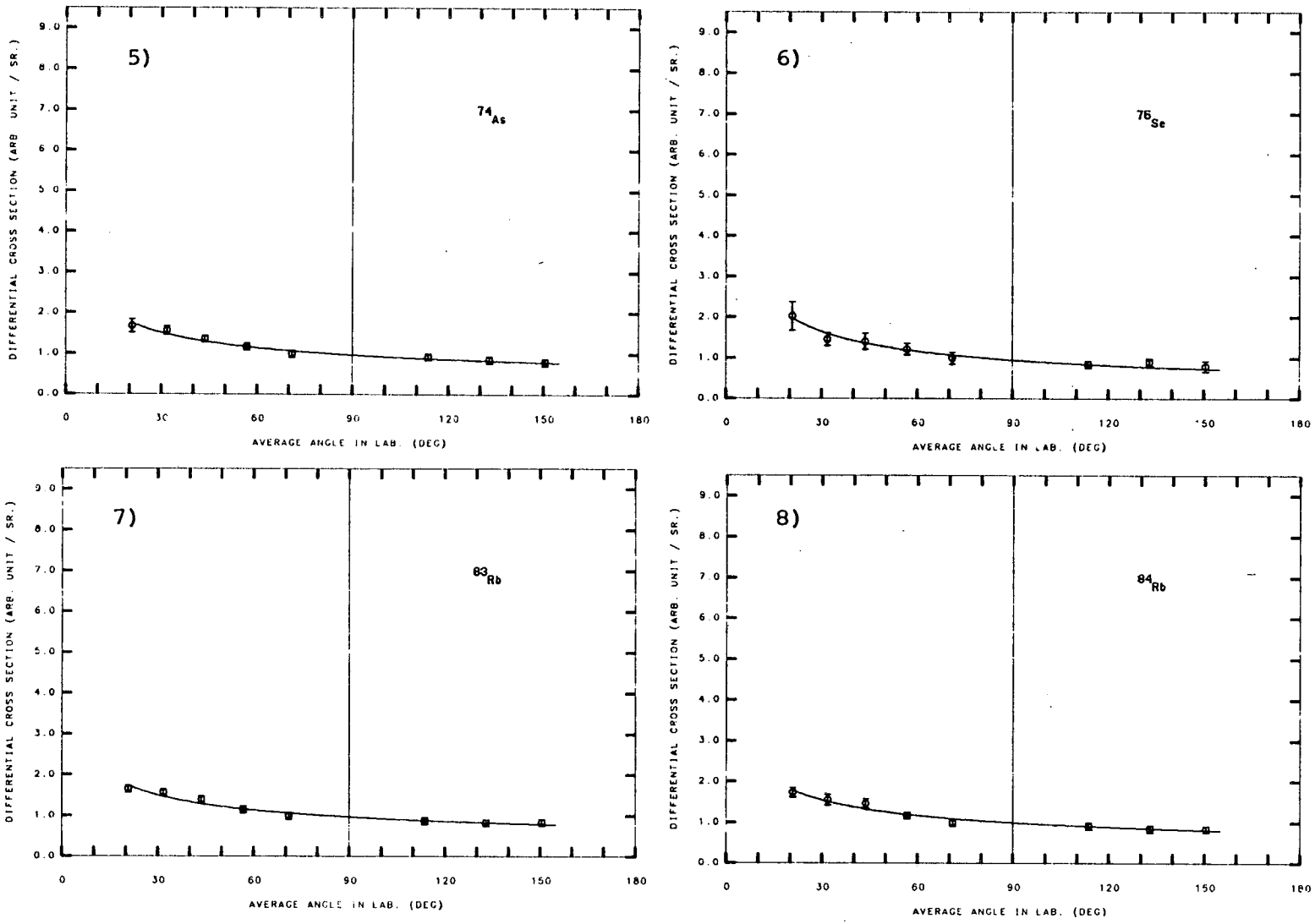

XBL 832-7866

Fig.16

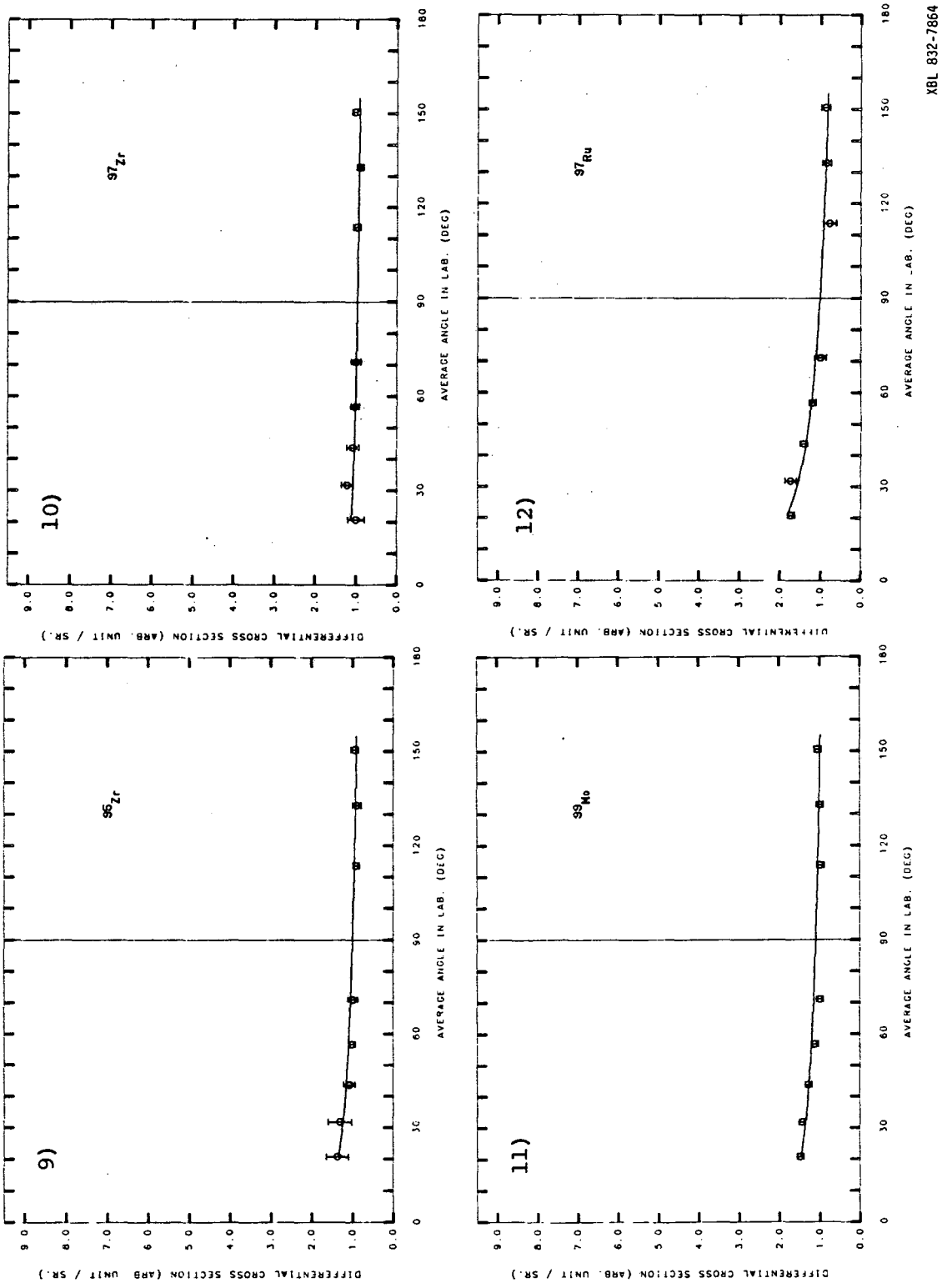
10)
^{97}Zr
12)
^{97}Ru
9)
^{95}Zr
11)
^{99}Mo
DIFFERENTIAL CROSS SECTION (ARB. UNIT / SR.)
AVERAGE ANGLE IN LAB. (DEG)
XBL 832-7864

Fig.16

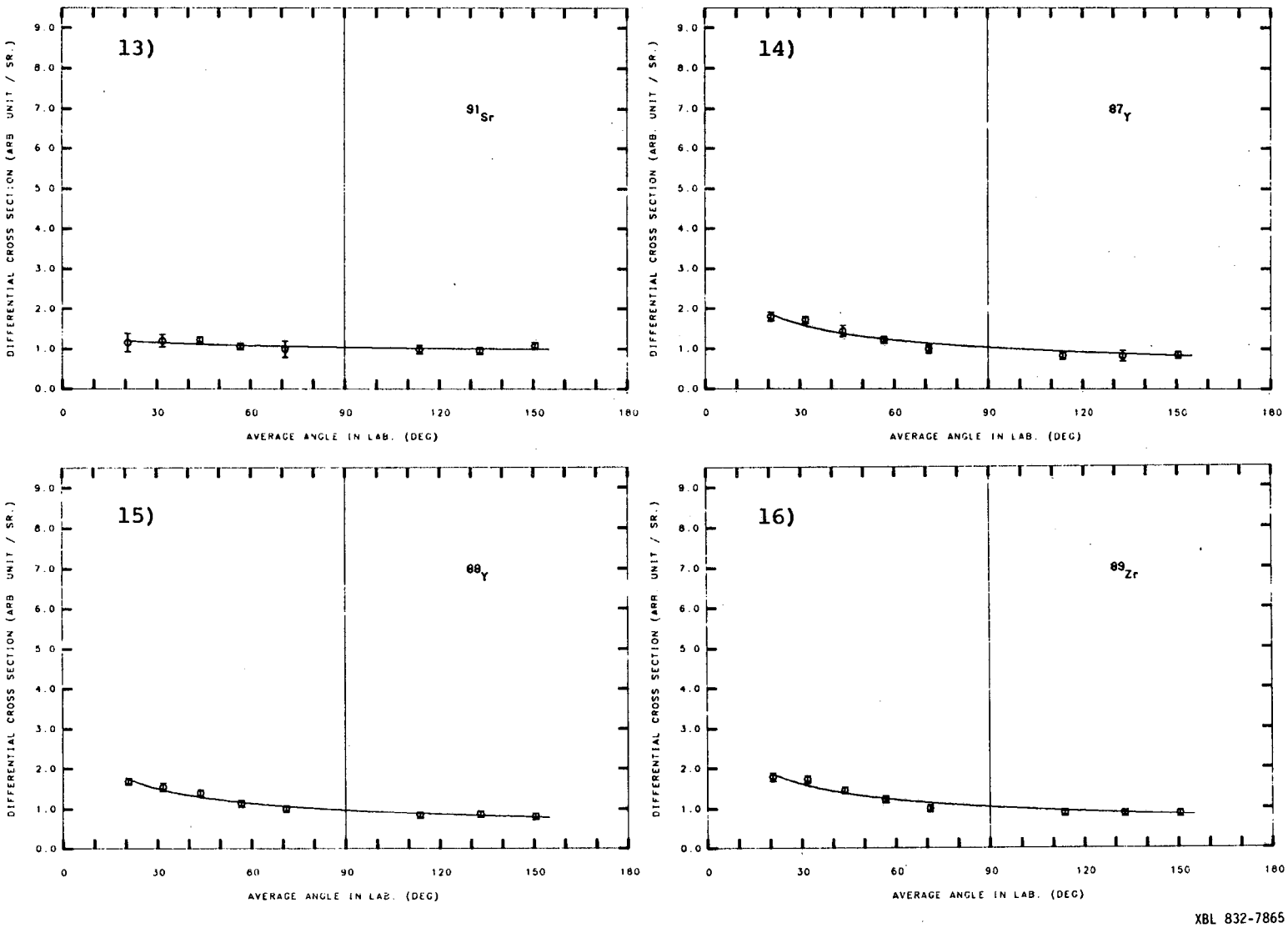

XBL 832-7865

Fig.16

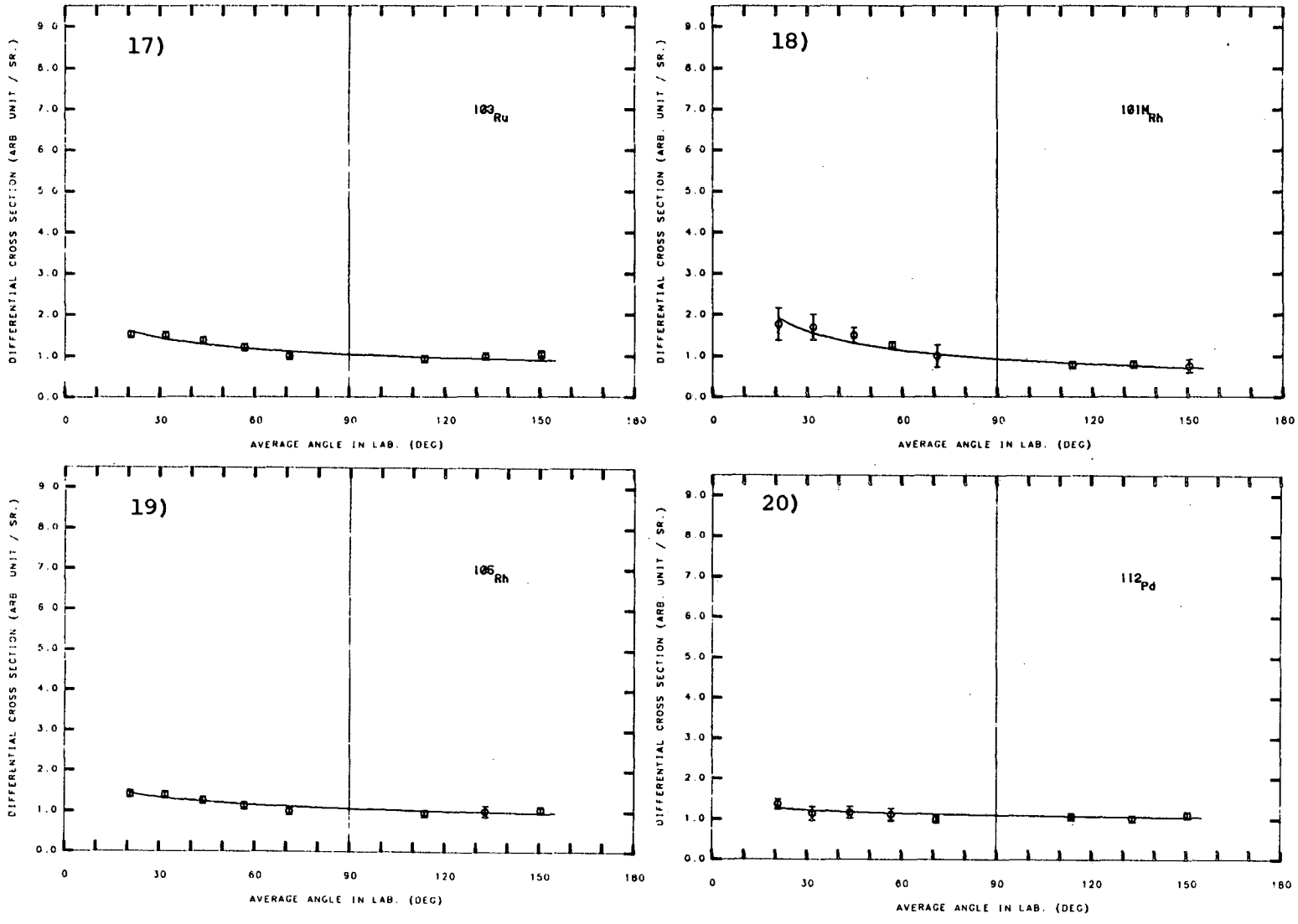
17)
^{103}Ru
18)
^{101M}Rh
19)
^{105}Rh
20)
^{112}Pd
DIFFERENTIAL CROSS SECTION (ARB. UNIT / SR.)
AVERAGE ANGLE IN LAB. (DEG)
XBL 832-7863

Fig.16

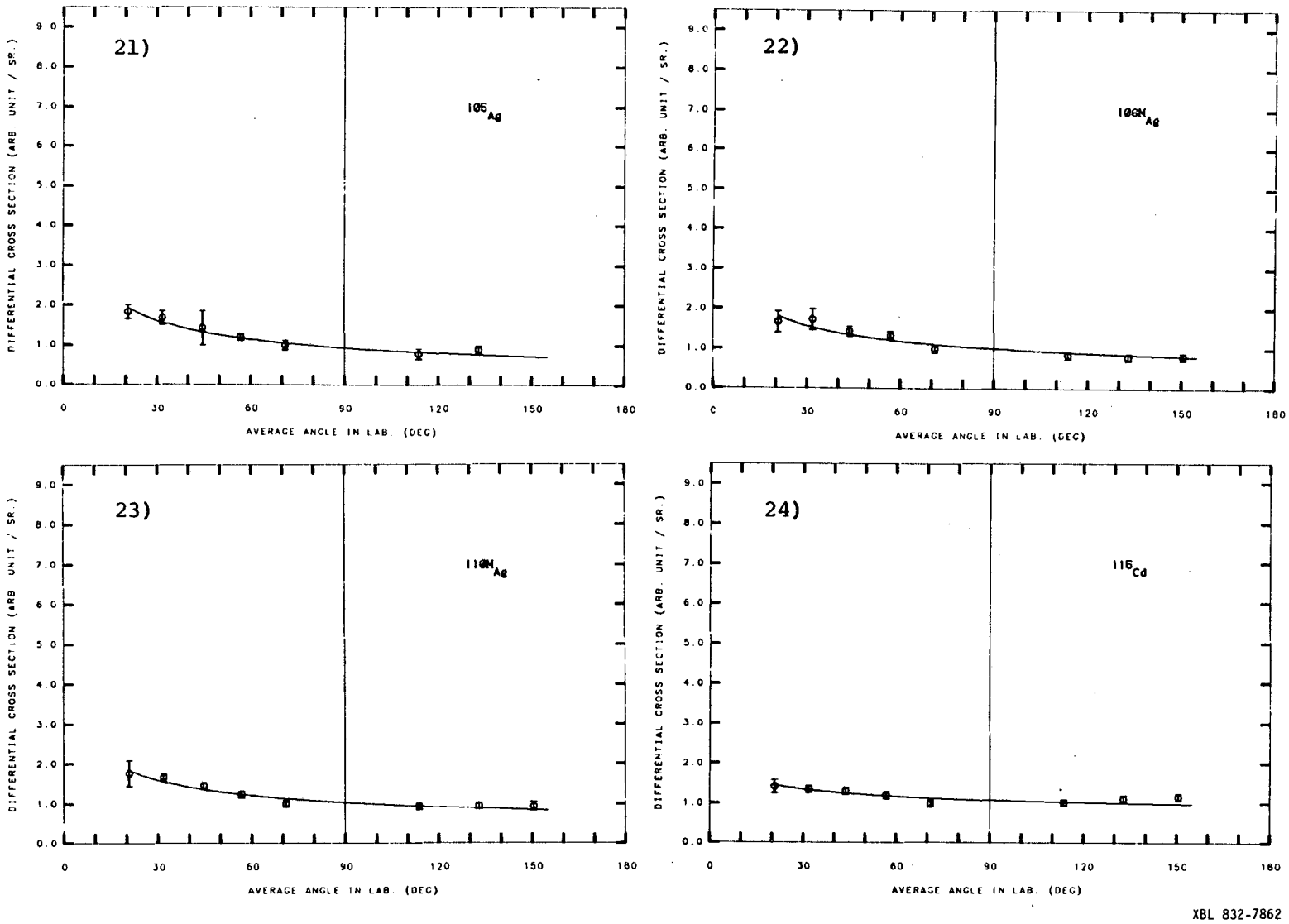
21)
^{105}Ag
22)
^{106M}Ag
23)
^{110M}Ag
24)
^{115}Cd
DIFFERENTIAL CROSS SECTION (ARB. UNIT / SR.)
AVERAGE ANGLE IN LAB. (DEG)
0
30
60
90
120
150
180
XBL 832-7862

Fig.16

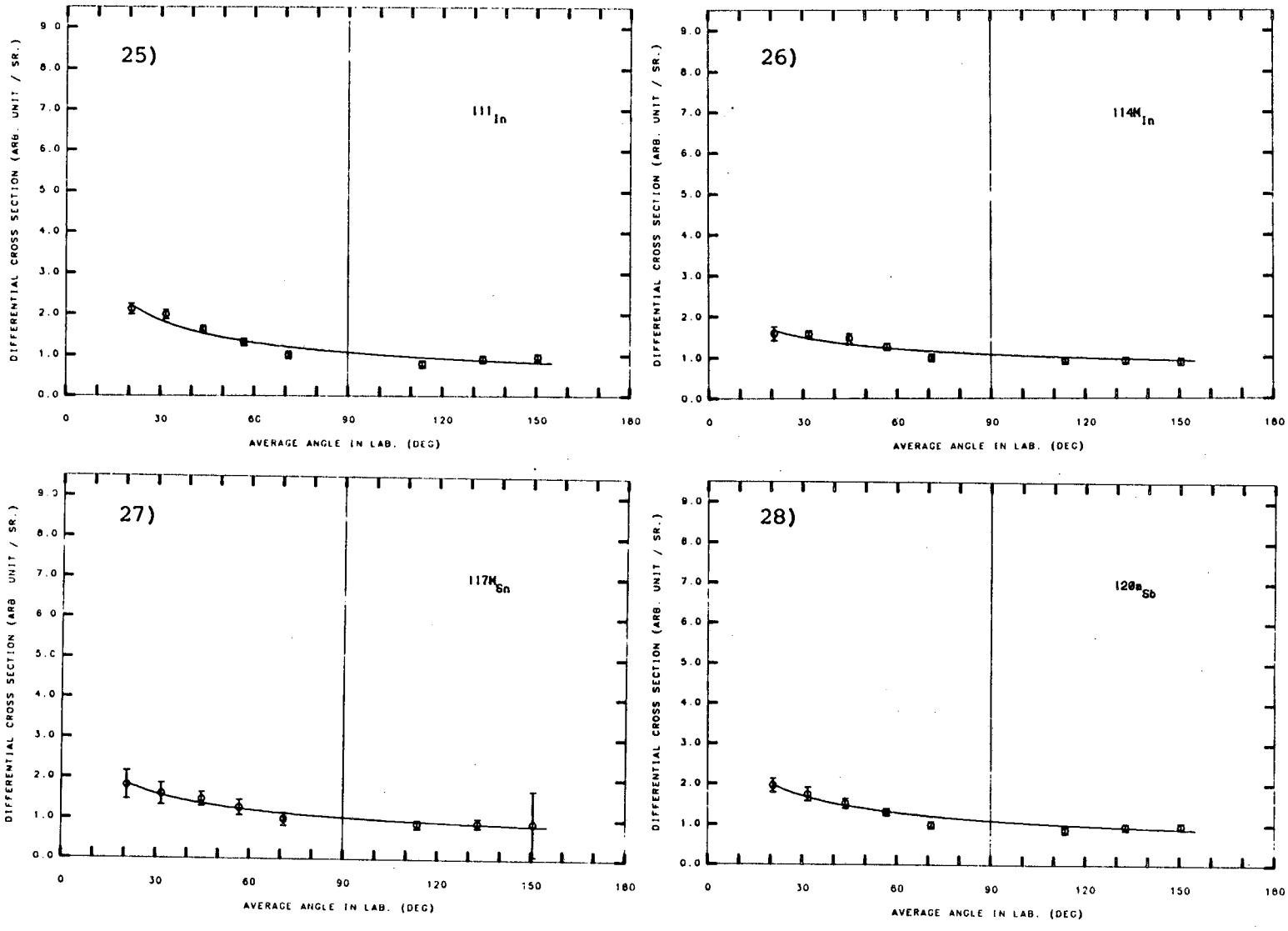

XBL 831-7869

Fig.16

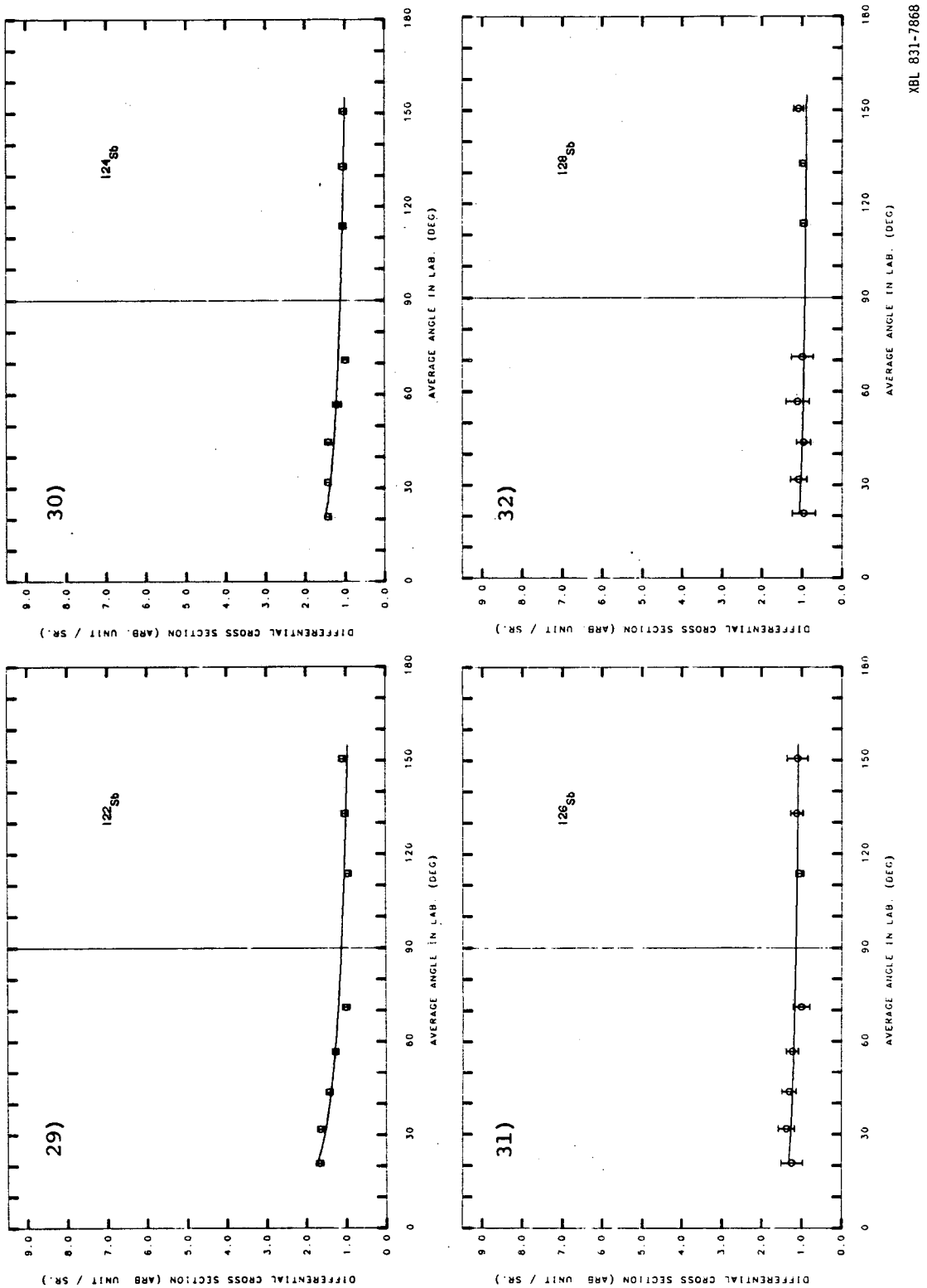
29)
^{122}Sb
30)
^{124}Sb
31)
^{126}Sb
32)
^{128}Sb
DIFFERENTIAL CROSS SECTION (ARB. UNIT / SR.)
AVERAGE ANGLE IN LAB. (DEG)
XBL 831-7868

Fig.16

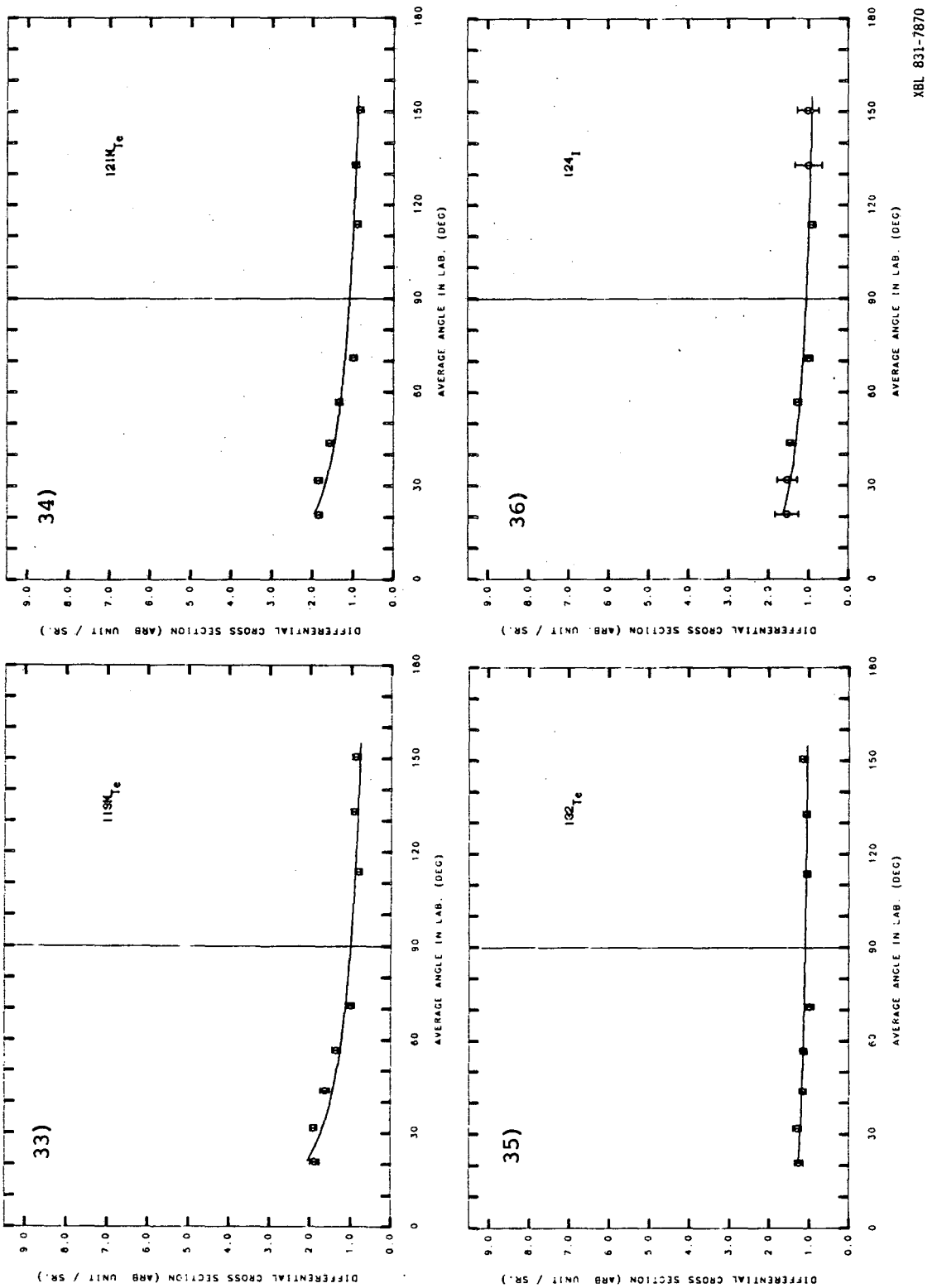
34)
121mTe
33)
119mTe
36)
124I
35)
122Te
DIFFERENTIAL CROSS SECTION (ARB. UNIT / SR.)
AVERAGE ANGLE IN LAB. (DEG)
XBL 831-7870

Fig.16

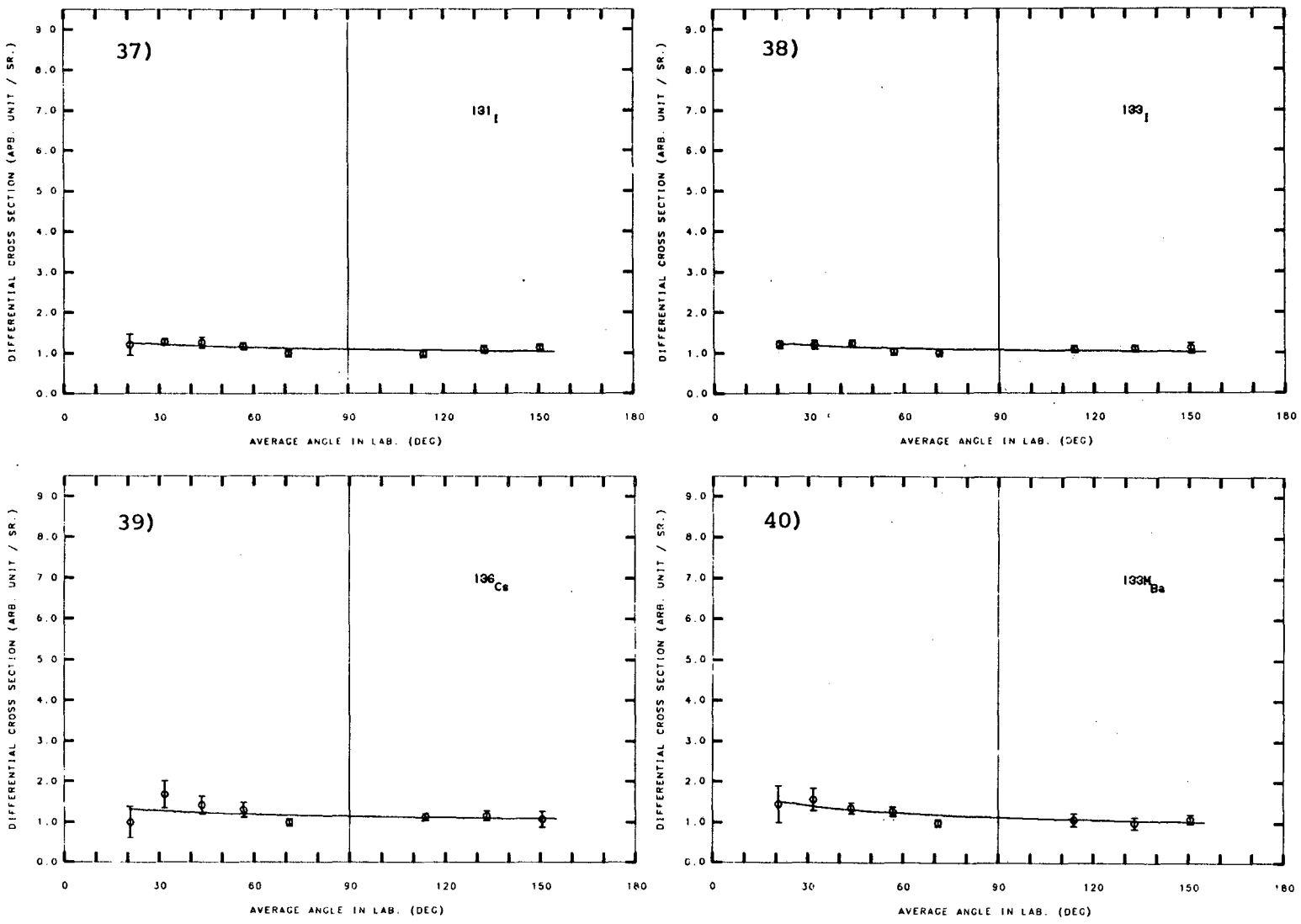

XBL 831-7871

Fig.16

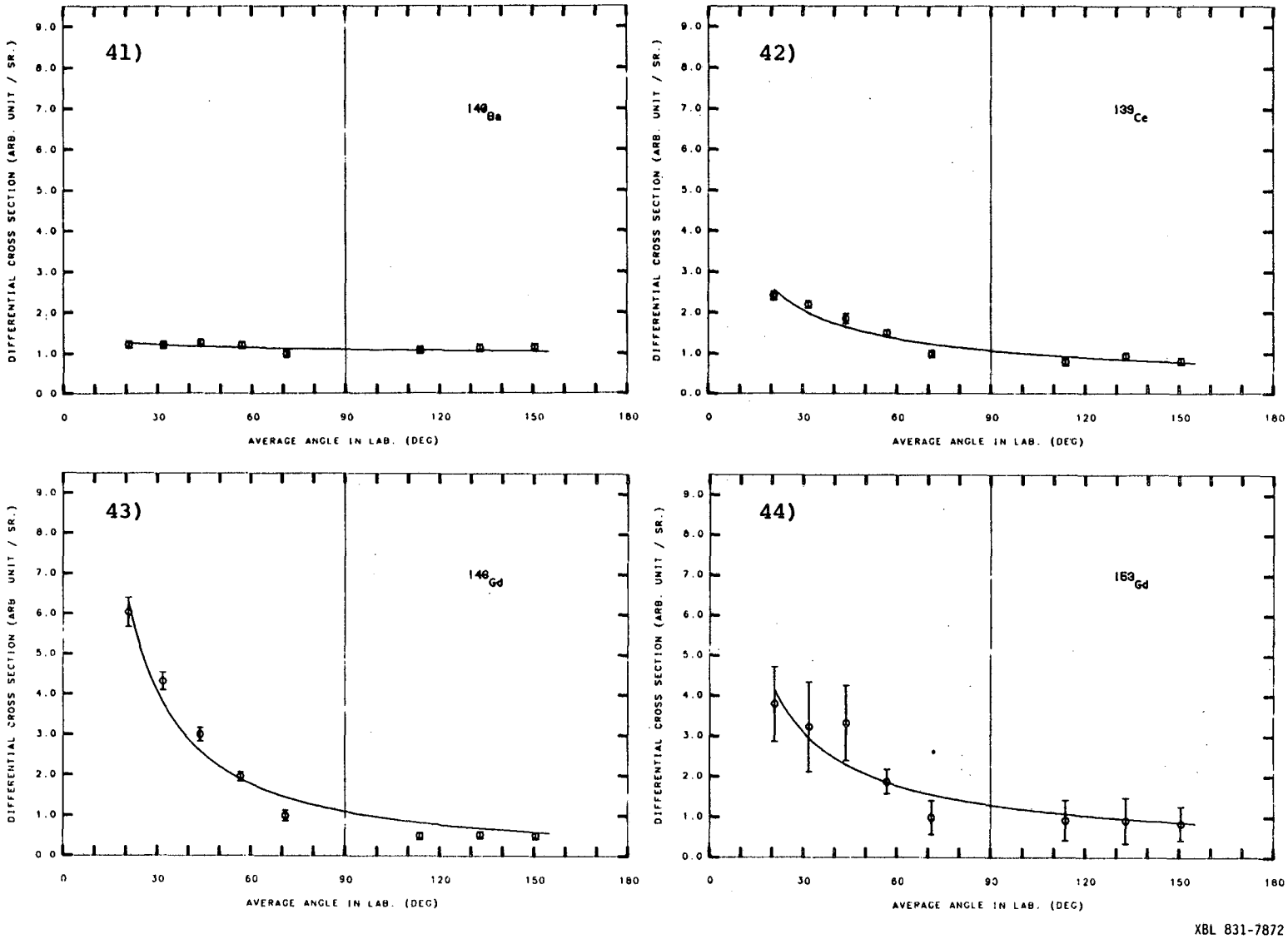
41)
^{140}Ba
42)
^{139}Ce
43)
^{148}Gd
44)
^{153}Gd
DIFFERENTIAL CROSS SECTION (ARB. UNIT / SR.)
AVERAGE ANGLE IN LAB. (DEG)
XBL 831-7872

Fig.16

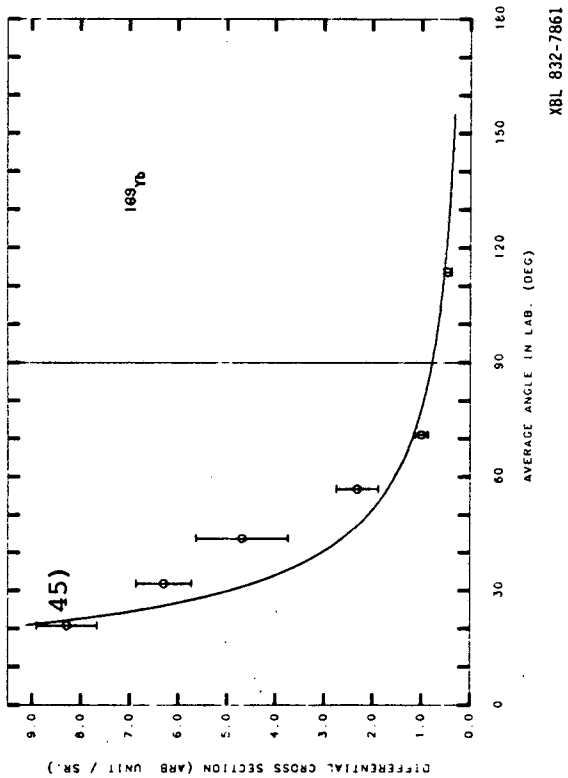
DIFFERENTIAL CROSS SECTION (ARB. UNIT / SR.)
AVERAGE ANGLE IN LAB. (DEG)
169Tb
45)
XBL 832-7861

Fig.16

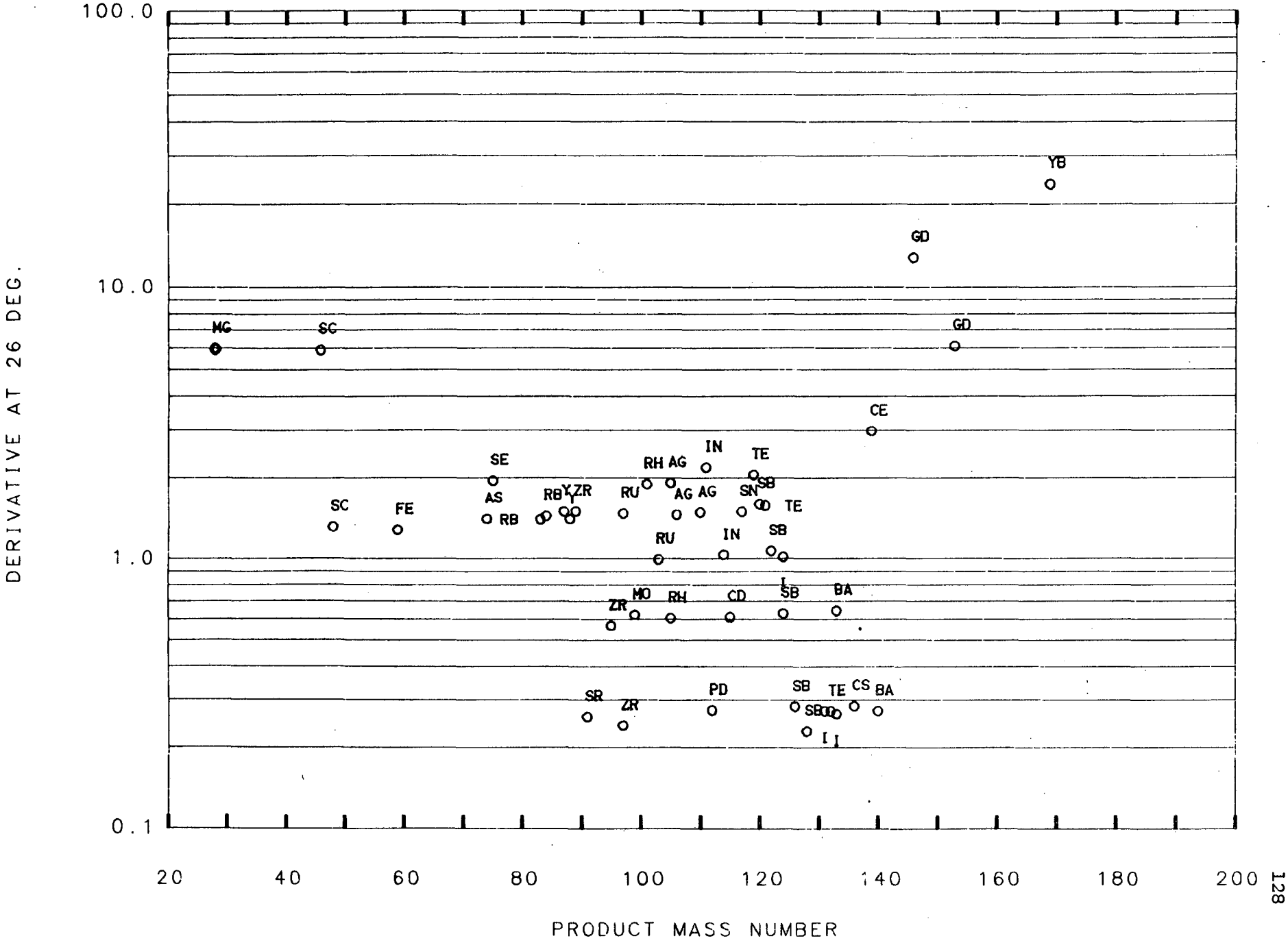

128

XBL 832-8158

Fig.17

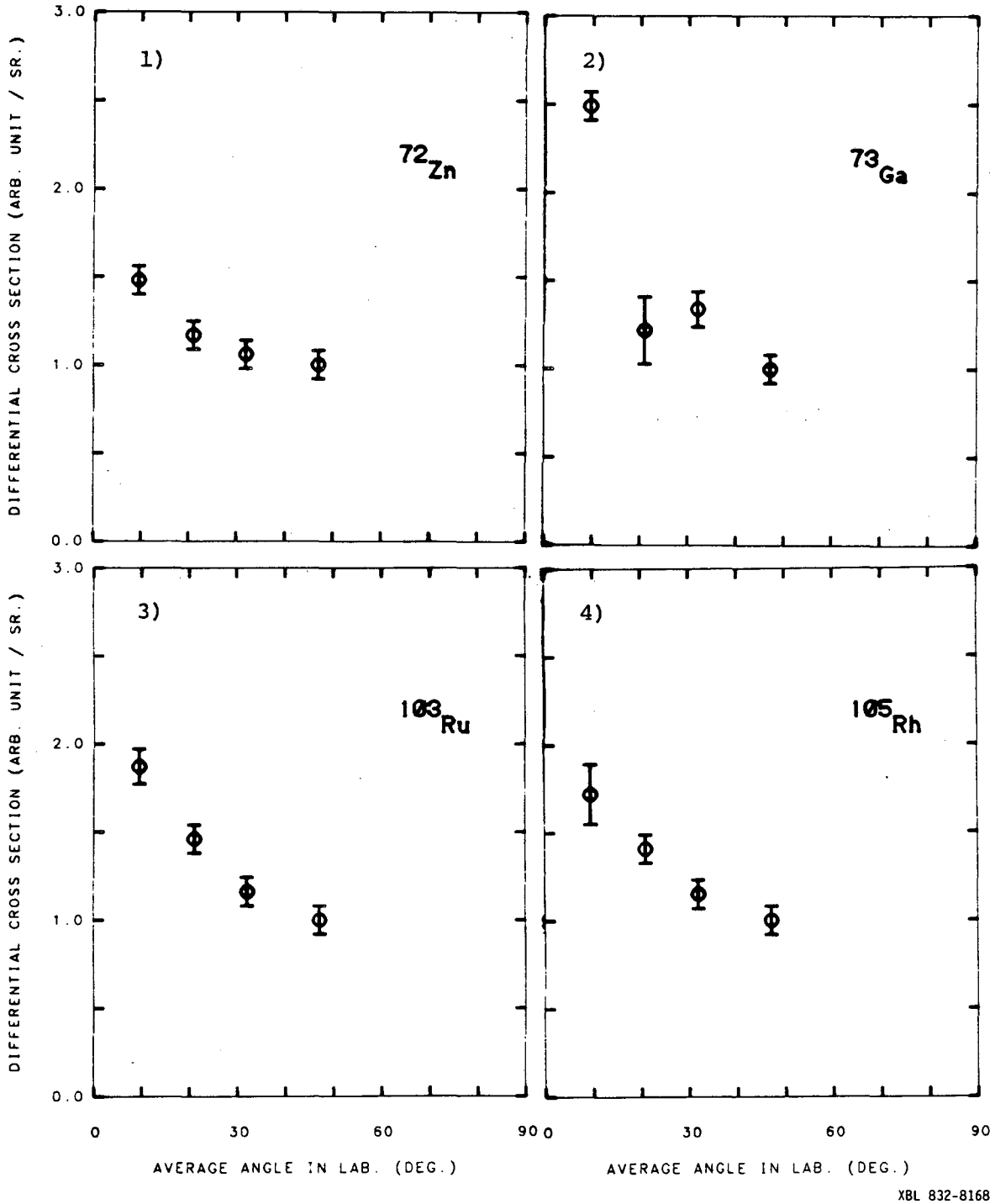
1)
^{72}Zn
2)
^{73}Ga
3)
^{103}Ru
4)
^{105}Rh
DIFFERENTIAL CROSS SECTION (ARB. UNIT / SR.)
DIFFERENTIAL CROSS SECTION (ARB. UNIT / SR.)
3.0
2.0
1.0
0.0
0
30
60
90
AVERAGE ANGLE IN LAB. (DEG.)
AVERAGE ANGLE IN LAB. (DEG.)
XBL 832-8168

Fig.18

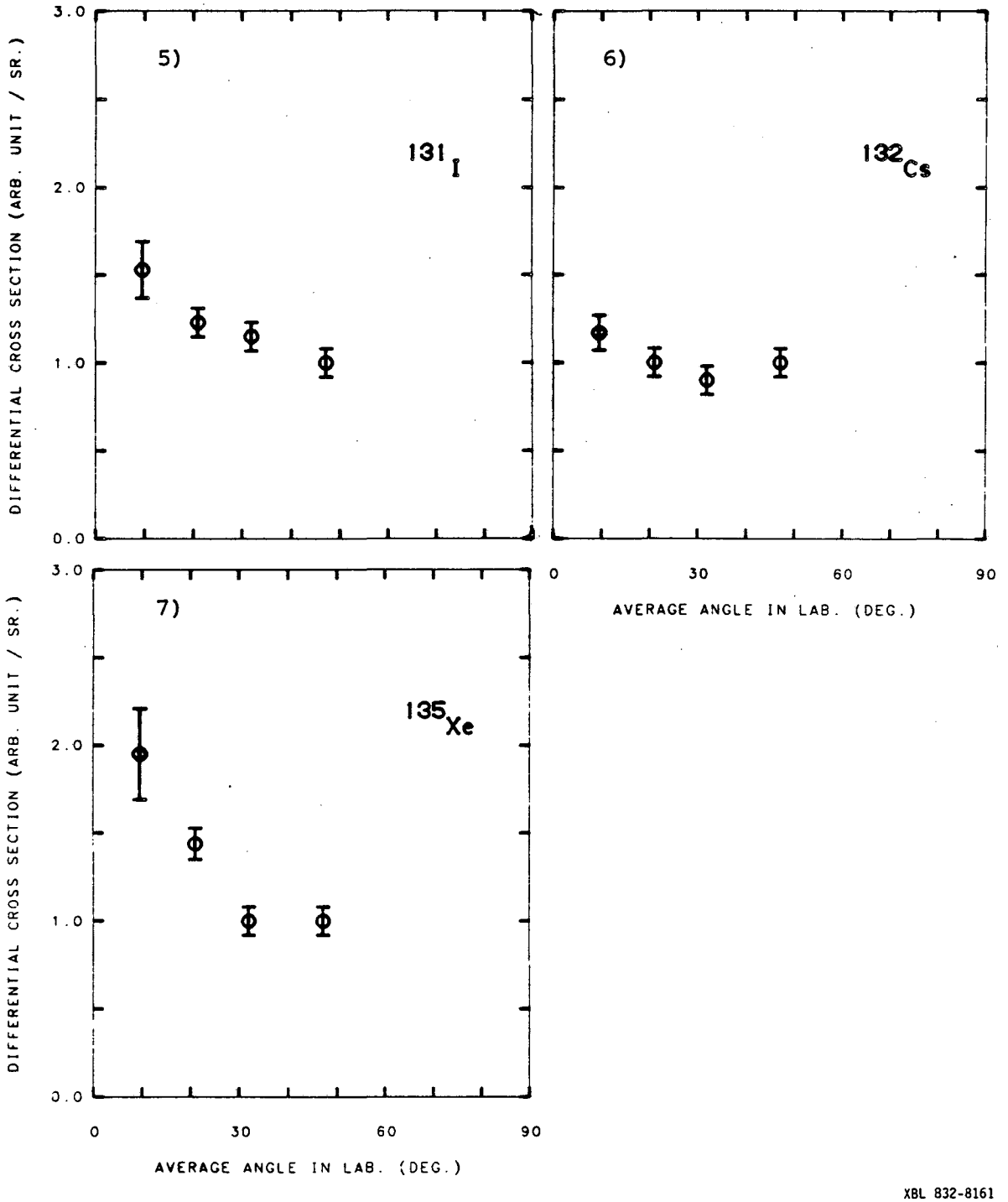
5)
131 I
6)
132 Cs
7)
135 Xe
DIFFERENTIAL CROSS SECTION (ARB. UNIT / SR.)
AVERAGE ANGLE IN LAB. (DEG.)
3.0
2.0
1.0
0.0
0
30
60
90
XBL 832-8161

Fig.18

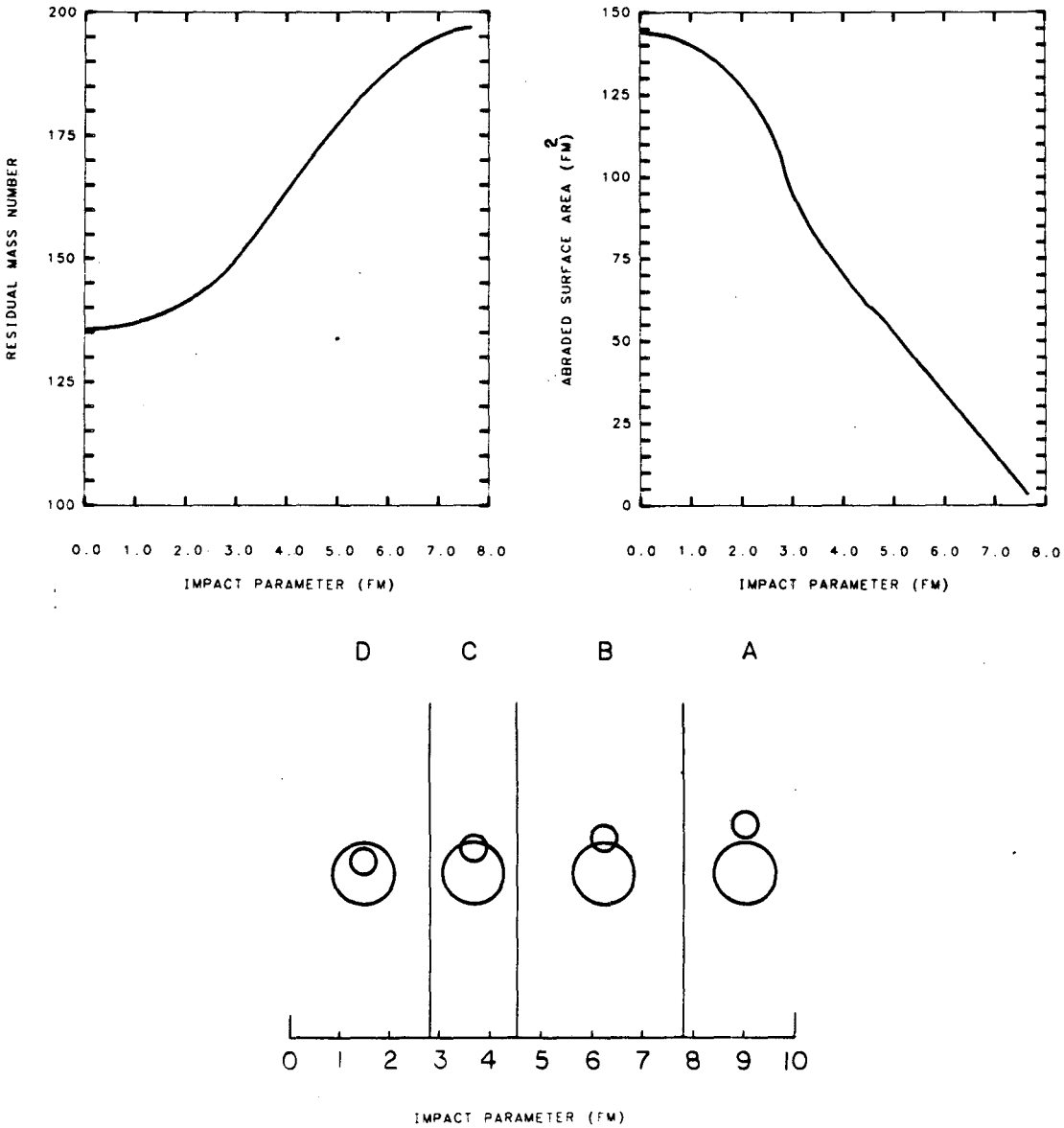

XBL 832-8355

Fig.19

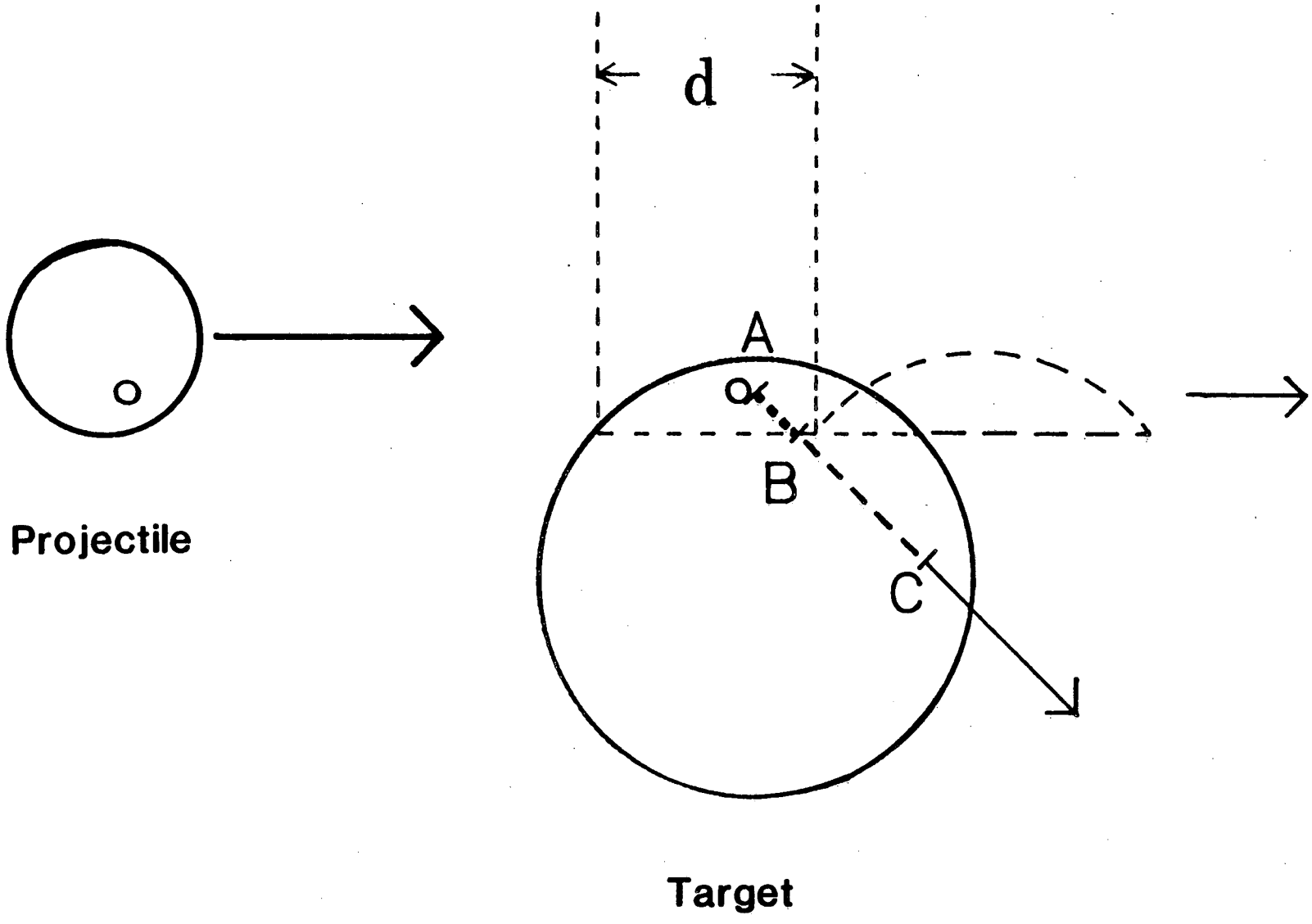

XBL 832-8354

Fig. 20

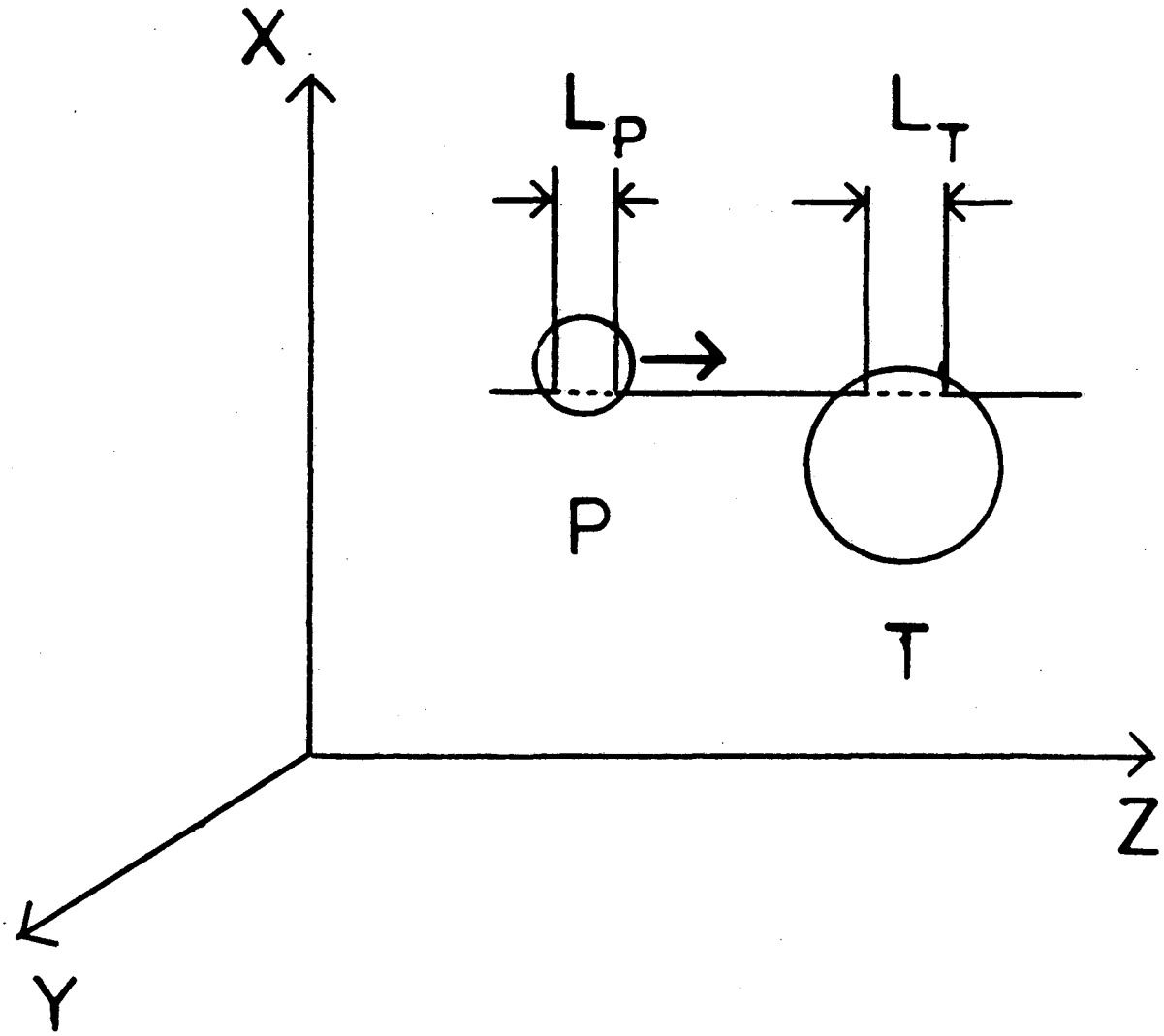

XBL 832-8147

Fig.21

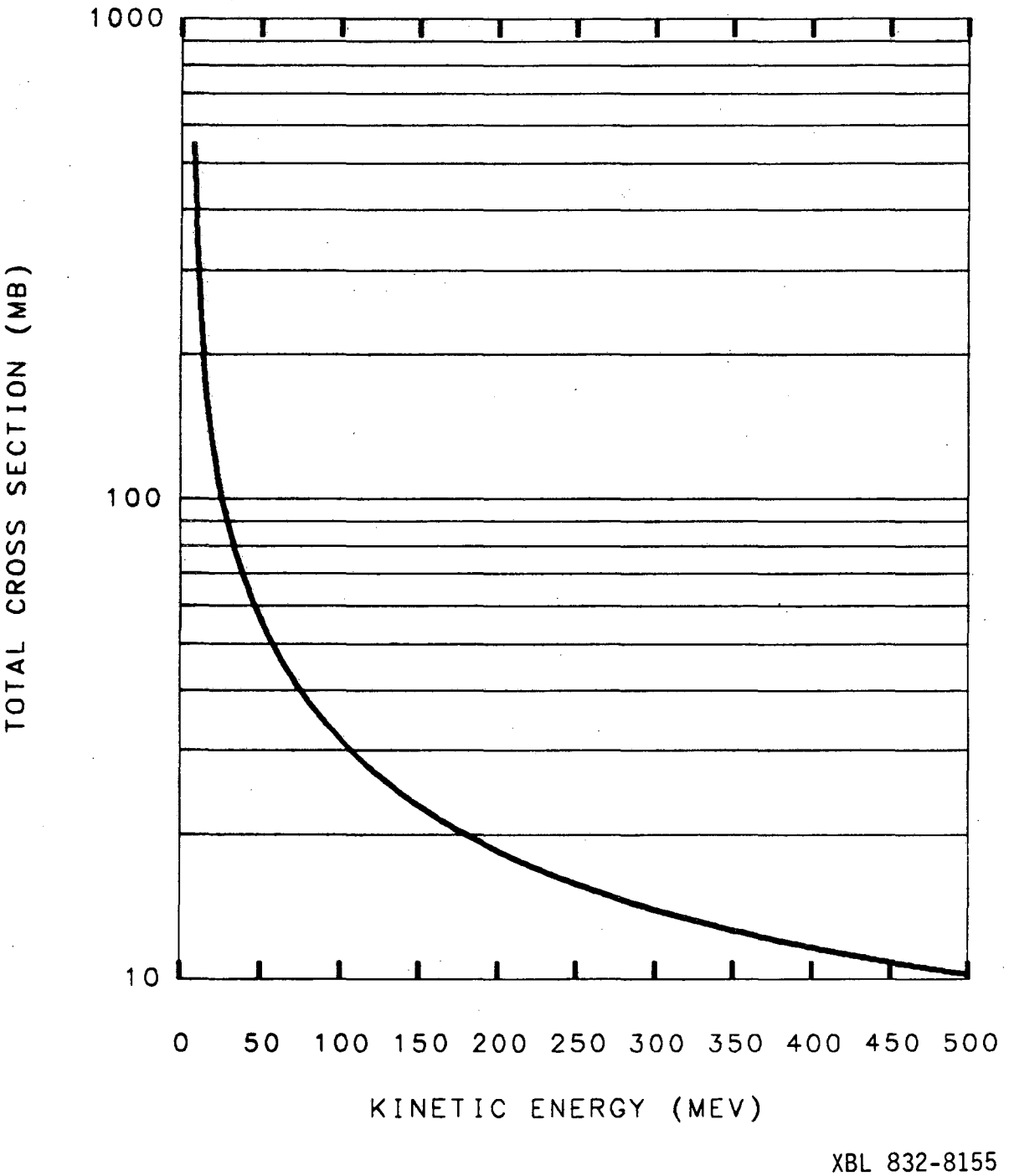
1000
100
10
TOTAL CROSS SECTION (MB)
0
50
100
150
200
250
300
350
400
450
500
KINETIC ENERGY (MEV)
XBL 832-8155

Fig.22

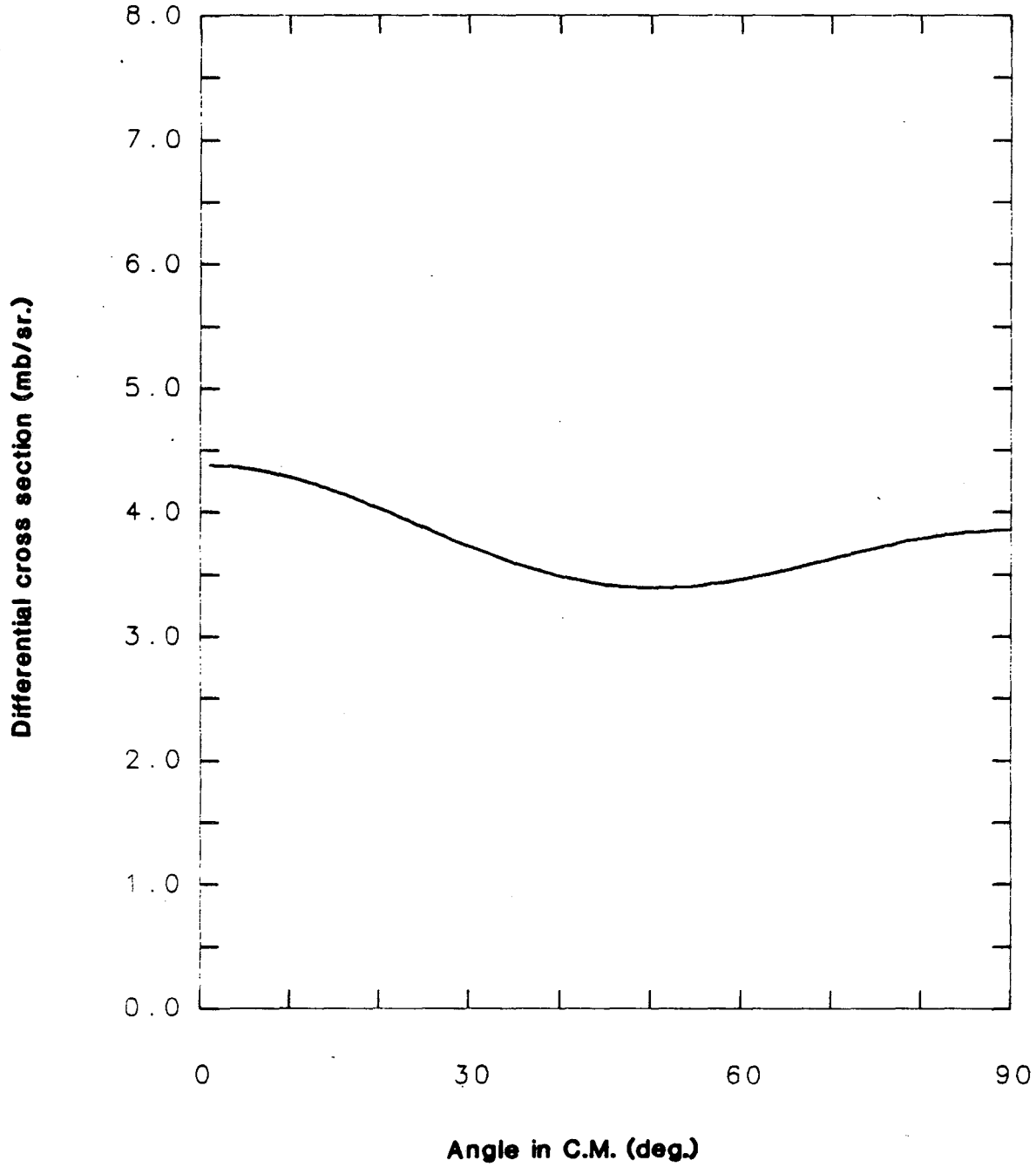

XBL 832-8152

Fig.23

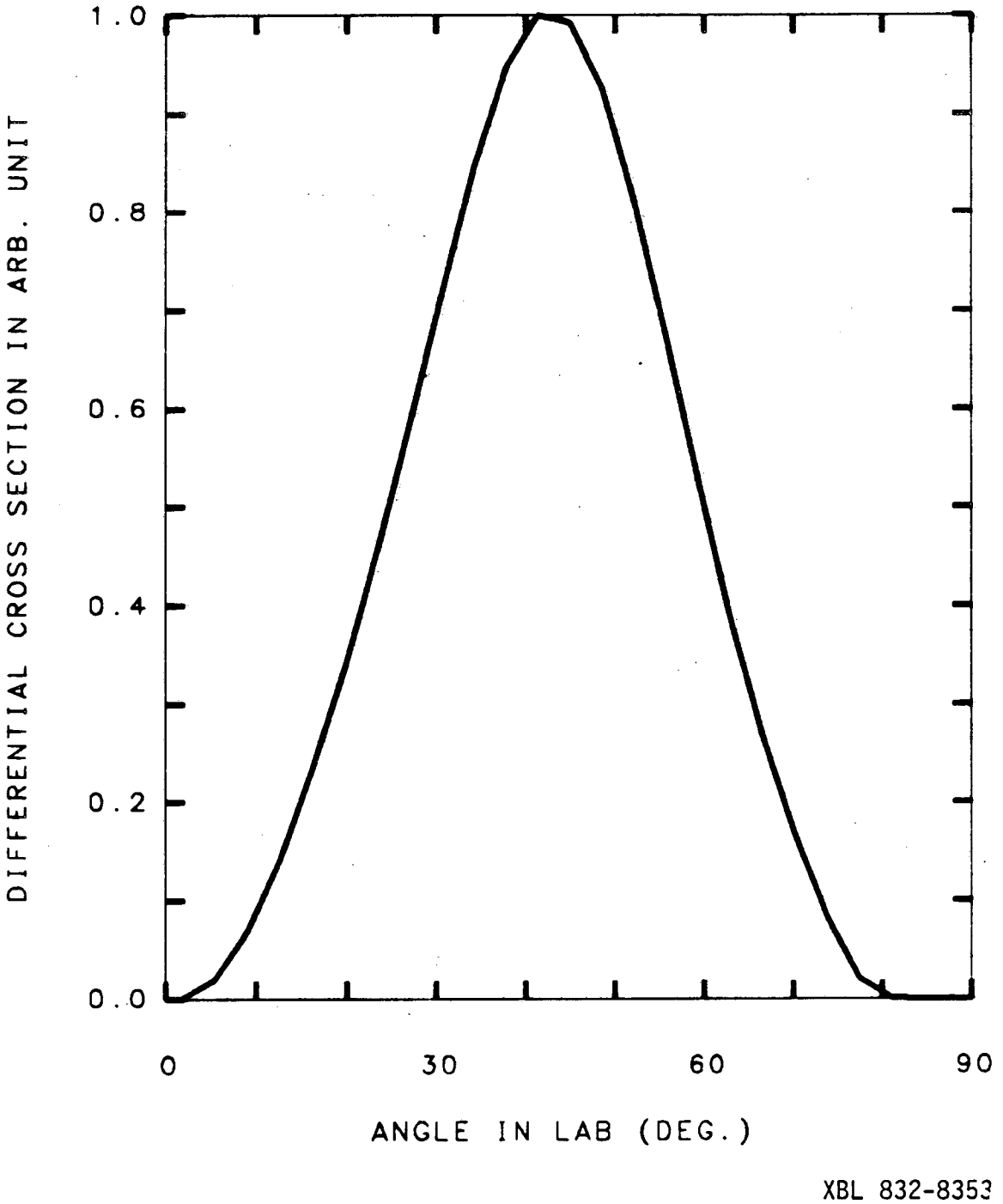
1.0
0.8
0.6
0.4
0.2
0.0
DIFFERENTIAL CROSS SECTION IN ARB. UNIT
0
30
60
90
ANGLE IN LAB (DEG.)
XBL 832-8353

Fig.24

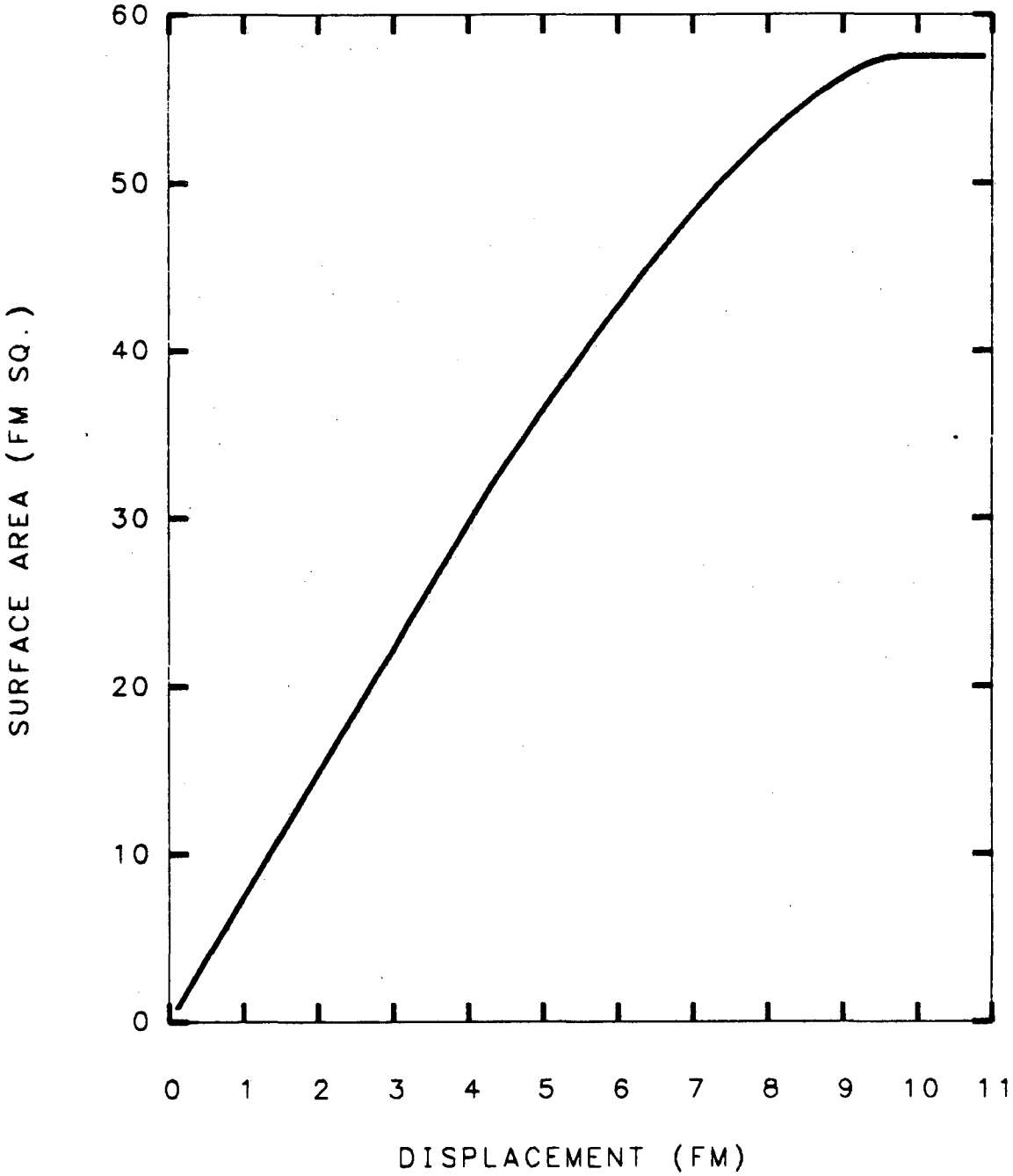

XBL 832-8153

Fig.25

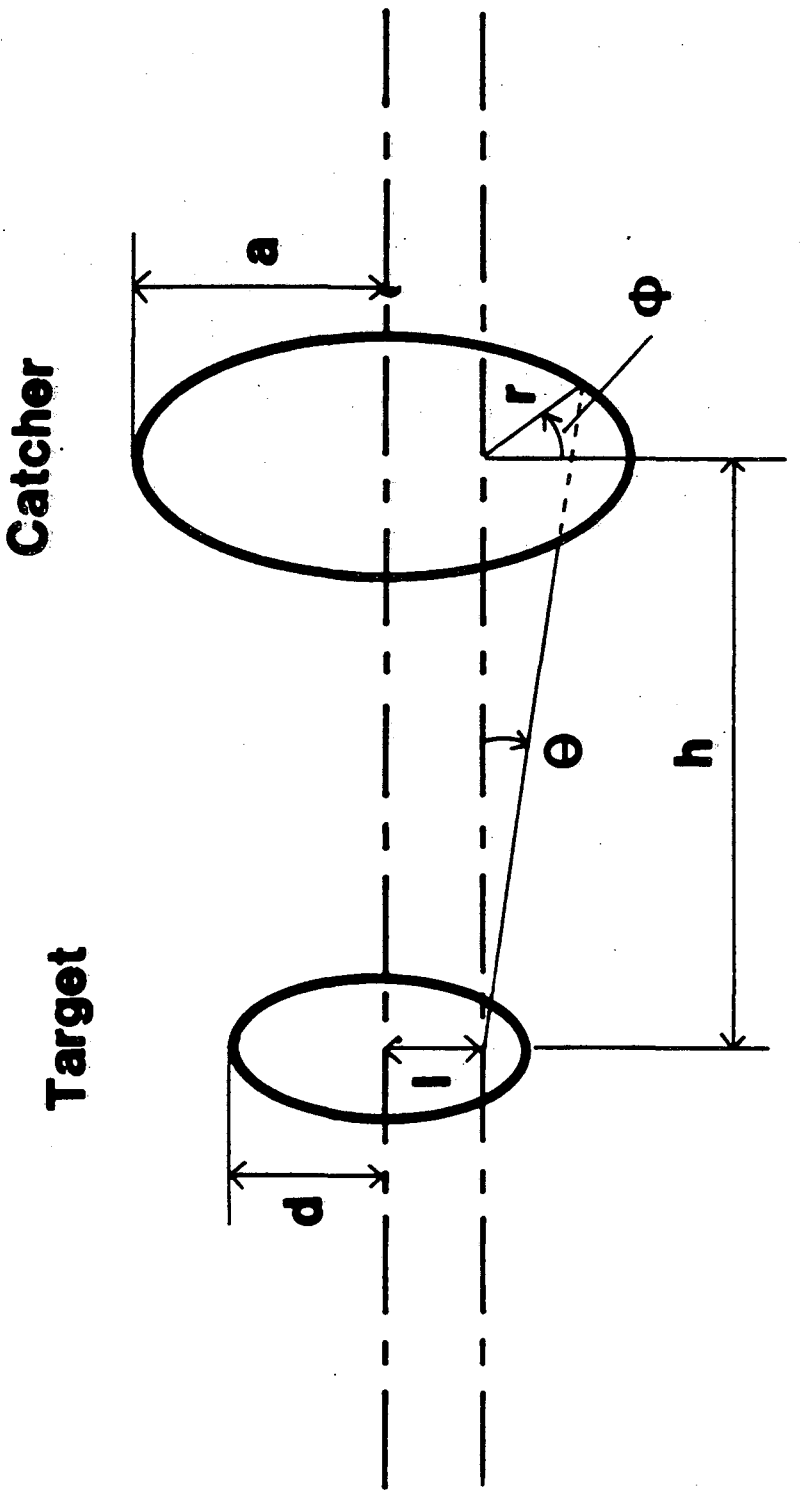

XBL 832-8150

Fig.A-1

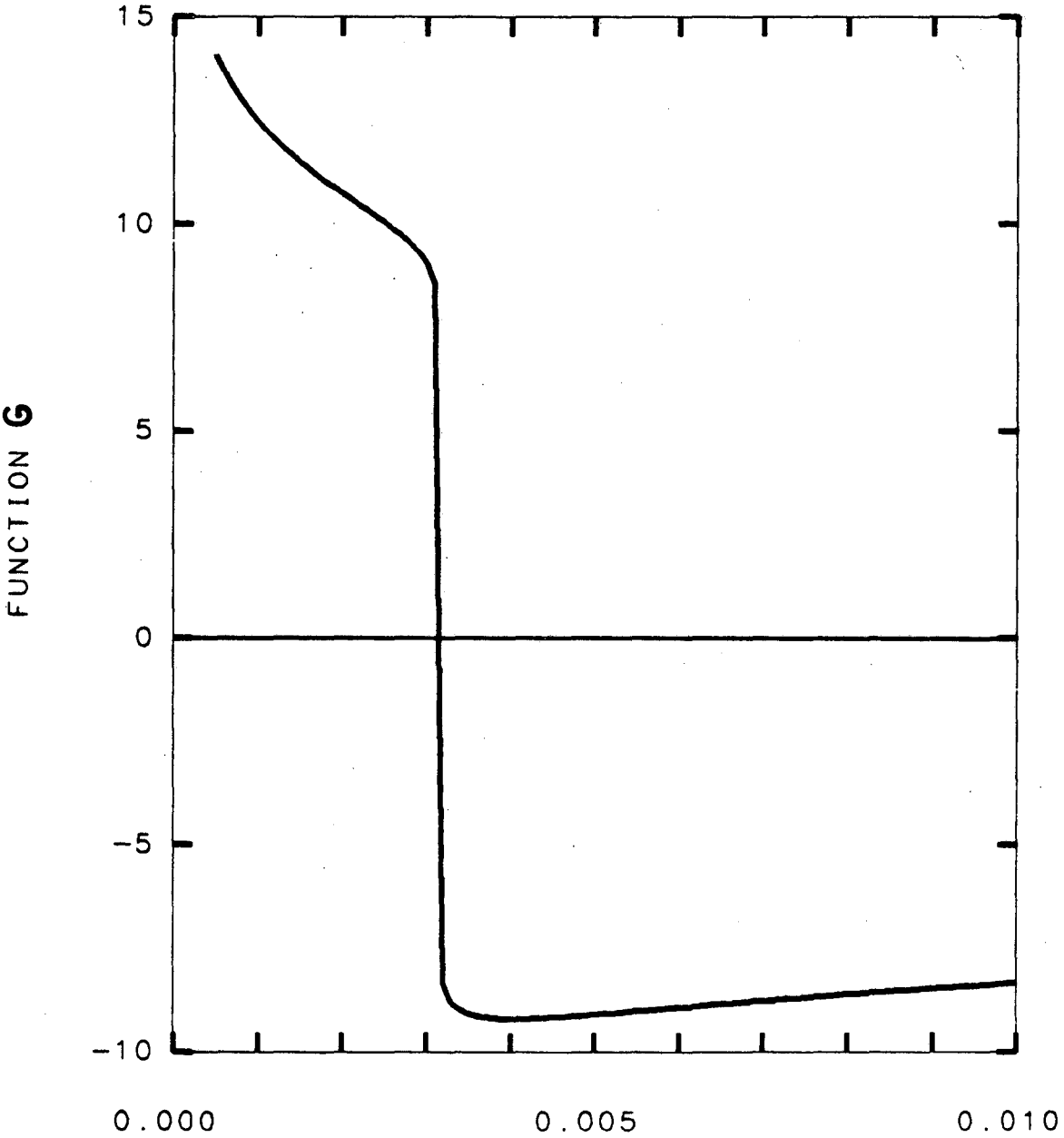

XBL 832-8154

Fig.B-1

This report was done with support from the Department of Energy. Any conclusions or opinions expressed in this report represent solely those of the author(s) and not necessarily those of The Regents of the University of California, the Lawrence Berkeley Laboratory or the Department of Energy.

Reference to a company or product name does not imply approval or recommendation of the product by the University of California or the U.S. Department of Energy to the exclusion of others that may be suitable.

TECHNICAL INFORMATION DEPARTMENT
LAWRENCE BERKELEY LABORATORY
UNIVERSITY OF CALIFORNIA
BERKELEY, CALIFORNIA 94720